A Practical Introduction to Beam Physics and Particle Accelerators

A Practical Introduction to Beam Physics and Particle Accelerators

Santiago Bernal
Institute for Research in Electronics and Applied Physics,
University of Maryland, College Park

Morgan & Claypool Publishers

ISBN 978-1-6817-4076-8 (ebook)
ISBN 978-1-6817-4012-6 (print)
ISBN 978-1-6817-4204-5 (mobi)

DOI 10.1088/978-1-6817-4076-8

Version: 20160301

IOP Concise Physics
ISSN 2053-2571 (online)
ISSN 2054-7307 (print)

A Morgan & Claypool publication as part of IOP Concise Physics
Published by Morgan & Claypool Publishers, 40 Oak Drive, San Rafael, CA, 94903, USA

IOP Publishing, Temple Circus, Temple Way, Bristol BS1 6HG, UK

To the Memory of Martin Reiser (1931–2011)

Contents

Preface

This book is a brief exposition of the principles of beam physics and particle accelerators with emphasis on numerical examples employing readily available computer tools. The same basic ideas can be found with different styles and emphasis in a number of excellent books on beam and accelerator physics: Bryant-Johnsen, Chao, Davidson-Qin, Edwards-Syphers, Lawson, Lee, Reiser, Rosenzweig, Wangler, Wiedemann, Wille, to name a few, and in countless online documents from accelerator schools (USPAS and CERN). However, we avoid detailed derivations, instead inviting the reader to use general high-end languages such as Mathcad and Matlab, as well as specialized particle accelerator codes (e.g. MAD, WinAgile, Elegant, and others) to explore the principles presented. This approach allows the student to readily identify relevant design parameters and their scaling. In addition, the computer input files can serve as templates that can be easily adapted to other related situations.

The examples and computer exercises comprise basic lenses and deflectors, fringe fields, lattice and beam functions, synchrotron radiation, beam envelope matching, betatron resonances, and transverse and longitudinal emittance and space charge. The last chapter presents examples of two major types of particle accelerators: radio frequency linear accelerators (RF linacs) and storage rings. Lastly, the appendix gives the reader a brief description of the computer tools employed and concise instructions for their installation and use in the most popular computer platforms (Windows, Macintosh and Ubuntu Linux). Hyperlinks to websites containing all relevant files are also included. An essential component of the book is its website (actually part of the author's website at the University of Maryland). It contains the files that reproduce results given in the text as well as additional material such as technical notes and movies. We will add new or updated material as it is developed. Although we have chosen Mathcad for most examples, we will add Matlab and Python scripts in the near future.

Acknowledgments

We thank all members of the University of Maryland Electron Ring (UMER) group. The discussions we have had over the years and the study of Professor Martin Reiser's book *Theory and Design of Charged-Particle Beams* were the inspiration that led to the present book. Special thanks to Max Cornacchia, former visiting scientist at the University of Maryland, for many insightful physics discussions and invaluable help with the Elegant code. We also thank Dr Brian Beaudoin for his hard work and continuous assistance with experiments and for useful hints on longitudinal space charge issues; Dr David Sutter for many insights particularly on experimental and historical aspects of accelerators; Dorothea Brosius for her help in setting up the book's website; Dr Chris Allen (Oak Ridge National Lab) for granting us permission to include his beam envelope code SPOT in our website; Dr Hui Li (Confer Technologies, Inc.) for his Matlab application code Menv, and Dr Valter Kiisk (University of Tartu in Estonia) for his Mathcad program 2D Optical Ray Tracer. We also acknowledge the patience and support from our family and the publishers. Last, but not least, we acknowledge the continuing financial support of the Office of Science, Office of High Energy Physics of the US Department of Energy. Matlab® is a registered trademark of MathWorks®, Python™ is a trademark of Python Software Foundation.

Author biography

Santiago Bernal

Santiago Bernal obtained a BSc in physics from the Universidad Nacional de Colombia in Bogotá, Colombia in 1981, an MSc in physics from Georgia Tech in 1983, and a PhD in physics from the University of Maryland, College Park in 1999. He worked for his PhD under the direction of the late Professor Martin Reiser. Before his graduate studies at Maryland, Dr Bernal taught college physics and math in Colombia and Puerto Rico. Dr Bernal joined the UMER group in 2000 as a postdoc, later becoming a research scientist at the Institute for Research in Electronics and Applied Physics (IREAP). He was involved in the design and construction of UMER and has been a leading experimentalist in the project. Dr Bernal helped organize and conduct an experimental course in UMER for the 2008 US Particle Accelerator School. He is the junior coauthor with Charles L Joseph (Rutgers University) of *Modern Devices*: *The Simple Physics of Modern Technology* (Wiley, 2016). Chapter 22 of *Modern Devices* contains a general discussion of a few additional topics on particle accelerators such as cyclotrons, not covered in this book. Besides beam and accelerator physics, Dr Bernal is interested in statistical mechanics and educational aspects of physics.

IOP Concise Physics

A Practical Introduction to Beam Physics
and Particle Accelerators

Santiago Bernal

Chapter 1

Rays and matrices

To understand particle accelerators and their components, we need to study and solve the equations of motion of charged particles in external electromagnetic fields. In their most general form, these equations contain terms involving all orders in the coordinates and velocities of the particles [1, 2]. However, if the particles are confined to small distances from a *reference orbit* and with small angles relative to the same orbit, a *linear equation of motion* resembling a simple pendulum (or mass-on-a-spring) equation results. This is the basis for the *paraxial approximation* presented in section 1.1. The 'spring constant' in the equation of motion can be generalized to include a piecewise *focusing function* whose form depends on the type of external fields present. In addition to the paraxial approximation, the focusing elements of particle accelerators can be treated as *thin* or *thick lenses*, depending on whether the focal length is large or comparable to the physical axial extent of the external fields. We discuss thin and thick lenses in sections 1.2 and 1.3. For both thin and thick lenses, a *matrix* description of particle motion is both convenient and powerful.

1.1 Paraxial approximation

The linearized equation of motion for a charged particle in the presence of external fields represented by the focusing function $\kappa(s)$ is given by:

$$x''(s) + \kappa(s)x(s) = 0, \tag{1.1.1}$$

where primes indicate derivatives with respect to the axial distance 's' measured along the reference trajectory. For now, we consider just one of the transverse coordinates for particle motion, say the horizontal component (or radial in a local curvilinear coordinate system).

Note that equation (1.1.1), known as Hill's equation, is a homogeneous, second-order ODE with a coefficient, the focusing function, which is not constant in general.

doi:10.1088/978-1-6817-4076-8ch1

The solution will depend on the initial conditions $x(0)$, $x'(0)$, and on the form of $\kappa(s)$, but not on any higher orders of either $x(0)$ or $x'(0)$. This latter condition is the essence of the *paraxial approximation*; it is the equivalent of using θ instead of $\sin\theta$ in Snell's law of standard optics.

The general solution of equation (1.1.1) is studied in great detail in many textbooks (e.g. [2]). The solution can be written as a superposition of *cosine-like* $C(s)$ and *sine-like* $S(s)$ functions:

$$\begin{aligned} x(s) &= x(0)C(s) + x'(0)S(s), \\ x'(s) &= x(0)C'(s) + x'(0)S'(s), \end{aligned} \tag{1.1.2}$$

such that $C(0) = 1$, $S(0) = 0$, $C'(0) = 0$, $S'(0) = 1$. In matrix form, equation (1.1.2) reads:

$$\begin{bmatrix} x(s) \\ x'(s) \end{bmatrix} = \begin{bmatrix} C(s) & S(s) \\ C'(s) & S'(s) \end{bmatrix} \begin{bmatrix} x(0) \\ x'(0) \end{bmatrix}. \tag{1.1.3}$$

In a more compact form we can write

$$[x(s),\ x'(s)]^T = \boldsymbol{M}[x(0),\ x'(0)]^T. \tag{1.1.4}$$

The space spanned by the coordinates $x(s)$, $x'(s)$ for an ensemble of particles is called *trace space* or, more commonly, *phase space*. Strictly speaking, this phase space would be the projection on the $(x,\ x')$ plane of the full phase space. In the simple situations whereby no radiation, acceleration, or particle losses occur, the area in phase space is conserved under transformations represented by $\boldsymbol{M}$. The latter statement is known as *Liouville's Theorem*, which we will revisit in chapter 4. As a consequence of this theorem, the determinant of $\boldsymbol{M}$ is equal to 1, i.e. $|\boldsymbol{M}| = 1$.

The simplest case of a focusing function would be the 'point' lens, a mathematical construct whereby $\kappa(s) = \delta(s)/f$. δ represents the Dirac delta function and f is a constant. By integration of equation (1.1.1) with this focusing function, it is easy to see that f represents the focal length of a zero-length lens located at $s = 0$. Figure 1.1 illustrates the zero-length or point lens.

By studying equations (1.1.2) for a point lens, we can identify the *principal trajectories* or rays illustrated in figure 1.1: the first ray has $x'_1(0) = 0$, $x_1(0) = x_{10}$,

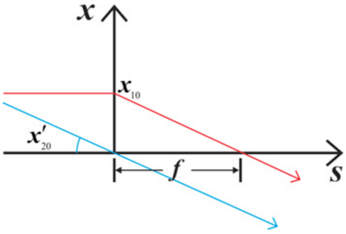

Figure 1.1. The point lens at $s = 0$. The red and blue rays represent the principal trajectories or rays.

leading to $x'_1(s) = -x_{10}(1/f)$, $x_1(s) = x_{10}(1 - s/f)$, for $s > 0$; and the second ray has $x_2(0) = 0$, $x'_2(0) = x'_{20}$, leading to $x_2(s) = x'_{20}s$. Thus, the matrix $\boldsymbol{M}$ is in this case:

$$\boldsymbol{M}_f = \begin{bmatrix} 1 & 0 \\ -1/f & 1 \end{bmatrix}. \tag{1.1.5}$$

Note that the first column in $\boldsymbol{M}$ represents ray 1 (coefficients multiplying initial conditions), while the second column represents ray 2.

An equally important transfer matrix represents the ray transformation over a drift of length L:

$$\boldsymbol{M}_L = \begin{bmatrix} 1 & L \\ 0 & 1 \end{bmatrix}. \tag{1.1.6}$$

The matrices in equations (1.1.5) and (1.1.6) are the building blocks for transforming rays in systems with multiple lenses.

1.2 Thin lens

If the extent of a real lens, as quantified by the *effective length* l_{eff} of the profile of the focusing function $\kappa(s)$, is much smaller than the focal length, then the lens is considered to be *thin*. (The point lens introduced above is an extreme example of a thin lens because it remains so for any $f > 0$). A useful construction that applies especially to lenses whose profiles $\kappa(s)$ are not dominated by *fringe fields*, i.e. extended 'tails', is the *hard-edge model*. Figure 1.2 shows an example of an actual axial profile (of a magnetic field) related to $\kappa(s)$ and the corresponding hard-edge model.

The effective length of the hard-edge model is defined by:

$$l_{\text{eff}} \equiv \frac{1}{\kappa_{\text{peak}}} \int_{-s_1}^{+s_1} \kappa(s)\mathrm{d}s, \qquad \frac{1}{f} = l_{\text{eff}}\kappa_{\text{peak}}. \tag{1.2.1}$$

Therefore, the condition for thin lens is $\kappa_{\text{peak}} \ll 1/l_{\text{eff}}^2$. By this criterion, a very strong lens can have a focal length comparable to its effective length, in which case the lens is *not* thin; otherwise, the lens can be weak and have a very long focal length, satisfying the condition of a thin lens.

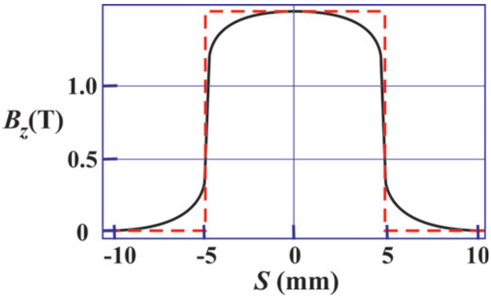

Figure 1.2. Actual axial profile of magnetic field (related to focusing function) and corresponding hard-edge model (red broken curve).

Ray tracing for a thin lens proceeds just as for the point lens (figure 1.1), so, for example, the exit x-coordinate of a given ray is unchanged after traversing the lens. Thus, the basic transfer matrix that connects ray coordinates on both sides of the lens is the same as in equation (1.1.5).

1.3 Thick lens

Thick lenses in charged-particle optics can be treated just as thick lenses in standard optics. Concepts such as *principal planes*, *nodal points*, etc apply to magnetostatic or electrostatic lenses as well [3]. The principal planes of a thick lens or system of lenses are two hypothetical planes that connect locations of unit magnification, i.e. an object located at one plane is imaged at the second plane and with the same size. Figure 1.3 illustrates the primary and secondary principal planes, H and H'', for a system of two focusing thin lenses separated by a distance d and having the same focal lengths. Ray tracing is done by using the method of parallel rays [4].

We can use equations (1.1.5) and (1.1.6) to find the matrix for the lens system in figure 1.3:

$$\boldsymbol{M} = \begin{bmatrix} M_{11} & M_{12} \\ M_{21} & M_{22} \end{bmatrix} = \begin{bmatrix} 1 & 0 \\ -1/f_2 & 1 \end{bmatrix} \begin{bmatrix} 1 & d \\ 0 & 1 \end{bmatrix} \begin{bmatrix} 1 & 0 \\ -1/f_1 & 1 \end{bmatrix}, \tag{1.3.1}$$

or,

$$\boldsymbol{M} = \begin{bmatrix} 1 - d/f_1 & d \\ -\left(\frac{1}{f_1} + \frac{1}{f_2} - \frac{d}{f_1 f_2}\right) & 1 - d/f_2 \end{bmatrix}. \tag{1.3.2}$$

By multiplying $\boldsymbol{M}$ with a drift matrix (length $= l_1$) on the left and another one (length l_2) on the right, we obtain a new matrix $\bar{\boldsymbol{M}}$:

$$\bar{\boldsymbol{M}} = \begin{bmatrix} \bar{M}_{11} & \bar{M}_{12} \\ \bar{M}_{21} & \bar{M}_{22} \end{bmatrix} = \begin{bmatrix} M_{11} + l_2 M_{21} & M_{12} + l_1 M_{11} + l_2 M_{22} + l_1 l_2 M_{21} \\ M_{21} & M_{22} + l_1 M_{21} \end{bmatrix}. \tag{1.3.3}$$

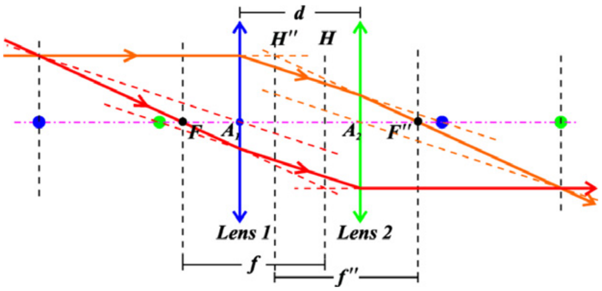

Figure 1.3. The system of two positive thin lenses is equivalent to a thick lens with the principal planes H and H'' shown. Note that the focal lengths of the system are measured from the principal planes.

Now, by setting $\bar{M}_{11} = 0$ we obtain the distance from the second lens to the second focal point of the system, F'' [5]:

$$l_2 = -\frac{M_{11}}{M_{21}} = \left(1 - \frac{d}{f_1}\right)\left(\frac{1}{f_1} + \frac{1}{f_2} - \frac{d}{f_1 f_2}\right)^{-1}. \tag{1.3.4}$$

The second factor on the right of equation (1.3.4) gives the inverse effective *object and image focal lengths* f, f'' of the lens combination [4]:

$$\frac{1}{f} = \left(\frac{1}{f_1} + \frac{1}{f_2} - \frac{d}{f_1 f_2}\right) = \frac{1}{f''}. \tag{1.3.5}$$

The focal lengths f and f'' are *measured from the corresponding principal planes*, as shown in the figures.

Now assume that the second lens is divergent but that the two lenses have the same strength, i.e. the same focal lengths in magnitude: $f_1 = -f_2 > 0$. Then, from equation (1.3.5), the effective focal length is simply:

$$f = \frac{f_1^2}{d} = \frac{f_2^2}{d}. \tag{1.3.6}$$

Furthermore, from equations (1.3.4) and (1.3.5), the second focal point of the system, F'', as measured from the second lens is

$$l_2 = f_1\left(\frac{f_1}{d} - 1\right). \tag{1.3.7}$$

This quantity is positive, indicating a convergent *equivalent thick lens* for the two-lens system if $f_1 > d$. Thus, we arrive at the important result that the combination of two lenses, one convergent (positive) and the other divergent (negative), and having the *same strengths* leads to net focusing if their separation is smaller than the positive focal length f_1. This has an important implication for strong focusing in particle accelerators, as discussed in chapter 3.

Figure 1.4 shows the action of the focusing–defocusing lens combination for two values of their separation d. The geometrical construction for finding the principal planes uses the method of parallel rays, as discussed in the standard optics book by Jenkins and White [4], but examination of the figures may reveal the basic ideas. Note that the principal planes lie outside the space between the lenses in figure 1.4(a), unlike figure 1.3 for a pair of converging lenses with the same separation as in figure 1.4(a).

Additional relationships between the elements of the matrix in equation (1.3.3) and important optical properties of a general lens system are discussed in the article by Halbach [6] and in appendix D of [5].

Computer resources

Matrix multiplication, both symbolically and numerically, can be readily implemented in either Mathcad or Matlab or their freeware counterparts Smath Studio

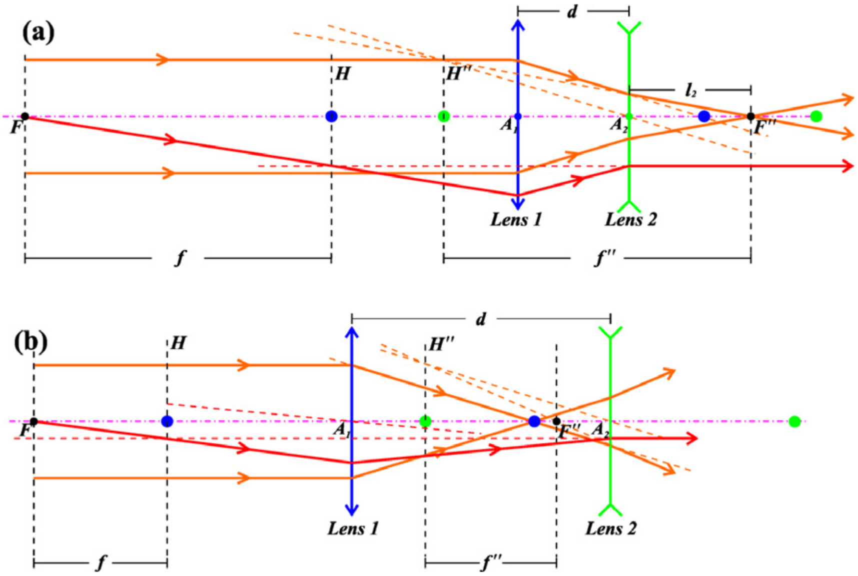

Figure 1.4. Combination of convergent (lens 1) and divergent (lens 2) lenses with the same strengths. In (a) the spacing d is *smaller* than the individual focal lengths ($f_1 = -f_2 > 0$); in (b) the spacing d is *larger* than the individual focal lengths. Note how the principal planes H and H'' are found from the parallel ray technique.

and Octave (see appendix). Many standalone optics design programs are also available, but most are either too expensive or for professional use. Some software of this type is available as packages for codes like Mathematica (e.g. Optics Lab).

We found the free program Optgeo (see appendix) to be instructive and relatively easy to use; in particular, the ray tracing in figures 1.3 and 1.4 can be reproduced without too much effort. We include two Optgeo files in the book's website. Alternatively, for Mathcad users we recommend a very well designed program for 2D optics called 2D Optical Ray Tracer, which is written by Valter Kiisk of the University of Tartu (Estonia) and available online for free. We include in our website a version with input that reproduces closely the results shown in figure 1.4(a). It is important to keep the lens thicknesses small relative to their focal lengths for comparison with figure 1.4, but we can also explore easily thick-lens combinations. Figure 1.5 illustrates typical output.

Another program that we found useful to illustrate the two-thin lens combination is Ray Optics for Android devices (there is a 'Pro' version that adds details of the calculations). Figure 1.6 shows a typical screen from Ray Optics. Note that the object is on the right and that ray tracing goes from right to left, unlike the rest of the figures in the chapter (however, object and image can be exchanged).

RayLab, a free app for Apple's IOS devices, looks very professional and rather challenging as an educational tool for geometrical optics.

Thin magnetostatic lenses can be implemented in several of the most popular codes for particle accelerator design. (In fact, in some cases thin lenses *are* required for some operations such as tracking in the code MAD). We include in our website

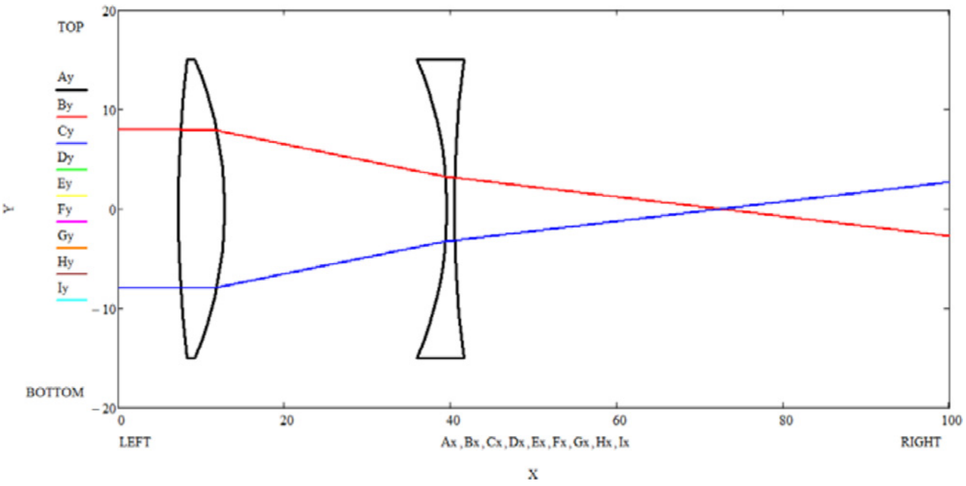

Figure 1.5. Graphics from 2D optics Mathcad program 2D Optical Ray Tracer by Valter Kiisk. Distances are in mm.

Cursor (546.0,77.0)

Object (x = 546.0 , height = 77.0)

Image (x = 182.66 , height = -77.62)

Object

X = 546.0 H = 77.0

Figure 1.6. Screen from the free Ray Optics app for the Android OS. Magnification is close to unity in the example shown.

three example files for the program Winagile (see appendix). The first file illustrates the implementation of one thin quadrupole lens; the other two files are examples of two thin-quadrupole combinations. The files illustrate the concepts of this chapter and also serve as a preamble to quadrupole focusing (chapter 2) and to alternating gradient, or strong focusing (chapter 3). In the appendix we indicate how to download, install and run Winagile. In figure 1.7 we show a screen from Winagile for trajectory tracking with a two thin-quadrupole combination.

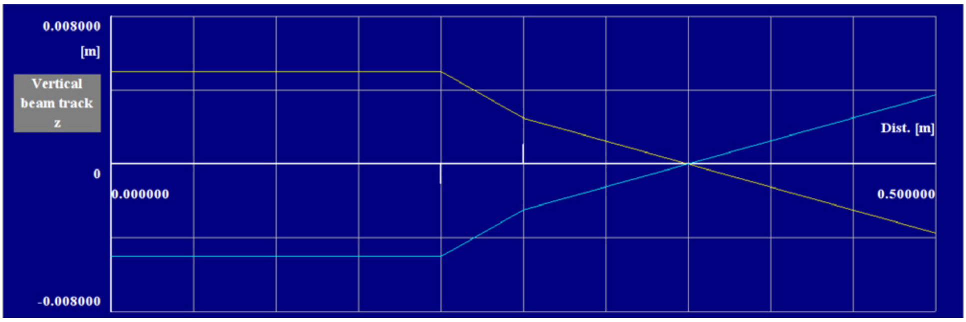

Figure 1.7. Trajectory tracking in Winagile for a combination of two thin quadrupoles of opposite strengths. The quadrupoles are located at $s = 20$ and 25 cm, while their individual focal lengths are $f_1 = -f_2 = 10$ cm. See also chapters 2 and 3 for additional important considerations.

Finally, 'Thin Lens Simulation with Python' (Frant'z blog, April 2011), a Python program for ray tracing through a system of four lenses, can be used to learn both optics and Python (see appendix).

References

[1] Steffen K G 1965 *High Energy Beam Optics* (New York: Wiley)
[2] Wiedemann H 2007 *Particle Accelerator Physics* 3rd edn (Berlin: Springer)
[3] Wollnik W 1987 *Optics of Charged Particles* (Orlando, FL: Academic)
[4] Jenkins F A and White H E 1976 *Fundamentals of Optics* 4th edn (New York: McGraw-Hill) chapter 5
[5] Conte M and MacKay W W 1991 *An Introduction to the Physics of Particle Accelerators* (Singapore: World Scientific)
[6] Halbach K 1964 Matrix representation of Gaussian optics *Am. J. Phys.* **32** 90–108

Chapter 2

Linear magnetic lenses and deflectors

Charged-particle beams in accelerators can be focused and guided by means of electrical or magnetic elements. We restrict the discussion in this chapter to magnetic elements because they are far more common in high-energy accelerators, but the electrical counterparts have essentially the same mathematical treatment. In some cases the same magnet provides both deflection and focusing (combined-function magnet), but most modern machines employ separated-function magnets. In other words, beam deflection and focusing are, ideally, completely independent of each other. We discuss in this chapter solenoids, magnetic quadrupoles and dipole deflectors. Solenoids are not commonly employed as main lattice elements, but mostly to manipulate electron bunches near the source and for other specialized applications. Solenoid focusing *per se* is an interesting but not straightforward concept, which we illustrate in detail and contrast with the idealized particle motion in a uniform B-field. Magnetic quadrupoles, on the other hand, are the most widely used lattice elements in accelerators; they provide *linear* strong focusing when paired in the alternating-gradient scheme (chapter 3). Naturally, important *non-linear* focusing elements (e.g. sextupoles and octupoles) are also part of many accelerators, but we will not discuss their principles here. We also present the Kerst–Serber equations and weak focusing in section 2.4. In section 2.5, we discuss dipole magnets and edge focusing, and in the last section we give examples of calculations of effective hard-edge models in solenoid and quadrupole magnets.

2.1 Magnetic rigidity, momentum, and cyclotron frequency

A charged particle moving in the presence of a uniform B-field follows a circular trajectory. By equating the Lorentz force, $\boldsymbol{F} = q\boldsymbol{v} \times \boldsymbol{B}$, for a particle of charge q and

doi:10.1088/978-1-6817-4076-8ch2

velocity $\boldsymbol{v} = \beta c\, \hat{\boldsymbol{\theta}}$ (c = speed of light in vacuum, $\hat{\boldsymbol{\theta}}$ = unit vector in the azimuthal direction), to the centripetal force we obtain

$$qvB = \frac{\gamma m v^2}{\rho}, \tag{2.1.1}$$

where ρ is the radius of the circular orbit, m is the rest mass, and γ is the relativistic mass factor $\gamma = (1 - \beta^2)^{-1}$. Therefore, if the relativistic linear momentum is defined as $p = \gamma m \boldsymbol{v}$, we have

$$B\rho = \frac{p}{q}. \tag{2.1.2}$$

The quantity $B\rho$ is called the *magnetic rigidity*, and its units are Tm (Tesla-meter, in SI units), or Gcm (Gauss-cm, in CGS units). The reason for that name is that particles with higher energies and therefore higher $B\rho$ are harder to 'bend': a higher field would be required for a fixed orbit radius ρ. It is strange (and sometimes confusing) to name the product of two quantities with a single name, but it is almost universal usage in the accelerator-related literature. Perhaps only Wollnik [1] uses a single symbol (χ_B) for magnetic rigidity.

From the special theory of relativity, the relativistic momentum, total energy E and rest mass energy $E_0 = mc^2$ are connected by the relation

$$E^2 = p^2c^2 + E_0^2 \approx p^2c^2. \tag{2.1.3}$$

The last equality is valid for highly relativistic particles, i.e. particles for which $E \gg E_0$. For reference, $E_0 = 0.511$ MeV for the electron, and $E_0 = 938$ MeV, or 0.938 GeV, for the proton.

As an example, if B is given in Tesla (T) units and ρ in meters, we can write the following relation for *relativistic electrons*:

$$B[\mathrm{T}]\rho[\mathrm{m}] = 0.3p[\mathrm{GeV}/c]c, \tag{2.1.4}$$

where the momentum p is given in units of GeV/c and c is the speed of light. Thus, a 300 MeV electron will move on a circular trajectory of 1 m radius in a 1 T B-field. As an exercise, the reader can write the corresponding relation for the magnetic rigidity of relativistic protons.

Finally, by writing $v = \rho(\mathrm{d}\theta/\mathrm{d}t) = \rho\omega_C$, we obtain from equation (2.1.1) the expression for the angular frequency of revolution of a particle of charge q in a uniform field B_0. It is called the *cyclotron frequency*:

$$\omega_C = \frac{qB_0}{\gamma m}. \tag{2.1.5}$$

A related frequency, which we will use later, is the *Larmor frequency*:

$$\omega_L = \frac{\omega_C}{2}. \tag{2.1.6}$$

2.2 Solenoid focusing

Solenoids for particle accelerators are built from coils of normal conducting or superconducting wires and fed with very high dc currents to produce central B-fields of up to several tesla (T). (For reference, 1 T = 10 000 gauss, and the magnitude of the Earth's B-field is 0.5 gauss, approximately).

From the discussion in the previous section, we can understand that charged particles in the *central* region of a solenoid of field $\boldsymbol{B}$ follow spiral trajectories that enclose the B-field lines as in figure 2.1. This motion in itself does not constitute focusing; the focusing effect occurs at the edges of the solenoid where the B-field has a radial component. In those fringe regions the Lorentz force produces an azimuthal acceleration which in turn leads to *radially symmetric* focusing. To see this in detail, consider the passage of a particle through the fringe field region depicted in figure 2.2. Let us assume that the particle starts moving in a region at $s = s_0$ with $B = 0$, and with a velocity along the solenoid axis, i.e. with $\dot{\theta}_0 = 0$, but with an offset radius ρ_0 near $r = 0$.

Therefore, the initial *canonical angular momentum* p_θ is zero, or, explicitly

$$\gamma m r^2 \dot{\theta} + q r A_\theta = 0, \tag{2.2.1}$$

where $A_\theta(r, z) = rB(r = 0, z)/2$ is the component of the vector potential that leads to a *rotationally symmetric* field $\vec{B}(r, z) = B_r \hat{\rho} + B_z \hat{z}$ (recall that $B = \nabla \times A$). The rotation frequency of particle motion inside the fringe region is then

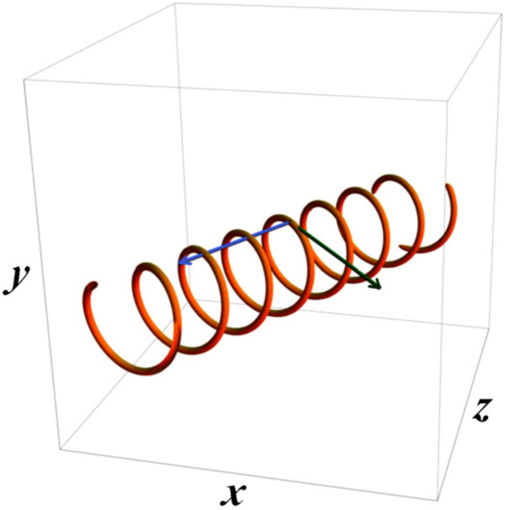

Figure 2.1. Motion of a positively-charged particle in uniform B-field. The blue arrow represents the B-field, while the green one indicates the velocity direction. Source: from 'Charged Particle in a Uniform Magnetic Field' from the Wolfram Demonstrations Project http://demonstrations.wolfram.com/ChargedParticleInAUniformMagneticField/. Contributed by: Jeff Bryant and Oleksandr Pavlyk.

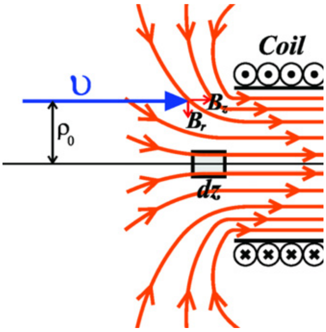

Figure 2.2. Geometry of field lines in fringe region of solenoid lens. Gauss' law applied to the pillbox near the axis provides a way to show that $B_r \cong -(r/2)(\partial B_z/\partial z)_{r=0}$.

$$\dot{\theta} = -\frac{q}{\gamma m r}A_\theta = -\frac{1}{2}\frac{qB_0}{\gamma m} = \mp\omega_L, \tag{2.2.2}$$

from equations (2.2.1), (2.1.5) and (2.1.6). The sign in front of ω_L in equation (2.2.2) is negative if q and B have the same signs and positive if they have opposite signs.

The radius of gyration can be found from the change in azimuthal or transverse linear momentum, $\Delta p_\perp$, not to be confused with p_θ, in the transition from '$B = 0$' space into the fringe region:

$$\Delta p_\perp = q\int_0^{t_1} v_z B_r(z)\mathrm{d}t = q\int_0^{z_1} B_r(z)\mathrm{d}z, \tag{2.2.3}$$

which can be further evaluated from $B_r \cong -(r/2)(\partial B_z/\partial Z)_{r=0}$. The latter result follows from the assumption of a linear radial fringe field $B_r = B_0 r$, rotational symmetry, and $\nabla \cdot \boldsymbol{B} = 0$ in cylindrical coordinates. (Alternatively, we can use Gauss' Law and the pillbox indicated in figure 2.2, see the article by McDonald [2]). We obtain $\Delta p_\perp = -q\rho_0 B_0/2$, which implies a radius of gyration equal to $\rho_0/2$. Furthermore, the opposite change in transverse linear momentum occurs in the transition from inside the solenoid to the region of '$B = 0$ space' on the opposite end of the solenoid.

In conclusion, particles moving initially parallel and near the axis in a solenoid rotate with the Larmor frequency and with a radius equal to one-half the initial offset; this implies that the particles cross the *solenoid axis* at $r = 0$ periodically. It is important to understand that particles rotate with the cyclotron frequency around the center of their individual orbits, but the rotations around the solenoid axis occur at the Larmor frequency. The geometry of these rotations is illustrated in figure 2.3. Additional insights on solenoid focusing can be found in an *American Journal of Physics* article by Vinit Kumar [3] and in a workshop presentation on 'Solenoid Dynamics' by R B Palmer [4].

It is convenient to describe the motion in a reference frame that rotates with the Larmor frequency $\dot{\theta}$, equation (2.2.2). It is clear that particles follow *simple harmonic*

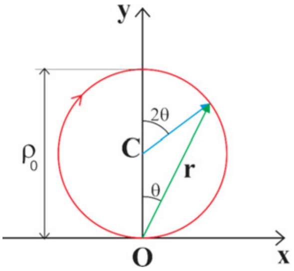

Figure 2.3. Orbit geometry in solenoid focusing of particles with an initial offset equal to ρ_0 and no canonical angular momentum. 'O' is on the axis of the solenoid and 'C' is the center of the individual orbit.

motion in both transverse coordinates. Thus, the wavenumber along the X or Y axis in the *Larmor frame* is

$$k_{X,Y}(z) = \frac{\omega_L(z)}{v_z} = \frac{1}{2}\frac{B(z)}{(B\rho)}. \tag{2.2.4}$$

Finally, from equation (2.2.4) and the paraxial equation of motion (1.1.1), the transverse focusing function for a solenoid can be written as

$$\kappa_S(s) = \frac{1}{4}\frac{B^2(s)}{(B\rho)^2}, \tag{2.2.5}$$

where $B\rho$ is the magnetic rigidity which was defined in equation (2.1.2), and we have reverted to using s instead of z for the axial coordinate. Note that solenoid focusing is always positive.

2.3 Quadrupole focusing

In the absence of electrical currents in the region traversed by a beam inside a magnetic lens, the B-field can be derived from a scalar potential: $\vec{B} = -\nabla\Phi$. In addition, if the lens is long compared to its aperture, we can ignore any dependence of Φ on the axial coordinate z. We have in effect a 2D problem and the scalar potential in cylindrical coordinates can be written as [5]

$$\Phi(r, \theta) = \sum_{n=1}^{\infty}\Phi_n = \sum_{n=1}^{\infty}\left[a_n r^n \cos(n\theta) - b_n r^n \sin(n\theta)\right], \tag{2.3.1}$$

which is applicable inside the magnet. The term $n = 1$, corresponds to a linear potential, i.e. a constant (dipole) field. The term $n = 2$ yields a quadratic (in r) potential

$$\Phi_2(r, \theta) = a_2 r^2 \cos(2\theta) - b_2 r^2 \sin(2\theta). \tag{2.3.2}$$

The part of the potential proportional to b_2 is called the *normal quadrupole component*, while the part proportional to a_2 is the *skew quadrupole component*. The normal component has the form

$$\Phi_{\text{Normal}} = -2b_2 xy, \tag{2.3.3}$$

in Cartesian coordinates. Therefore, the x-component of the Lorentz force on a particle moving initially with velocity v along the $+z$-axis is

$$F_x = -qvB_y = -2qvb_2x. \tag{2.3.4}$$

Similarly, the y-component of the force is

$$F_y = qvB_x = 2qvb_2y. \tag{2.3.5}$$

We can see from equations (2.3.4) and (2.3.5) that an ideal normal quadrupole provides *linear* focusing in the horizontal plane and *linear* defocusing in the vertical plane. This latter statement assumes that the product qb_2 is positive and that v is along the $+z$ direction. Figure 2.4 illustrates the B-field geometry and the forces in such a situation.

To make the connection with equation (1.1.1) and find the form of the focusing function $\kappa(s)$, we first realize that the time and axial derivatives of x are related through

$$\dot{x} = vx', \qquad \ddot{x} = v^2x'', \tag{2.3.6}$$

so Newton's second law yields

$$x'' = -\frac{2b_2}{(B\rho)}x = -\frac{g_x}{(B\rho)}x, \tag{2.3.7}$$

and similarly for the y-direction, except for the sign on the right-hand-side. The *B-field gradients* in the x and y-directions (see equations (2.3.4) and (2.3.5)) are defined by

$$g_x = \frac{\partial B_y}{\partial x}, \qquad g_y = \frac{\partial B_x}{\partial y}. \tag{2.3.8}$$

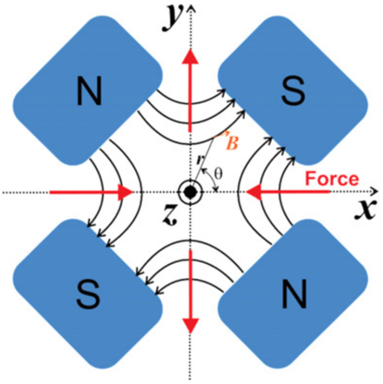

Figure 2.4. Quadrupole magnet for horizontal focusing of beams of positively-charged particles. The red arrows indicate the magnetic forces acting on particles moving out of the plane of the figure.

We generalize and include an *axial dependence* for the field gradients and write

$$x''(s) + \kappa_x(s)x(s) = 0,$$
$$y''(s) - \kappa_x(s)y(s) = 0, \tag{2.3.9}$$

where

$$\kappa_x(s) = \frac{1}{(B\rho)}g_x(s). \tag{2.3.10}$$

Then, the magnitude of the focal length is related to the *integrated gradient* by:

$$\frac{1}{f} = \frac{1}{(B\rho)}\int g(s)\mathrm{d}s = \frac{1}{(B\rho)}g_0 l_{\mathrm{eff}}, \tag{2.3.11}$$

where l_{eff} is the *effective length* and g_0 is the *peak on-axis gradient*.

Typically, magnetic quadrupole lenses, based on either permanent magnets or electromagnets, are employed for focusing of relativistic particles, while electrostatic quadrupoles (based on electric field gradients) are used at low energies. Quadrupole focusing is termed 'strong' focusing because it is more efficient than focusing based on fringe effects (e.g. solenoid focusing or focusing in cyclotron magnets). We can see this by comparing the focal lengths of a quadrupole doublet and a solenoid when both have the same peak B-fields and same overall lengths. If the quadrupoles have aperture a, the magnitude of their peak fields is $g_0 a = B_0$ (ideal linear quadrupoles); further, if their separation is $2l_{\mathrm{eff}}$, with l_{eff} defined in equation (2.3.11), and the solenoid has an effective length equal to $2l_{\mathrm{eff}}$ and the same field B_0, then

$$\frac{f_{\text{solenoid}}}{f_{\text{quad doublet}}} \approx \frac{4l_{\mathrm{eff}}^2}{a^2}, \tag{2.3.12}$$

as the reader can verify from equations (1.3.6) (chapter 1), (2.2.5) and (2.3.11). Since ordinarily $a \ll l_{\mathrm{eff}}$, the doublet is significantly stronger than the equivalent solenoid.

2.4 The Kerst–Serber equations and weak focusing

The discussion in section 2.1 of particle motion in a uniform B-field led to the formula for the cyclotron frequency, equation (2.1.5), which can be complemented with the cyclotron radius or radius of the *design orbit* R_0:

$$R_0 = \frac{\gamma m v}{q B_0} = \frac{(B\rho)}{B_0}. \tag{2.4.1}$$

Although equation (2.4.1) may seem tautological, it must be understood that specifying the magnetic rigidity of a particle does not yield automatically either the actual design orbit radius or the B-field.

An important question regarding circular accelerators is the *stability* of the orbits. Using cylindrical coordinates (r, θ, z), the radial equation of motion is $\gamma m\ddot{r} - \gamma m r\dot{\theta}^2 = qr\dot{\theta}B_z$. We recover equation (2.4.1) if $r = R_0$, $B_z = B_0$, constant, and

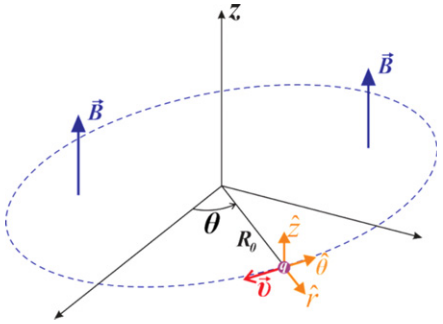

Figure 2.5. Reference orbit and cylindrical coordinate system. The particle is positively charged.

$r\dot{\theta} = -v$. The latter choice of sign indicates that the unit vectors $\hat{r}$, $\hat{\theta}$, $\hat{z}$ form a right-handed coordinate system, with θ increasing in the counterclockwise direction, so a positively charged particle moves in a clockwise direction if the B-field is pointing in the $+z$ direction. Figure 2.5 illustrates the geometry of the problem.

Let us now assume that the particle moves off the design orbit with a small offset x, so that $r = R_0 + x$, with $x \ll R_0$. Furthermore, let us expand the vertical B-field in x and keep only the linear term:

$$B_z(r, x) = B_0 + x\left(\frac{\partial B_z}{\partial r}\right)_{r=R_0} = B_0\left(1 - n\frac{x}{R_0}\right), \tag{2.4.2}$$

where we have introduced the field index n defined by

$$n \equiv -\frac{R_0}{B_0}\left(\frac{\partial B_z}{\partial r}\right)_{r=R_0}. \tag{2.4.3}$$

With these definitions, an equation of motion for x can be easily derived [6, 7]:

$$x''(s) + \frac{1}{{R_0}^2}(1 - n)x(s) = 0. \tag{2.4.4}$$

Similarly, for the vertical motion we have

$$z''(s) + \frac{n}{{R_0}^2}z(s) = 0. \tag{2.4.5}$$

Equations (2.4.4) and (2.4.5) are called the Kerst–Serber equations after D Kerst and R Serber who in 1941 studied the stability of transverse motion in the betatron accelerator. The equations indicate that particles executes harmonic oscillations around the design orbit both radially and in the vertical plane but with different frequencies. These oscillations are called *betatron oscillations*. Further, the motion is stable if the associated focusing function (see equation (1.1.1)) is $\kappa_{x,z} > 0$, i.e. for $0 < n < 1$.

In the radial direction, equation (2.4.4), the focusing function has two parts, one proportional to $1/{R_0}^2$ and the other to $-n$. The first part is a completely geometrical effect and corresponds to what is known as *weak focusing*, while the second part arises because of the appearance of a radial component of the B-field that varies linearly with the height z over the orbit plane. The latter effect can be seen from $\nabla \times \boldsymbol{B} = 0$, which implies $\partial B_r/\partial z = \partial B_z/\partial r$, or $B_r = -(B_0/R_0)nz$. In the vertical plane there is no geometrical focusing but a focusing function proportional to $+n$ (see equation (2.4.5)), the opposite of the situation in the horizontal plane. We can recast equation (2.4.4) to see the quadrupole term more clearly (see equation (2.3.8)):

$$x''(s) + \left(\frac{1}{{R_0}^2} + \frac{g_x}{(B\rho)}\right)x(s) = 0, \qquad g_x = \left(\frac{\partial B_z}{\partial x}\right)_{x=0}, \tag{2.4.6}$$

since $B_0R_0 = B\rho$, and we are using z instead of y for the vertical coordinate.

Furthermore, from equation (2.4.4), the wavenumber associated with the radial motion is $k_x = \sqrt{\kappa_x} = (1 - n)^{1/2}/R_0$. Thus, the number of radial oscillations per turn, which defines the *radial betatron tune*, ν_x, is

$$\nu_x = \frac{2\pi R_0}{\lambda_x} = k_xR_0 = (1 - n)^{1/2}. \tag{2.4.7}$$

Similarly for the *vertical betatron tune*:

$$\nu_z = k_zR_0 = n^{1/2}. \tag{2.4.8}$$

We see that with weak focusing the betatron tunes, as the field index, cannot be larger than 1 if the orbits are to be stable. This limitation is overcome in a different scheme, strong focusing, discussed in chapter 3.

2.5 Dipoles and edge focusing

Let us assume that a charged particle of magnetic rigidity $B\rho$ moves through a region of uniform field ΔB and length L. By equating the centripetal force to the Lorentz force and recalling that $\dot{\theta} = \theta' v$ and the definition of magnetic rigidity, we find the deflection angle $\Delta\theta$ caused by this dipole field:

$$\Delta\theta = \frac{\Delta B \cdot L}{(B\rho)}. \tag{2.5.1}$$

(Alternatively, we can simply use $\Delta\theta = \Delta s/\rho$, where Δs is the arc length, and multiply by $\Delta B/B$ with the understanding that $\Delta B = B$ for a uniform field.)
More generally, we can write

$$\Delta\theta = \frac{1}{(B\rho)}\int_{s_1}^{s_2} B(s)\mathrm{d}s, \tag{2.5.2}$$

for the deflection through a non-uniform field $B(s)$. Note that we can obtain equation (2.5.2) by setting $\mathrm{d}s = \rho(s)\mathrm{d}\theta$, and using $B(s)\rho(s) = B\rho$, for all s, the latter equality being valid without acceleration (other than centripetal). Here we see the

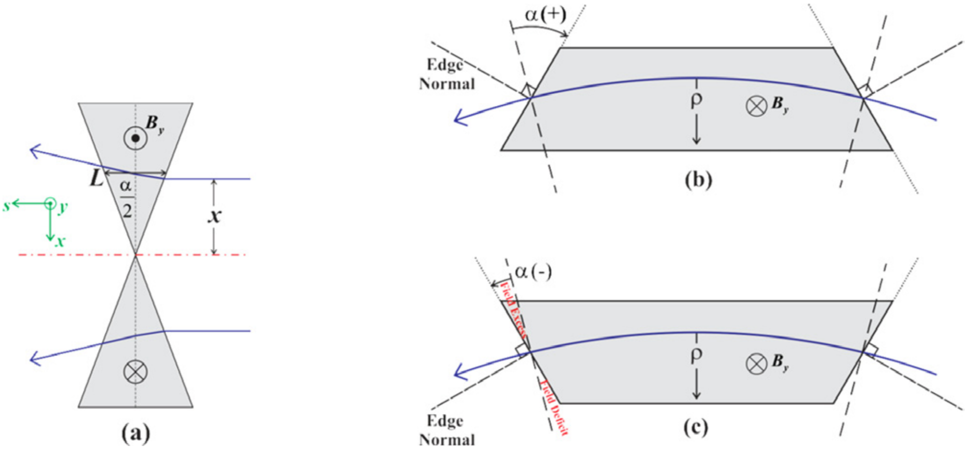

Figure 2.6. Edge focusing of a positively-charged particle: (a) thin magnetic wedge, (b) magnet with horizontal edge-defocusing, and (c) magnet with horizontal edge-focusing. The blue traces in (b) and (c) indicate the reference trajectories (radius ρ).

potential for confusion because we need to distinguish $B(s)$ in the integrand in equation (2.5.2) from B in the factor outside the integral. The latter B is not to be taken separately, because the actual factor is $B\rho = p/q$, constant. Note also that the net deflection is proportional to the 'integral Bds', regardless of the details of how the field varies along the trajectory through the dipole magnet.

Motion through the boundary regions in a real dipole magnet leads to focusing effects. In essence, a particle moving with a (transverse) offset distance from the reference trajectory can see either a 'deficit' or an 'excess' of integrated transverse magnetic field. Equivalently, from equation (2.5.1), particles are deflected by an angle proportional to the traversed distance L in the boundary region, which in turn is to first order proportional to the transverse offset. We can see this explicitly with help from figure 2.6(a), which represents the effect of either edge in the dipole magnet depicted in figure 2.6(b).

Figures 2.6(b) and 2.6(c) show reference trajectories forming an angle $|\alpha|$ with the normal to the pole faces. The intermediate case between figures 2.6(b) and 2.6(c) is not shown but we can deduce that it corresponds to $\alpha = 0$: the reference trajectory enters and exits the pole faces along the normal to the faces. This latter magnet is called a *sector magnet*. Thus, the thin wedge magnet of figure 2.6(a) is designed so that it *subtracts* from the field of an ideal sector magnet on the upper part (of the reference trajectory, at the boundary), but adds to the field on the lower part. In other words, the magnet of figure, 2.6(b) is equivalent to the superposition of a sector magnet and a thin wedge magnet (figure 2.6(a)) at each end. Furthermore, the distance in the thin wedge of figure 2.6(a) is $L = 2x\,\tan(|\alpha|/2) \cong x\,\tan|\alpha|$. Therefore, from equation (2.5.1) we can write

$$\Delta\theta = \frac{B_y \tan\alpha}{(B\rho)}x. \qquad (2.5.3)$$

By convention the angle α for the magnet in figure 2.6(b) is *positive*, so equation (2.5.3) implies that net defocusing results (i.e. positive slope for particles moving from right to left). In contrast, the magnet in figure 2.6(c) has a negative α and yields focusing. To summarize, edge focusing is represented by the matrices

$$R_{xx[\text{wedge}]} = \begin{bmatrix} 1 & 0 \\ +\dfrac{\tan\alpha}{\rho} & 1 \end{bmatrix}, \qquad R_{yy[\text{wedge}]} = \begin{bmatrix} 1 & 0 \\ -\dfrac{\tan\alpha}{\rho} & 1 \end{bmatrix}. \tag{2.5.4}$$

R_{xx} and R_{yy} represent thin lenses for the horizontal and vertical planes, respectively.

Although no edge focusing occurs for a sector magnet, the magnet provides net focusing in the horizontal plane. This is just a geometric effect that corresponds to the weak focusing discussed in connection with equation (2.4.4); the focusing constant is then $\kappa = 1/R_0 = 1/\rho$. In the vertical plane, the sector magnet is represented by a drift. In matrix form (see equation (3.2.1)), a horizontal sector magnet is represented by the matrices

$$R_{xx[\text{sector}]} = \begin{bmatrix} \cos\theta & \rho\sin\theta \\ -\dfrac{\sin\theta}{\rho} & \cos\theta \end{bmatrix}, \qquad R_{yy[\text{sector}]} = \begin{bmatrix} 1 & \rho\theta \\ 0 & 1 \end{bmatrix}. \tag{2.5.5}$$

If $|\alpha|$ in a magnet is one-half of the bending angle θ, we have a *rectangular magnet*. It can be shown by matrix multiplication that in this case the geometric and edge effects exactly balance each other out yielding no net focusing in the horizontal plane. In the vertical plane (perpendicular to the bending plane), however, the rectangular magnet can be shown to introduce edge *focusing*.

The section on computer resources at the end describes exercises to illustrate edge focusing, sector and rectangular magnets.

2.6 Effective hard-edge model of fringe fields in focusing magnets

The standard *hard-edge model* of the focusing function $\kappa(s)$ was illustrated in figure 1.2.

It has a length equal to the effective length as defined in equation (1.2.1) and a top value that coincides with the maximum value of $\kappa(s)$. However, the hard-edge model constructed in this way *will not* give correct answers in general. For this reason, other models have been devised to take into account the smooth wings of an actual $\kappa(s)$ profile. An example is the linearization of the end fields. But for basic design calculations it is still more convenient to implement hard-edge models in computer codes to track particle trajectories or trace beam envelopes.

The correct approach to constructing a hard-edge model consists in dividing the focusing function profile into a number of thin slices representing individual lenses and then multiplying out all the individual matrices to obtain a transfer matrix whose elements can be related to the effective length and strength of the magnet [8, 9]. This method of 'slicing' the focusing profile is quite general and is especially suited for cases when the profile has extended wings.

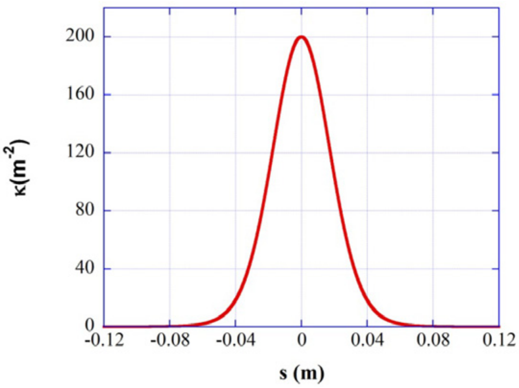

Figure 2.7. Analytical axial profile of focusing function for a short solenoid. The profile is proportional to the square of $B_z(s)$ in equation (2.6.1) with particular values of fit constants and a peak value $\kappa_0 = 200\ \mathrm{m}^{-2}$. See also Mathcad document.

We illustrate here the slicing method using the focusing function for a solenoid. The function is proportional to the square of the on-axis z-component B_z of the solenoid B-field—see equation (2.2.5):

$$B_Z(s) = B_0 \exp\left(-\frac{s^2}{d^2}\right)\left[\operatorname{sec}h\left(\frac{s}{b}\right) + c_0 \sin h^2\left(\frac{s}{b}\right)\right], \tag{2.6.1}$$

where B_0 is the peak field, i.e. the axial field at the middle plane of the solenoid ($z = 0$), and d, b, and c_0 are constants. Equation (2.6.1) can be used to fit very accurately actual magnetic field data for a solenoid used to focus low energy electrons [10]. Figure 2.6 illustrates the $\kappa(s)$ profile.

The profile in figure 2.7 is divided into $N = 203$ slices with a width $\delta = 0.001$ m thus covering $L = 0.203$ m well into the wings where $\kappa \ll 1\%\ \kappa_0$. Each slice is represented by the following matrix, following equation (3.1.1) (see also (1.1.1)–(1.1.3)):

$$\boldsymbol{M}_{\text{slice}} = \begin{bmatrix} \cos\left(\sqrt{|\kappa(s)|}\,\delta\right) & \dfrac{1}{\sqrt{\kappa(s)}} \sin\left(\sqrt{|\kappa(s)|}\,\delta\right) \\ -\sqrt{\kappa(s)} \sin\left(\sqrt{|\kappa(s)|}\,\delta\right) & \cos\left(\sqrt{|\kappa(s)|}\,\delta\right) \end{bmatrix}. \tag{2.6.2}$$

Multiplication of all N matrices leads to:

$$\boldsymbol{M} = \boldsymbol{M}_1\boldsymbol{M}_2 \ldots \boldsymbol{M}_N = \begin{bmatrix} M_{11} & M_{12} \\ M_{21} & M_{22} \end{bmatrix}. \tag{2.6.3}$$

The *effective length* of the solenoid is then found from [9]:

$$l_{\text{eff}} = -\frac{\theta \sin \theta}{M_{21}}, \tag{2.6.4}$$

where θ is the root (nearest to zero) of the transcendental equation

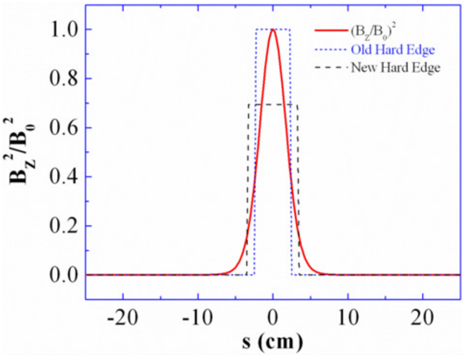

Figure 2.8. Hard-edge models for the normalized focusing function of a short solenoid. The dotted blue line follows the prescription of equation (1.2.1), while the dashed black line results from the slicing method described in the text. From [10]. Used under CC-BY 3.0, http://creativecommons.org/licenses/by/3.0/deed.en_US

$$\cos\theta + \frac{1}{2}\theta\sin\theta - M_{11} + \frac{1}{2}LM_{21} = 0. \tag{2.6.5}$$

L is the extent of the slicing. Furthermore, the *effective strength* of the solenoid is:

$$\kappa_{\text{eff}} = \frac{\theta^2}{{l_{\text{eff}}}^2}. \tag{2.6.6}$$

The method just described yields hard-edge models whose hard-top value *does not* coincide in general with the peak value of the smooth profile. This is illustrated in figure 2.8. Furthermore, there is a slight dependence of the effective length and hard-top strength on the peak strength of the smooth profile $\kappa(s)$. Explicitly, we obtain $l_{\text{eff}} = 0.0651$ m, and $\kappa_{\text{eff}} = 138.62\ \text{m}^{-2}$ for the profile illustrated in figure 2.7 for which $\kappa_0 = 200\ \text{m}^{-2}$. Additional details are included in the references as well as in the Mathcad document mentioned in the next section.

A similar 'slicing' procedure is applicable to quadrupole lenses, but two slightly different effective lengths are obtained, one for the focusing plane (l_f) and another one for the defocusing plane (l_d). Likewise, two effective quadrupole strengths result from the analysis. Thus, instead of equation (2.6.4) and (2.6.5) we have:

$$l_\text{f} = -\frac{\theta_\text{f}\sin\theta_\text{f}}{F_{21}}, \qquad l_\text{d} = -\frac{\theta_\text{d}\sinh\theta_\text{d}}{D_{21}}, \tag{2.6.7}$$

where θ_f, θ_d are solutions of the transcendental equations

$$\begin{aligned}&\cos\theta_\text{f} + \frac{1}{2}\theta_\text{f}\sin\theta_\text{f} - F_{11} + \frac{1}{2}LF_{21} = 0,\\ &\cosh\theta_\text{d} - \frac{1}{2}\theta_\text{d}\sinh\theta_\text{d} - D_{11} + \frac{1}{2}LD_{21} = 0.\end{aligned} \tag{2.6.8}$$

The corresponding effective focusing constants are related to θ_f, θ_d through $\theta = |\kappa|^{1/2}l$. The effective lengths l_f, l_d vary linearly with quadrupole peak gradient in such a way that the average effective length $l_{\text{ave}} = (l_\text{f} + l_\text{d})/2$ is nearly independent of the quadrupole peak gradient. An average effective quadrupole focusing constant is also defined. An example for short magnetic quadrupoles is illustrated in a Mathcad document available in the book's website.

Computer resources

The motion of a charged particle in a uniform *B*-Field can be explored using the Wolfram Demonstrations Project 'Charged Particle in a Uniform Magnetic Field' (see figure 2.1), which is freely available and requires the Wolfram CDF Player.

Particle trajectories in a sector magnet (section 2.5) can be studied numerically using a Mathcad program freely available from the University of Colorado: http://cips.colorado.edu/mathcad/mathcad.html. Scroll down to chapter 3 and download **3_Lorentz_Bending_Magnet.xmcd.** Note that $q = 1$, $m = 1$ and the special construction of the sector: the bending radius originates at the apex of the magnet. Thus, with the default values in the program, the inverse focal length (equation (2.5.5)) is just $1/f = \sin\theta/\rho = \sin 30^\circ = 0.5$, since $\rho = 1$ (SI units implied).

The Winagile (see appendix) files **S-bend.lat** and **R-bend.lat** contain single 10° bends and help to understand the matrix representation and focusing properties of sector and rectangular magnets with 'flat' fields. Run either file as a 'transfer line' and click on the last row to reveal the matrix elements. Figure 2.9, top, shows the

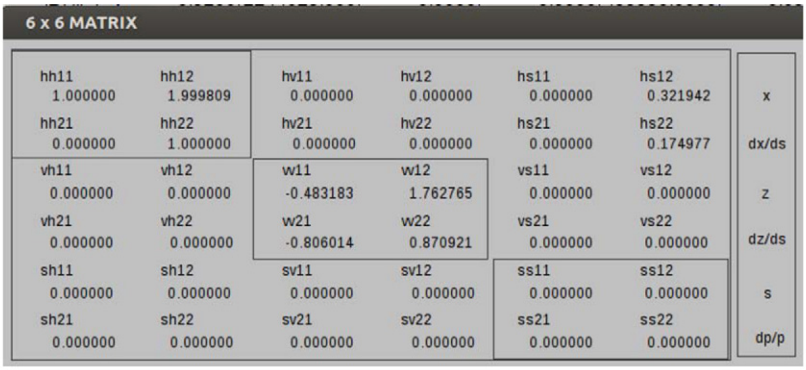
6 x 6 MATRIX

hh11 1.000000	hh12 1.999809	hv11 0.000000	hv12 0.000000	hs11 0.000000	hs12 0.321942	x
hh21 0.000000	hh22 1.000000	hv21 0.000000	hv22 0.000000	hs21 0.000000	hs22 0.174977	dx/ds
vh11 0.000000	vh12 0.000000	vv11 -0.483183	vv12 1.762765	vs11 0.000000	vs12 0.000000	z
vh21 0.000000	vh22 0.000000	vv21 -0.806014	vv22 0.870921	vs21 0.000000	vs22 0.000000	dz/ds
sh11 0.000000	sh12 0.000000	sv11 0.000000	sv12 0.000000	ss11 0.000000	ss12 0.000000	s
sh21 0.000000	sh22 0.000000	sv21 0.000000	sv22 0.000000	ss21 0.000000	ss22 0.000000	dp/p

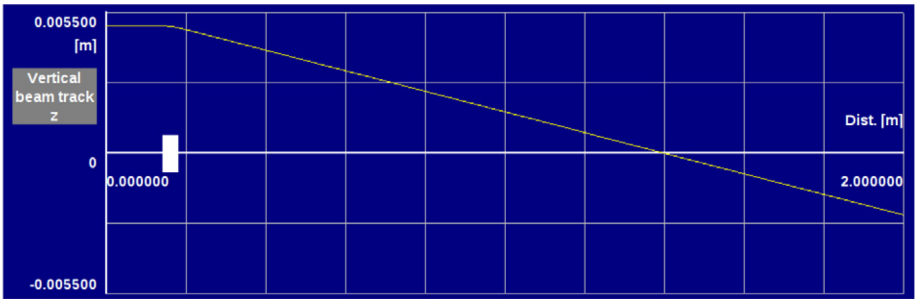

Figure 2.9. Output from Winagile file R-bend.lat. Top: matrix elements. Note in particular the element -vv21; it is the inverse of the focal length in the vertical plane. Particle tracking in the vertical plane is shown on the bottom graph.

output to expect for a rectangular magnet. Furthermore, doing tracking with a particle starting at +0.005 m in the vertical plane illustrates vertical focusing (figure 2.9, bottom).

The Mathcad files **SOLENOID-SmoothAndHE.xmcd**, and **QUAD-SmoothAndHE.xmcd** illustrate the method described in section 2.6 to calculate the effective length and strength of solenoids and quadrupoles with fringe fields. Figures 2.7 and 2.8 for the solenoid case can be reproduced.

References

[1] Wollnik W 1987 *Optics of Charged Particles* (Orlando, FL: Academic)

[2] McDonald K T 2011 Expansion of an axially symmetric, static magnetic field in terms of its axial field (available online)

[3] Kumar V 2009 Understanding the focusing of charged particle beams in a solenoid magnetic field *Am. J. Phys.* **77** 737

[4] Palmer R B 2005 *Solenoid Dynamics* presentation for the PRISM Workshop, Osaka, November, 2005 (available online)

[5] Rosenzweig J B 2003 *Fundamentals of Beam Physics* (Oxford: Oxford University Press)

[6] Reiser M 2008 *Theory and Design of Charged Particle Beams* 2nd edn (New York: Wiley)

[7] Bryant P J and Johnsen K 1993 *The Principles of Circular Accelerators and Storage Rings* (Cambridge: Cambridge University Press)

[8] Steffen K G 1965 *High Energy Beam Optics* (New York: Wiley)

[9] Wiedemann H 2007 *Particle Accelerator Physics* 3rd edn (Berlin: Springer)

[10] Bernal S *et al* 2006 RMS envelope matching of electron beams from ‘zero’ current to extreme space charge in a fixed lattice of short magnets *Phys. Rev. ST Accel. Beams* **9** 064202

IOP Concise Physics

A Practical Introduction to Beam Physics and Particle Accelerators

Santiago Bernal

Chapter 3

Periodic lattices and functions

A periodic lattice consists of a repeating focusing structure composed of one or more lenses, not all necessarily identical, whose function is to allow the transport of charged-particle beams over long distances. The repeating structure or cell constitutes one *lattice period*; the focusing function introduced in chapter 1 then becomes a periodic function. Further, if focusing is *axisymmetric*, focusing of particles occurs with equal strengths (and signs) in both transverse planes; this is the case with a *solenoid lattice*, which requires a single focusing function. We consider a periodic linear solenoid lattice in the first section. Although not commonly used, the solenoid lattice provides a simple system to study stable beam transport and to introduce the *phase advance per period* without space charge. In the second section we analyze the *alternating gradient* (AG) focusing system, which consists of quadrupoles paired with opposite gradient polarities. If the strengths of the quadrupoles are the same (except for the sign), the configuration is called symmetric FODO for 'FOcusing–DefOcusing'. For various reasons, however, it is customary to power the two quadrupoles per FODO cell with different strengths; this case is also considered. In section 3.3, we summarize the classic *Courant–Snyder theory*, the 'bread-and-butter' theory of accelerator physics. In section 3.4, we introduce the *uniform-focusing approximation*, an idealized constant focusing function which is widely used for theoretical and computational studies. Section 3.5 covers *linear dispersion* and section 3.6 additional important concepts especially applicable to rings. Finally, the last section covers computer resources and exercises.

3.1 Solenoid lattice

Focusing by a single solenoid was discussed in section 2.2. The transfer matrix for the solenoid in the Larmor frame of reference can be written as

doi:10.1088/978-1-6817-4076-8ch3

$$\boldsymbol{M}_S = \begin{bmatrix} \cos\theta & \dfrac{l_S}{\theta}\sin\theta \\ -\dfrac{\theta}{l_S}\sin\theta & \cos\theta \end{bmatrix}, \tag{3.1.1}$$

where $\theta = \sqrt{\kappa_S}\, l_S$, κ_S is given in equation (2.2.5) and l_S is the effective length of the solenoid. It is possible to write a matrix that describes the ray transformation in the laboratory frame, i.e. a transformation that includes rotation; the derivation is discussed in the book by Banford [1]. It is implicit in equation (3.1.1) that $\kappa_S \equiv \kappa_S(s)$, i.e. the focusing function can vary with distance. Note that in the limit of small θ, the matrix $\boldsymbol{M}_S$ reduces to the thin lens form given by equation (1.1.5). In that limit, $\cos\theta = 1$, $\sin\theta = \theta$, and $\kappa_S l_S = 1/f$.

Let us now consider N solenoids in a linear configuration and with a spacing L between them. Then, the matrix corresponding to *one period* of the solenoid lattice is the product $\boldsymbol{M}_S\boldsymbol{M}_L$, where $\boldsymbol{M}_L$ is the matrix representing a drift (equation (1.1.6)). Let us write the one-period matrix in the form

$$\boldsymbol{M}_1 = \boldsymbol{M}_S\boldsymbol{M}_L = \begin{bmatrix} A & B \\ C & D \end{bmatrix}, \tag{3.1.2}$$

so a ray $[r_{s+1}, r'_{s+1}]$ at a plane labelled $s+1$ is related to a ray at plane s by

$$\begin{aligned} r_{s+1} &= Ar_s + Br'_s, \\ r'_{s+1} &= Cr_s + Dr'_s. \end{aligned} \tag{3.1.3}$$

From these relations, a *difference equation* can be easily obtained:

$$r_{s+2} - 2br_{s+1} + r_s = 0, \tag{3.1.4}$$

where we have used $b = (A + D)/2 \equiv (1/2)\mathrm{Tr}[\boldsymbol{M}_1]$, and $AD{-}BC = 1$. The symbol Tr stands for 'trace', while the last equality is equivalent to $\det[\boldsymbol{M}_1] = 1$ (see chapter 1 and section A.0 in appendix). We now look for a *periodic ray solution* of the form $r_s = r_0 \mathrm{e}^{\mathrm{i}sq}$ (naturally, only the real—or the imaginary—part of r is physical). When r_s is substituted in equation (3.1.4), we find $\mathrm{e}^{\mathrm{i}q} = b \pm \mathrm{i}\sqrt{1 - b^2}$. By setting $b = \cos\sigma_0$, we see that σ_0 is real and the ray solution is confined if $|b| \leqslant 1$, i.e. if the *trace* of the one-period matrix satisfies

$$|\mathrm{Tr}[\boldsymbol{M}_1]| \leqslant 2. \tag{3.1.5}$$

The quantity σ_0 is the change in phase of the ray when advancing one period; thus, it is called the *phase advance per period*. In practice, the phase advance σ_0 is specified, and the required strength of the magnet is obtained by solving for $\theta = \sqrt{\kappa_S}\, l_S$ the equation

$$\cos\sigma_0 - \frac{1}{2}\mathrm{Tr}[\boldsymbol{M}_1] = 0. \tag{3.1.6}$$

From the product of the solenoid and drift matrices, equations (3.1.1) and (1.1.6), we can identify $A = \cos\theta$, $B = L\cos\theta + (l_S/\theta)\sin\theta$, $C = -(\theta/l_S)\sin\theta$, and $D = \cos\theta - (L\theta/l_S)\sin\theta$, so the condition 3.1.5 is, explicitly,

$$\frac{1}{2}\,|\mathrm{Tr}[\boldsymbol{M}_1]| = \left|\cos\theta - \frac{L\theta}{2l_S}\sin\theta\right| \leqslant 1. \tag{3.1.7}$$

In the limit of thin lenses we have

$$\left|1 - \frac{L}{2f}\right| \leqslant 1, \tag{3.1.8}$$

from which the condition $L \leqslant 4f$ easily follows. In chapter 1 we had found that a combination of positive and negative lenses with the same strength lead to net focusing if their separation is smaller than one focal length. Clearly, the combination of only positive lenses like solenoids allows a greater separation.

As an example, let us consider a periodic lattice with solenoids having an effective length $l_S = 0.065$ m, and a drift space $L = 0.10$ m. If we specify a phase advance per period $\sigma_0 = 30°$, we obtain $\theta = 0.3272$ from equation (3.1.6), and $\kappa_S = 25.35\ \mathrm{m}^{-2}$ (see definitions below equation (3.1.1)). Ray propagation in this lattice is illustrated in figure 3.1.

3.2 FODO lattice

A *symmetrical* FODO lattice is realized with paired quadrupole lenses that have the same strength but opposite gradients (polarities). Figure 3.2 shows a schematic representation of a symmetrical FODO lattice.

In the same vein as equation (3.1.1) for a solenoid lens, a quadrupole that is focusing in the *horizontal* or *x-plane* is represented by the matrix

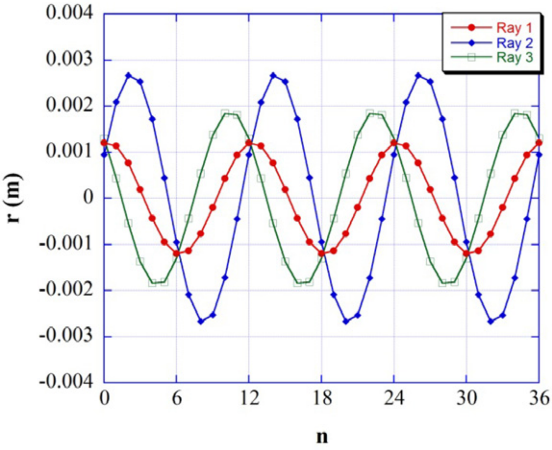

Figure 3.1. Ray propagation in a periodic lattice with 36 solenoids. Three rays with different initial conditions (r_0, r_0') start at $n = 0$. The phase advance per period is $\sigma_0 = 30°$.

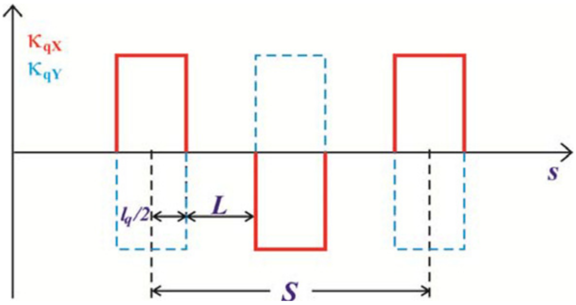

Figure 3.2. Focusing functions of one-and-a-half cells of a symmetrical FODO (FOcusing–DefOcusing) lattice. Notice that $\kappa_{qX} = -\kappa_{qY}$: there is focusing in the horizontal plane and defocusing in the vertical plane. The full-lattice period is S.

$$\boldsymbol{M}_F = \begin{bmatrix} \cos\theta & \dfrac{l_q}{\theta}\sin\theta \\ -\dfrac{\theta}{l_q}\sin\theta & \cos\theta \end{bmatrix}, \tag{3.2.1}$$

where $\theta = +\sqrt{\kappa_q}\, l_q$, κ_q is positive and given by equation (2.3.10) for a magnetic quadrupole, and l_q is the effective length of the quadrupole. If the quadrupole is focusing in the *vertical or y-plane*, it will be *defocusing* in the horizontal plane, with a corresponding matrix given by

$$\boldsymbol{M}_D = \begin{bmatrix} \cosh\theta & \dfrac{l_q}{\theta}\sinh\theta \\ \dfrac{\theta}{l_q}\sinh\theta & \cosh\theta \end{bmatrix}. \tag{3.2.2}$$

Therefore, the matrix corresponding to one symmetrical FODO cell as in figure 3.2 is

$$\boldsymbol{M}_{\text{FODO}} = \boldsymbol{M}_L\boldsymbol{M}_D\boldsymbol{M}_L\boldsymbol{M}_F = \begin{bmatrix} A & B \\ C & D \end{bmatrix}. \tag{3.2.3}$$

Matrix multiplication leads to

$$\begin{aligned} \cos\sigma_0 &= \frac{1}{2}\text{Tr}[M_{\text{FODO}}] \\ &= \cos\theta\cosh\theta + \frac{1}{\eta}\theta[\cos\theta\sinh\theta - \sin\theta\cosh\theta] \\ &\quad - \frac{1}{2\eta^2}\theta^2\sin\theta\sinh\theta, \end{aligned} \tag{3.2.4}$$

with

$$\eta = \frac{l_q}{L} = \frac{l_q}{(S/2) - l_q} \tag{3.2.5}$$

defining the *fill factor*.

As an example, let us consider a *symmetric* periodic FODO lattice with magnetic quadrupoles having an effective length $l_q = 0.0516$ m, and a full-lattice period $S = 0.32$ m. If we specify a phase advance per period $\sigma_0 = 30°$, we obtain $\theta = 0.4341$ from equation (3.2.4), and $\kappa_q = 70.78\ \mathrm{m}^{-2}$ (see definitions below equation (3.2.1)). Note that $\kappa_q = 70.78\ \mathrm{m}^{-2}$ is the value of the focusing (piecewise) constant in the horizontal x-plane; correspondingly, the focusing (piecewise) constant in the vertical y-plane will be $-\kappa_q$. Ray propagation in this lattice is illustrated in figure 3.3 for the x and y components of just one ray.

If the strengths of the 2 quadrupoles in a FODO cell are different, the FODO lattice is *asymmetrical*. The focusing function for such a lattice would be schematically represented as in figure 3.4.

In this case, we need to define separate strength variables θ for the two quadrupoles (figure 3.4): $\theta_1 = +\sqrt{\kappa_1}\, l_q$, $\theta_2 = +\sqrt{\kappa_2}\, l_q$. With these definitions, matrix multiplication as for equation (3.2.3) leads to [2]:

$$\begin{aligned}\cos(\sigma_{0x}) = \cosh(\theta_2)&\left[\cos(\theta_1) - \frac{1}{\eta}\theta_1 \sin(\theta_1)\right]\\ &+ \sinh(\theta_2)\sin(\theta_1)\left[\frac{1}{2}\left(\frac{\theta_2}{\theta_1} - \frac{\theta_1}{\theta_2}\right) - \frac{1}{2\eta^2}\theta_1\theta_2 + \frac{1}{\eta}\theta_2 \cot(\theta_1)\right],\end{aligned} \tag{3.2.6}$$

$$\begin{aligned}\cos(\sigma_{0y}) = \cos(\theta_2)&\left[\cosh(\theta_1) + \frac{1}{\eta}\theta_1 \sinh(\theta_1)\right]\\ &+ \sinh(\theta_1)\sin(\theta_2)\left[\frac{1}{2}\left(\frac{\theta_1}{\theta_2} - \frac{\theta_2}{\theta_1}\right) - \frac{1}{2\eta^2}\theta_1\theta_2 - \frac{1}{\eta}\theta_2 \coth(\theta_1)\right].\end{aligned} \tag{3.2.7}$$

As an example, let us consider a periodic FODO lattice with the same geometry as before but with different quadrupole strengths so that the phase advances per

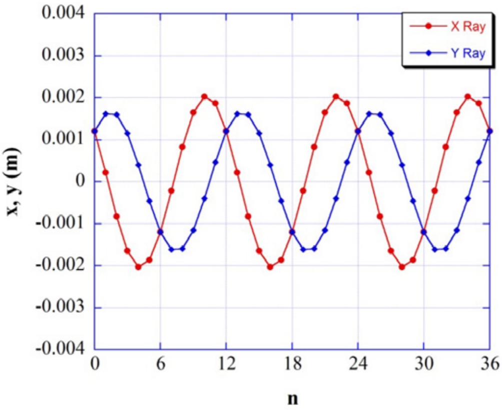

Figure 3.3. Example of ray propagation in symmetrical FODO lattice with 36 periods. Both the x and y components of a ray starting with components $(x_0, x'_0) = (0.0012, 0)$ m, and $(y_0, y'_0) = (0.0012, 0)$ m have phase advances of 30° per period.

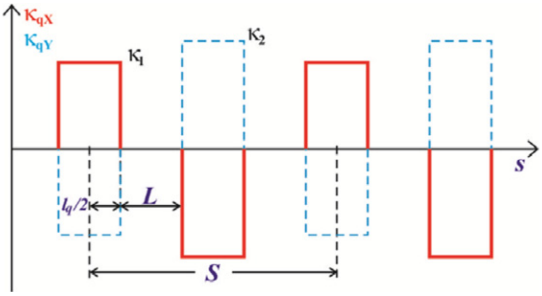

Figure 3.4. Focusing functions of two cells of an *asymmetrical* FODO lattice. Notice that $\kappa_1 \neq \kappa_2$, but still $\kappa_{qX} = -\kappa_{qY}$ for *each* quadrupole.

period in the two transverse planes are $\sigma_{0X} = 30°$, and $\sigma_{0Y} = 45°$. By solving equations (3.2.6) and (3.2.7) simultaneously for θ_1, θ_2, we obtain $\theta_1 = 0.4748$, and $\theta_2 = 0.50135$, which correspond to $\kappa_1 = 84.67\ \mathrm{m}^{-2}$, and $\kappa_2 = 94.40\ \mathrm{m}^{-2}$. Clearly, a stronger second quadrupole in a FODO in the scheme of figure 3.4 is needed for a larger phase advance in the vertical y-plane.

3.3 Lattice and beam functions

The matrix treatment of the previous two sections describing paraxial ray propagation in periodic lattices is equivalent to solving the second-order homogeneous differential equations

$$\begin{aligned} x''(s) + \kappa_x(s)x &= 0, \\ y''(s) + \kappa_y(s)y &= 0. \end{aligned} \tag{3.3.1}$$

For a solenoid lattice, only one equation would be needed, with the function $\kappa(s)$ representing focusing in the radial direction. Inspired by the simple harmonic oscillator equation, the general solution of the first of equations (3.3.1) can be written as

$$x(s) = Cw(s)\cos[\psi(s) + \phi], \tag{3.3.2}$$

where $w(s)$ is the *amplitude function*, $\psi(s)$ is the *phase function*, and C and ϕ are constants that depend on the initial conditions $x(0)$ and $x'(0)$. Differentiation of equation (3.3.2) and substitution into the first of equations (3.3.1) yields

$$\gamma x^2 + 2\alpha x x' + \beta x'^2 = C^2, \tag{3.3.3}$$

where α, β, γ define the *Courant–Snyder* (C–S) [3], or *Twiss* parameters, and C is the *Courant–Snyder invariant*, sometimes also called ‘single-particle emittance’.

The C–S parameters are functions of s and can be related to the amplitude function and its derivative:

$$\beta = w^2, \qquad \alpha = -ww', \qquad \gamma = \frac{1}{w^2} + w'^2. \tag{3.3.4}$$

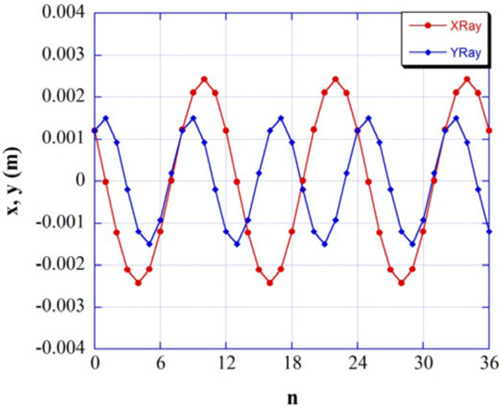

Figure 3.5. Example of ray propagation in *asymmetrical* FODO lattice with 36 periods. The x-component of a ray starting with components $(x_0, x'_0) = (0.0012, 0)$ m, and $(y_0, y'_0) = (0.0012, 0)$ m has a phase advance of 30° per period, while the y-component has a phase advance of 45° per period.

(It will be clear from the context of any discussion whether β and γ refer to the standard relativistic quantities or to the C–S parameters). Only two of the C–S parameters are independent because they are connected by the equation

$$\beta\gamma - \alpha^2 = 1, \tag{3.3.5}$$

which can be easily verified from equation (3.3.4).

Two additional important equations can be easily obtained from equations (3.3.2) and (3.3.1):

$$w''(s) + \kappa_x(s)w(s) - \frac{1}{w(s)^3} = 0, \tag{3.3.6}$$

and

$$\psi'(s) = \frac{d\psi(s)}{ds} = \frac{1}{\beta(s)}. \tag{3.3.7}$$

Equation (3.3.3) represents a tilted ellipse in *trace space* (x, x'), although it is common to call this space 'phase space'. Figure 3.6 shows the ellipse and its relation to the C–S parameters. The ellipse size and shape at a given s are determined by the constant C and coefficients $\alpha(s)$ and $\beta(s)$. In a single-pass machine, a particle is represented by only one point on the ellipse at a given location s. If the structure is periodic, however, the particle coordinates (x, x') will trace the ellipse discontinuously. This is illustrated in figure 3.7 for the periodic solenoid lattice; we have used the same parameters for the calculation of ray propagation illustrated in figure 3.1. Alternatively, we can construct the trace-space ellipses from equation (3.3.3) and the C–S parameters. These parameters can be related to the $ABCD$ matrix in equation (3.1.2) by the following relations:

$$\alpha(s) = \frac{A - D}{2\sin\sigma_0}, \qquad \beta(s) = \frac{B}{\sin\sigma_0}, \qquad \gamma(s) = -\frac{C}{\sin\sigma_0}. \tag{3.3.8}$$

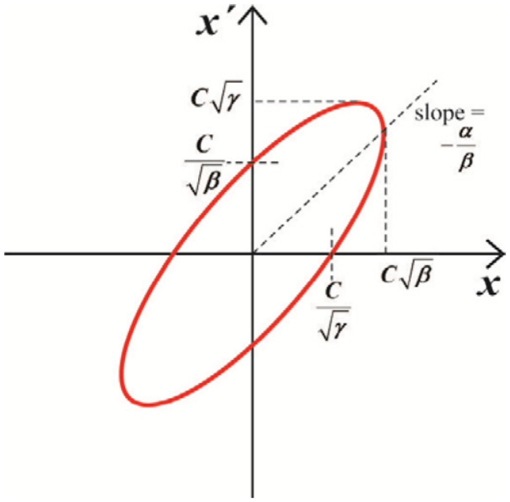

Figure 3.6. Trace-space ellipse (equation (3.3.3) in the horizontal plane at a given location s along the beam line. The size and orientation of the ellipse are related to the C–S parameters (equation (3.3.4)).

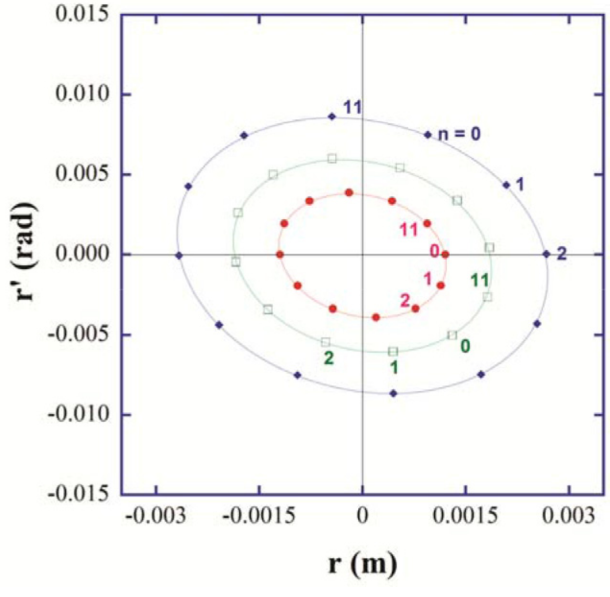

Figure 3.7. Trace-space ellipses corresponding to the rays in figure 3.1 for a periodic solenoid lattice. n is the period number. Note that the points overlap after 12 periods because the phase advance per period is $\sigma_0 = 30°$.

(See also expressions in the discussion before equation (3.1.7)). The values of the C–S invariant C in equation (3.3.3) can be determined from the initial conditions. This is shown numerically in one of the examples mentioned in the section on ‘Computer Resources’ below. The relations in equations (3.3.8) are a special case of the general matrix for *linear* ray transformation between two planes 1 and 2 in terms of the corresponding C–S parameters:

$$\boldsymbol{M}_{1\to2} = \begin{bmatrix} \sqrt{\dfrac{\beta_2}{\beta_1}}(\cos\Delta\psi + \alpha_1\sin\Delta\psi) & \sqrt{\beta_2\beta_1}\sin\Delta\psi \\ \dfrac{(\alpha_1-\alpha_2)\cos\Delta\psi - (1+\alpha_1\alpha_2)\sin\Delta\psi}{\sqrt{\beta_2\beta_1}} & \sqrt{\dfrac{\beta_1}{\beta_2}}(\cos\Delta\psi - \alpha_2\sin\Delta\psi) \end{bmatrix}, \tag{3.3.9}$$

where $\Delta\psi$ is the phase advance from plane 1 to plane 2. The derivation of equation (3.3.9) employs equation (3.3.2) and its derivative; details can be found in many textbooks (e.g. [4, 5]).

So far, we have discussed the propagation of a single particle or ray. In a particle *beam*, different particles will have different values of C and phase ϕ, leading to different ellipse sizes at a location s. But the functions $\alpha(s)$ and $\beta(s)$ depend entirely on the lattice geometry and magnet strengths through the function $\kappa_x(s)$, and for this reason are called *machine* or *lattice functions*.

The general solution equation (3.3.2) is valid for periodic or non-periodic lattices; only when $\kappa_x(s) = \kappa_x(s+S)$, we have periodic focusing. Naturally, in this latter case the C–S parameters are also periodic, indicating that *at a given instant* the trace-space ellipse repeats itself with period S along the reference trajectory. But a beam injected into a periodic system will not follow the machine ellipse unless the beam is *matched*. When the beam is mismatched, we can still define *beam functions* $\alpha_B(s)$, $\beta_B(s)$, $\gamma_B(s)$ and a corresponding *beam ellipse*, to be distinguished from the *machine* (or *lattice*) counterparts. The beam functions can be identified with those of the particle with the maximum C–S invariant, but a proper discussion of beam matching normally involves the *beam emittance* and a *beam ellipse* in the manner described in chapter 6.

3.4 Uniform-focusing ('smooth') approximation

From equation (3.3.7) we can write an expression for the single-particle *phase advance per period*, introduced in section 3.1 in the matrix treatment of the solenoid lattice but now made more general in the context of the Courant–Snyder theory:

$$\sigma_0 = \int_{\text{Per.}} \psi'(s)\,\mathrm{d}s = \int_{\text{Per.}} \frac{\mathrm{d}s}{\beta(s)}. \tag{3.4.1}$$

Furthermore, we can substitute an effective *uniform-focusing lattice* for the periodic lattice. The uniform-focusing lattice will have a constant focusing function κ_0 and constant amplitude function w. If we set $w'' = 0$, we find from equation (3.3.6) an expression for κ_0 in terms of the constant amplitude function, or the betatron parameter β:

$$\kappa_0 = \frac{1}{w^4} = \frac{1}{\beta^2}. \tag{3.4.2}$$

Now we can relate the phase advance per period of the actual lattice (with period S) to the constant focusing function of the uniform-focusing lattice.

From equation (3.4.1), the integral over one period of the inverse betatron function can be written as:

$$\sigma_0 = \frac{S}{\bar{\beta}} = S\sqrt{\kappa_0}\,. \tag{3.4.3}$$

Finally, we introduce $k_0 \equiv \sqrt{\kappa_0}$, so $\sigma_0 = k_0 S$. An additional related concept, the *betatron tune* or number of betatron oscillations per turn, can be defined for a circular lattice of radius R_m:

$$\nu_0 = \frac{1}{2\pi}\oint\frac{\mathrm{d}s}{\beta(s)} = \frac{R_\mathrm{m}}{\bar{\beta}}, \tag{3.4.4}$$

which can be written also as $k_0 = \nu_0/R_\mathrm{m}$.

The uniform-focusing or 'smooth' approximation is a very useful construction for theoretical as well as computational studies in accelerator and beam physics. We will return to this model when we consider emittance and space charge in the next chapter.

3.5 Linear dispersion

The single-particle equations of motion, equations (3.3.1), assume mono-energetic particles so that the focusing represented by $\kappa(s)$ is defined for a single momentum p_0. If, however, there is a momentum spread Δp around the design value p_0, the equations are modified. For the horizontal motion (radial in a circular machine) we have the inhomogeneous equation (see e.g., [6] page 46):

$$x''(s) + \kappa_x(s)x = -\frac{1}{R(s)}\delta, \tag{3.5.1}$$

where $\delta = \Delta p/p_0$, and $R(s)$ is the *local* orbit radius. A major assumption here is that $x(s) \ll R(s)$, so we can neglect the *weak focusing* term $1/R^2$ discussed in section 2.4. It is straightforward to show, from the definition of magnetic rigidity in equation (2.1.2), that the momentum error is equivalent to a magnet error, i.e. $\Delta p/p_0 = \Delta B/B_0$. The general solution of equation (3.5.1) is

$$x(s) = x_\beta(s) + D_x(s)\delta, \tag{3.5.2}$$

where $x_\beta(s)$is the solution of the *homogeneous* equation (3.3.1), and $D(s)$ defines the *linear dispersion function*. $D(s)$ satisfies the equation (see e.g. [6] page 49)

$$D_x''(s) + \left[\frac{1}{R^2(s)} - \kappa_x(s)\right]D_x(s) = -\frac{1}{R(s)}. \tag{3.5.3}$$

Normally, the weak focusing term $1/R^2(s)$ can be neglected as in equation (3.5.1). Thus, using the smooth-approximation whereby $D_x''(s) \to 0$, we obtain for the *average dispersion*:

$$\bar{D}_x = \frac{1}{\kappa_x R_\mathrm{m}} = \frac{R_\mathrm{m}}{\nu_0^2}, \tag{3.5.4}$$

the last equality following results from the previous section. Therefore, larger circular machines normally need to operate at larger tunes to reduce dispersion effects. Note the resemblance of equation (3.5.4) to the equation for the average beta function $\bar{\beta} = R_{\mathrm{m}}/\nu_0$, from equation (3.4.4). In circular machines, the term $x_\beta(s)$ in equation (3.5.2) defines the design *reference orbit*; with momentum error, the dispersion function can be interpreted as the reference orbit for *off-momentum* particles.

3.6 Momentum compaction, transition gamma, and chromaticity

In general, the change in orbit radius due to a momentum error cannot be neglected. Thus, we define the *momentum compaction factor* as the fractional change in equilibrium radius per fractional change in momentum:

$$\alpha_c \equiv \frac{\mathrm{d}R/R_0}{\mathrm{d}p/p_0}, \tag{3.6.1}$$

with p_0, R_0 defining design values. Rewriting equation (2.1.2) for the magnetic rigidity in the form

$$R(p, B) = \frac{p}{qB}, \qquad R_0 = \frac{p_0}{qB_0}, \tag{3.6.2}$$

and taking logarithmic derivatives on both sides we get $\mathrm{d}R/R_0 = \mathrm{d}p/p_0 - \mathrm{d}B/B_0$. (Note that we are evaluating the derivatives, i.e., $\partial R/\partial p$, $\partial R/\partial B$, at the equilibrium values p_0, R_0). Therefore, by using the definition of the *field index*, equation (2.4.3), we find:

$$\frac{\mathrm{d}R}{R_0}(1 - n) = \frac{\mathrm{d}p}{p_0}. \tag{3.6.3}$$

The momentum compaction is then

$$\alpha_c = \frac{1}{1 - n}. \tag{3.6.4}$$

Further, if C denotes the length of the orbit over the beam line for a particle of coordinate x, and C_0 is the length of the reference orbit (for which $x = 0$ by definition), then $\alpha_c = (\mathrm{d}R/R_0)\delta^{-1} = (\mathrm{d}C/C_0)\delta^{-1}$, and to first order in x we can write (see e.g. [7], or [4]):

$$\alpha_c = \frac{1}{C_0}\int_0^{C_0} \frac{D_x}{\rho(s)}\mathrm{d}s, \tag{3.6.5}$$

since $\mathrm{d}C = C - C_0 = \int_0^{C_0}(x/\rho)\mathrm{d}s$, ($\rho(s) = R(s)$ = local radius of curvature), and $x = D_x\delta$, from equation (3.5.2) with $x_\beta = 0$.

Furthermore, because of the change in R there are corresponding changes in the revolution period $T = 2\pi R/\beta c$ and angular frequency $\omega = \beta c/R$. Taking logarithmic derivatives in the equation for ω we get $\mathrm{d}\omega/\omega_0 = \mathrm{d}\beta/\beta_0 - \mathrm{d}R/R_0$. The second term is $\mathrm{d}R/R_0 = \alpha_c \mathrm{d}p/p_0$, from equation (3.6.3), while the first term is $\mathrm{d}\beta/\beta_0 = \gamma_0^{-2}\mathrm{d}p/p_0$, which follows from the definition of the relativistic mass factor γ, and $\mathrm{d}\gamma/\gamma_0 = \beta_0\gamma_0^2\mathrm{d}\beta$ [8]. Finally, the fractional change in period is

$$\frac{\mathrm{d}T}{T_0} = -\frac{\mathrm{d}\omega}{\omega_0} = \eta_{\mathrm{tr}}\frac{\mathrm{d}p}{p_0}, \quad \text{with} \quad \eta_{\mathrm{tr}} = \alpha_c - \frac{1}{\gamma_0^2}. \tag{3.6.6}$$

The momentum compaction also defines a *transition gamma*, γ_t:

$$\gamma_t = \frac{1}{\sqrt{\alpha_c}}. \tag{3.6.7}$$

In a straight machine, $\alpha_c = 0$, $\gamma_t \to \infty$, $\eta_{\mathrm{tr}} = -1/\gamma_0^2$: at all energies particles with higher momentum take less time to traverse a given distance. In circular machines, the same would apply for energies such that $\gamma_0 < \gamma_t$. However, there are situations where, counterintuitively, particles with higher momentum take *more* time to complete a revolution, i.e. $\eta_{\mathrm{tr}} > 0$, or $\gamma_0 > \gamma_t$. This is the regime of 'negative mass' of weak focusing machines such as cyclotrons, or strong focusing circular machines above transition energy. For cyclotrons we have $0 < n < 1$, $\nu_r < 1$ (equation (2.4.7)), while $\nu_r > 1$ for strong focusing machines.

In circular machines, another effect of a momentum error δ is to change the *tunes* in both the radial and vertical planes. Horizontal and vertical *chromaticities*, $\boldsymbol{\xi}_X$, $\boldsymbol{\xi}_Y$, are defined to characterize the effect:

$$\Delta\nu_X = \xi_X\delta, \qquad \Delta\nu_Y = \xi_Y\delta. \tag{3.6.8}$$

The focusing of particles with higher momentum is less efficient, leading to reduced tunes. Therefore, we expect the chromaticity from linear elements such as dipoles and quadrupoles to be negative.

In a weak focusing machine where $\partial B_y/\partial R$ is constant, the field index satisfies $\mathrm{d}n/\mathrm{d}R = n(1 + n)/R$ (see Reiser) and we find:

$$\xi_X = -\frac{n(n+1)}{2(1-n)^{3/2}}, \qquad \xi_Y = -\frac{\sqrt{n}(n+1)}{2(1-n)}. \tag{3.6.9}$$

Note that in Reiser's book [9] the chromaticity is defined in terms of fractional quantities $\Delta\nu_X/\nu_X$, $\Delta\nu_Y/\nu_Y$ instead of just $\Delta\nu_X$, $\Delta\nu_Y$.

A more general definition of chromaticity, referred to as the *natural chromaticity* is

$$\xi_X = -\frac{1}{4\pi}\oint\beta_x(s)\kappa_x(s)\mathrm{d}s, \qquad \xi_Y = \frac{1}{4\pi}\oint\beta_y(s)\kappa_x(s)\mathrm{d}s, \tag{3.6.10}$$

where only linear focusing elements are involved. We will encounter a related expression in chapter 4 when we discuss the effects of linear space charge on betatron tune.

Computer resources

Two Mathcad files, **Sol_Lattice.xmcd**, and **Quad_Lattice.xmcd** provide the tools for obtaining the ray and trace-space plots in this chapter. In addition, input files for the popular code MAD8 and ELEGANT are included for calculating lattice functions in an example. Additional examples are given in chapter 6 for linacs and rings.

References

[1] Banford A P 1966 *The Transport of Charged Particle Beams* (London: E & F N Spon)

[2] Bernal S *et al* 2006 RMS envelope matching of electron beams from 'zero' current to extreme space charge in a fixed lattice of short magnets *Phys. Rev. ST Accel. Beams* **9** 064202

[3] Courant E D and Snyder H S 2000 Theory of the alternating-gradient Synchrotron *Ann. Phys.* **281** 360–408 (reprint of original 1958 article)

[4] Wille K 2000 *The Physics of Particle Accelerators, An Introduction* (New York: Oxford University Press)

[5] Edwards D A and Syphers M J 2004 *An Introduction to the Physics of High Energy Accelerators* (New York: Wiley)

[6] Bryant P J and Johnsen K 1993 *The Principles of Circular Accelerators and Storage Rings* (Cambridge: Cambridge University Press)

[7] Wolski A 2014 *Beam Dynamics In high Energy Particle Accelerators* (London: Imperial College Press)

[8] Bovet C, Gouiran R, Gumowski I and Reich K R 1970 A selection of formulae and data useful for the design of A.G. synchrotrons *CERN Technical Note DL/70/4*

[9] Reiser M 2008 *Theory and Design of Charged Particle Beams* 2nd edn (New York: Wiley)

A Practical Introduction to Beam Physics and Particle Accelerators

Santiago Bernal

Chapter 4

Emittance and space charge

The description of the evolution of beams in accelerators and other devices must be extended beyond the single-particle dynamics concepts of the previous three chapters. The first concept we encounter is the *particle distribution* in phase or trace space. For particle ensembles satisfying Hamilton's equations of motion, i.e. systems without dissipation (from radiation or collisions) or particle losses, the evolution of any representative region in phase space is similar to the motion of an incompressible fluid. This is in essence a statement of *Liouville's theorem*, introduced in section 3.1. Then, we discuss *beam emittance*, which is related to area in phase space and thus invariant if the conditions for Liouville's theorem are satisfied. In practice, however, *root-mean-square (rms) emittance* is used, a beam quality factor that can be shown to be conserved under linear transformations and without acceleration. In section 3.2 we give a simple treatment of the Kapchinskij–Vladimirskij (K–V) and thermal distributions, which are mathematical constructs widely used in beam physics to model real distributions. In section 3.3 we derive the *K–V envelope equations*, which embody the simplest macroscopic beam dynamics of *direct ('incoherent') space charge* in a uniform-focusing lattice. From the K–V envelope equations, we derive in section 3.4 the expression for the *tune shift* caused by direct space charge (incoherent tune shift) for beams of circular and elliptical cross sections. Lastly, in section 3.5 we discuss the change in tune caused by image forces (coherent tune shift). In presenting the expressions for space-charge tune shifts we use the language of the standard literature as well as the notation of more specialized books such as Reiser's [1]. Most illustrations and examples are covered in computer exercises described briefly at the end of the chapter.

4.1 Liouville's theorem and emittance

We mentioned in chapter 3 that the ellipse represented in equation (3.3.3) and shown in figure 3.6 is a particle's orbit in (x, x') space, i.e. 'trace' space. More generally,

doi:10.1088/978-1-6817-4076-8ch4

non-interacting particles in a beam occupy a 6-dimensional phase space formed by three space coordinates and three canonical momenta, or (x, y, z, p_x, p_y, p_z). It can be shown from Hamiltonian mechanics that the *density of particles* or the volume occupied by a number of particles in phase space is invariant. These are statements of Liouville's Theorem; its derivation (see e.g. section 3.2 in [1]) corresponds essentially to showing that the evolution of particles in phase space is similar to the motion of an incompressible fluid. If the particles interact, the concept can be extended to a $6N$-dimensional space, where N is the number of particles, but we will retain the use of the simpler 6-dimensional space.

Furthermore, if the motions along the 3 coordinate directions are uncoupled, we can consider the projection of the 6-dimensional phase space onto any plane, such as was done with the ellipse in figure 3.6 for the (x, x') plane. Therefore, we can state Liouville's theorem for the (x, x') plane in the form

$$\iint \mathrm{d}x\mathrm{d}x' = \frac{1}{p}\iint \mathrm{d}x\mathrm{d}p_x = \text{const.}, \tag{4.1.1}$$

where $p = \gamma m\beta c$, and similarly for the vertical (y, y') plane (β, γ now stand for the relativistic parameters). Now, an ellipse of the general form $ax^2 + 2bxy + cy^2 = d^2$ encloses an area equal to $\pi d^2/\sqrt{ac - b^2}$; therefore, the area enclosed by the ellipse in figure 3.6 is equal to $A = \pi C^2$ (not in m^2 but in 'm' units, as x' is dimensionless) after using equation (3.3.5). If the ellipse represents the trajectory in trace space of the particle with the *maximum amplitude* C in an ensemble of particles, the ratio A/π is identified as the beam *emittance*:

$$\varepsilon_x = \frac{\pi C^2}{\pi} = C^2. \tag{4.1.2}$$

We will adopt this definition which can be found in many other books (e.g. [1, 2]). An alternative definition of emittance, adopted by e.g. [3], *includes the factor of* π, in which case

$$\varepsilon_x = A = \pi C^2, \quad (\textit{alternative definition}). \tag{4.1.3}$$

Very often the units are quoted in the form 'π-mm-mrad', but there is no fundamental reason for factoring π. Unfortunately, the lack of consensus in the definition of emittance is a source of great confusion.

Since it is not possible in practice to establish the maximum amplitude of particle trajectories, a definition of emittance very often relies on assuming a *Gaussian distribution* for particle positions and momenta. In the (x, p_x) plane, we have:

$$f(x, p_x) = \frac{1}{2\pi\sigma_x\sigma_{p_x}} \exp\left(-\frac{x^2}{2\sigma_x^2} - \frac{p_x^2}{2\sigma_{p_x}^2}\right), \tag{4.1.4}$$

where σ_x, σ_{p_x} represent *standard deviations*, and we have assumed that the average values of x and p_x are zero, which is the case for distributions around design values. The constant in front of the exponential function in equation (4.1.4) assures us that

$\iint f(x, p_x)\, \mathrm{d}x\mathrm{d}p_x = 1$. Furthermore, from figure 3.6, the maximum value of x is $C\sqrt{\beta_x}$. Therefore, if we identify this value with σ_x, we can also write for the *emittance*, following the definition in equation (4.1.2),

$$\varepsilon_x = \frac{\sigma_x^2}{\beta_x}. \tag{4.1.5}$$

From Liouvilles's theorem as stated in equation (4.1.1), emittance decreases as $1/p$, or as $1/\beta\gamma$. Therefore, emittance in Hamiltonian beam transport is conserved only without acceleration or emission of radiation (see also chapter 5). However, we can define a conserved quantity, *normalized emittance*, by multiplying by $\beta\gamma$ (β, γ are the relativistic parameters):

$$\varepsilon_{xn} = \beta\gamma\varepsilon_x. \tag{4.1.6}$$

Without a sharp elliptical boundary, we would like to express the emittance as the product of spreads in both x and x' as if we had an elliptical *upright* boundary: $\tilde{\varepsilon}_x = 2\sigma_x 2\sigma_{x'}$. In general, however, we expect that a *statistical definition* of emittance will involve a correlation term of the form $x\, x'$, because the hypothetical boundary will not be upright but rotated. As shown in detail in [4], the *effective* or 4 × root-mean-square, or *4-rms emittance* is

$$\tilde{\varepsilon}_x \equiv 4\varepsilon_{x\mathrm{rms}} = 4\sqrt{\langle x^2\rangle\langle x'^2\rangle - \langle xx'\rangle}, \tag{4.1.7}$$

where the angular brackets $\langle\rangle$ stand for average in phase space. For example,

$$\langle x^2\rangle = \sigma_x^2 = \frac{1}{N}\sum_{i=1}^{N}(x_i - \langle x\rangle)^2,\ \langle xx'\rangle = \frac{1}{N}\sum_{i\neq j}^{N}\sum_{j=1}^{N}(x_i - \langle x\rangle)\big(x_j' - \langle x'\rangle\big), \tag{4.1.8}$$

for N particles. Note that if the correlation term $\langle xx'\rangle = 0$, we regain the expression $\tilde{\varepsilon}_x = 2\sigma_x 2\sigma_{x'}$

To conclude this section, we present an example of a simple trace-space distribution and its evolution in linear and non-linear focusing channels. The particles originate from a *point source* located at $s = 0$. Thus, the initial trace space is a vertical line in (x, x') space, i.e. with no spread in x values but some range in initial trajectory slopes. The particles are emitted with initial divergence values x' assigned *randomly* between -1 and 1 rad. In addition, the particles are focused by a *linear* uniform-focusing channel with focusing constant $\kappa_0 = 100\ \mathrm{m}^{-2} = k_0{}^2$. The trace space line rotates clockwise and completes half a revolution after a distance $s = \lambda_0/2 = \pi/k_0 = 0.314$ m. Figure 4.1(a) depicts the rotation of the trace space line formed by 100 particles. Note that the rotation spans an oval, but that the area occupied by the particles as well as the emittance is zero. If focusing is non-linear, with third order terms of the form $k_0{}^4x^3$ and $k_0{}^2x'^2x$ added to the linear focusing $k_0{}^2x$, the trace space lines twist as they rotate, eventually spiraling in and occupying an apparent larger area. Figures 4.1(b) and 4.1(c) illustrate the trace-space evolution. The area occupied by the particles as well as the standard emittance is still zero, but the rms emittance now has a non-zero value: the effective emittance, as defined in equation (4.1.7) is 0.020 m after a distance equal

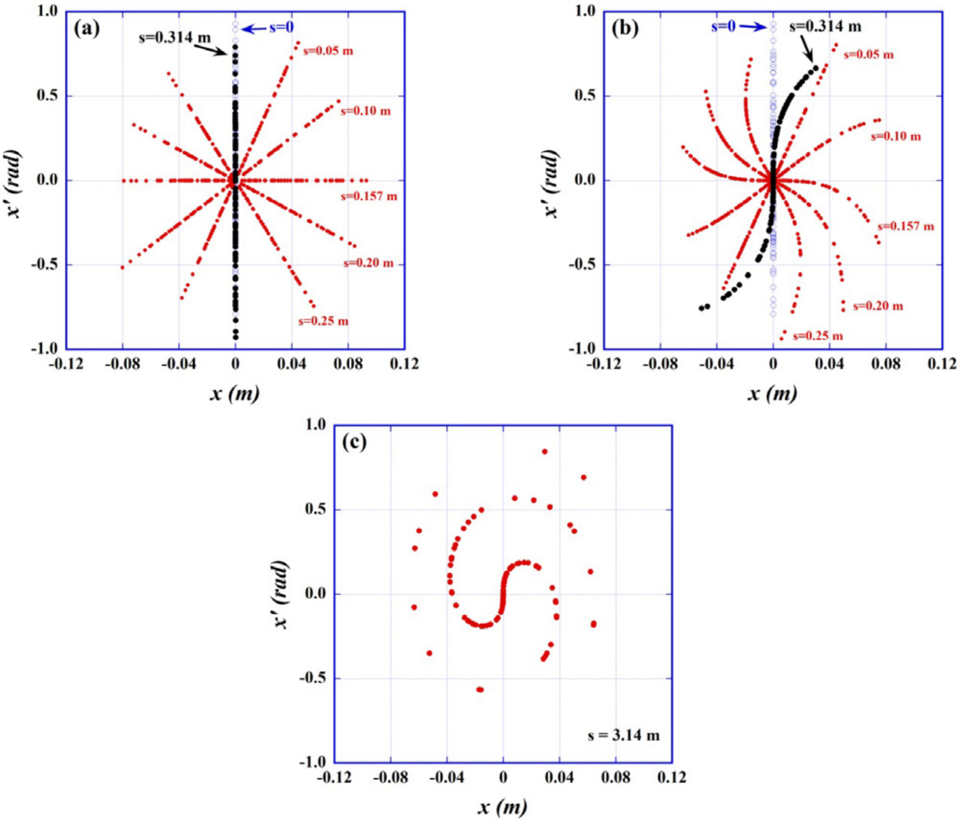

Figure 4.1. Evolution of the trace space of 100 particles originating from a point source at $s = 0$ and moving in (a) *linear* uniform-focusing channel; (b) *non-linear* (cubic) but otherwise uniform-focusing channel; and (c) trace space in non-linear channel after 5 betatron wavelengths. See text and Mathcad programs in website.

to $\lambda_0/2$, and 0.027 m after a distance equal to $5\lambda_0$. These rather large emittance values stem from the assumed large initial spread in trajectory slopes; for the linear channel, on the other hand, the effective emittances are 2×10^{-5} m and 3×10^{-4} m after $s = \lambda_0/2$ and $5\lambda_0$, respectively. The calculations and figures can be reproduced using the accompanying Mathcad programs. We will consider additional trace-space distributions in the following section.

In many applications of accelerators it is important to have beams with small cross section and beam divergence. Thus, a great deal of accelerator technology is devoted to controlling and minimizing rms emittance. From Liouville's theorem alone, emittance as an area in phase space (or in trace space, but without acceleration) is conserved for Hamiltonian *linear or non-linear processes*. The rms emittance, on the other hand, is conserved only under linear transformations, such as the transformation of coordinates and slopes in equation (1.1.3) (see also [5]). The non-linearities originate in most cases from the focusing magnets, but they may also arise from space charge forces. A detailed account of these and other mechanisms of rms emittance growth and theoretical models can be found in chapter 6 of [1].

4.2 The Kapchinskij–Vladimirskij (K–V) and thermal distributions

Let us consider a continuous, axially-symmetric beam with constant particle volume density n_0 (in m^{-3}) within a radius $r = a$. In addition, let us assume that all particles have the same energy and longitudinal velocity $v = \beta c$, with no energy or longitudinal velocity 'errors' or spreads. The beam is kept together by an external *uniform-focusing lattice* characterized by a focusing constant k_0 (in m^{-1}). As we will discover, this arrangement is self-consistent if the beam is 'matched' to the lattice, i.e. if a, n_0, and k_0 are properly chosen. The corresponding particle distribution is an example of a 2D Kapchinskij–Vladimirskij distribution, or K–V for short. The K–V distribution is a mathematical construct that can be employed to model transport of real particle beam distributions with elliptical symmetry ([1, 6]). Mathematically we have,

$$f_{\text{K-V}}(p_\perp, r) = \frac{n_0}{2\pi\gamma m}\delta\left[H_\perp(p_\perp, r) - H_0\right], \tag{4.2.1}$$

where δ is a Dirac delta function, H_0 is the constant transverse energy, and $H_\perp(p_\perp, r)$ is the transverse Hamiltonian given by:

$$H_\perp(p_\perp, r) = \frac{1}{2}\frac{p_\perp^2}{\gamma m} + \frac{1}{2}\gamma m v^2 k_0^2 r^2 + q\phi(r). \tag{4.2.2}$$

In equation (4.2.2), $p_\perp^2 = p_x^2 + p_y^2$, $r^2 = x^2 + y^2$, and $q\phi(r)$ the self-potential energy from *linear* space charge for particles of charge 'q'. We can imagine a uniform background of opposite charge to provide a physical basis for the model; magnetic (solenoid) focusing, on the other hand, can be accommodated if the dynamics is described in the Larmor frame (see chapter 3).

From Gauss' law, the self-potential *inside* the beam of radius 'a' can be easily found to be

$$\phi(r) = -\frac{q n_0}{4\varepsilon_0}r^2, \quad 0 \leqslant r \leqslant a. \tag{4.2.3}$$

For later reference, we define the *generalized beam perveance* K by

$$K = \left(\frac{n_0 q^2}{2\varepsilon_0 \gamma^3 m}\right)\frac{a^2}{\beta^2 c^2} = \frac{\omega_p^2}{2}\frac{a^2}{\beta^2 c^2}, \tag{4.2.4}$$

where ω_p is the *plasma frequency*, implicitly defined in equation (4.2.4). Thus, we have

$$q\phi(r) = -\frac{\gamma^3 m v^2 K}{2}\left(\frac{r}{a}\right)^2, \quad 0 \leqslant r \leqslant a, \tag{4.2.5}$$

The generalized perveance K can be expressed in terms of the (squared) *wave-number* of plasma oscillations $k_p^2 = \omega_p^2/v^2$, so $K = k_p^2 a^2/2$. Finally, we can re-write the transverse Hamiltonian in equation (4.2.2) in the convenient form

$$H_{\perp}(p_{\perp}, r) = \frac{1}{2}\frac{p_{\perp}^2}{\gamma m} + H_0\left(\frac{r}{a}\right)^2, \qquad H_0 = \frac{1}{2}\gamma m v^2 a^2\left(k_0^2 - \frac{\gamma^2 k_p^2}{2}\right). \tag{4.2.6}$$

An alternative form for the K–V particle distribution in equation (4.2.1) is then

$$f_{\text{K–V}}(p_{\perp}, r) = \frac{n_0}{2\pi\gamma m}\delta\left[\frac{1}{2}\frac{p_{\perp}^2}{\gamma m} - H_0\left(1 - \frac{r^2}{a^2}\right)\right]. \tag{4.2.7}$$

Using cylindrical coordinates in $(p_{\perp}, r)$ space and the properties of the δ function, we verify from equation (4.2.7) the normalization of the K–V distribution:

$$2\pi\int f_{\text{K–V}}p_{\perp}\,\mathrm{d}p_{\perp} = 2\pi\gamma m\int f_{\text{K–V}}\,\mathrm{d}\left(\frac{p_{\perp}^2}{2\gamma m}\right) = n_0, \quad 0 \leqslant r \leqslant a. \tag{4.2.8}$$

Furthermore, the *transverse kinetic temperature* in energy units is

$$T_{\perp\text{kin}} = \frac{2\pi}{n_0}\int f_{\text{K–V}}\left(\frac{p_{\perp}^2}{2\gamma m}\right)p_{\perp}\,\mathrm{d}p_{\perp} = H_0\left(1 - \frac{r^2}{a^2}\right), \quad 0 \leqslant r \leqslant a. \tag{4.2.9}$$

The transverse kinetic temperature has a *parabolic profile*, being maximum on axis, $r = 0$, and zero at the beam edge $r = a$.

The K–V distribution is an example of a *micro-canonical* distribution in statistical mechanics, i.e. a particle distribution constructed for an isolated system at constant energy. However, other related concepts from statistical mechanics such as *partition function* are rarely discussed in connection with charged-particle beams because of problems to identify dynamical 'states' for interacting particles in a beam even in the simple context of the K–V distribution. More generally, there are conceptual difficulties for the use of statistical thermodynamics in beam physics (see [7]).

Another widely used concept in describing charged-particle beams is the *Boltzmann factor* $\exp(-H_{\perp}/k_B T_{\perp})$. Here $H_{\perp}$ is the transverse Hamiltonian of equation (4.2.6) and $T_{\perp}$ the *transverse temperature*, normally much larger than the *longitudinal temperature* (see [1], chapter 6). The *canonical ensemble* is implicit in this picture, but no discernible *heat bath*, which is a key component of the ensemble, is present. Therefore $T_{\perp}$ cannot be a thermodynamic temperature, but simply a *kinetic parameter* characterizing the spread of energies in a *model* distribution. More importantly, a beam may evolve towards an equilibrium described by an effective *Maxwell–Boltzmann (M–B) distribution*, but such equilibrium cannot be rigorously characterized as *thermodynamic equilibrium*.

As implied at the beginning of this section, the uniform-focusing approximation is employed to simplify the study of transport of continuous (i.e. 'unbunched') round beams in the presence of significant space charge. Under these circumstances, equilibrium transverse distributions are derived that have non-analytic spatial transverse profiles at given transverse temperatures (see [1], chapter 5). In the limit $T_{\perp} \to 0$, i.e. the *space charge or laminar limit*, the equilibrium distribution is a K–V distribution, which, as we have seen, is uniform in both spatial and velocity coordinates. This limit can also be considered as the 'zero emittance' limit. However, as we will see below, an equivalent K–V distribution can be defined for *any* combination of emittance and perveance. Furthermore, the limit $T_\perp \to 0$ refers to the limit of an M–B distribution; the kinetic temperature, on the other hand, is only zero at the beam edge (equation (4.2.9)).

In the limit of high temperature (or 'zero current') $T_\perp \to \infty$ *Gaussian (thermal) distributions* in both spatial and velocity coordinates are obtained. The spatial profile will have the form of equation (4.1.4), except that $r = \sqrt{x^2 + y^2}$ would be substituted for 'x'. The velocity profile, on the other hand, is Gaussian at all temperatures.

The total, or 100%, and rms emittances in the K–V distribution can be easily shown to be related by ([1], chapter 5):

$$\varepsilon_x = 4\varepsilon_{x\text{rms}} \equiv \tilde{\varepsilon}_x, \quad \text{K–V distribution.} \tag{4.2.10}$$

For a Gaussian distribution, on the other hand, no 100% emittance can be defined because the tails extend to infinity. If the distribution is truncated at n standard deviations σ_x, however, the truncated and rms emittances are related by:

$$\varepsilon_x(n) = n^2\varepsilon_{x\text{rms}}, \quad \text{Gaussian distribution.} \tag{4.2.11}$$

Following this prescription the expression in equation (4.1.5) corresponds to $n = 1$, or 39% of particles: $a^2 \cong \sigma_x^2$. From [3] (chapter 3) we find that the fraction of particles F within $n\sigma_x$ is:

$$F = 1 - \exp(-n^2/2). \tag{4.2.12}$$

For protons, for example, it is customary to use either the 87% ($n = 2.0$) emittance, or the 95% ($n = 2.45$) emittance. We find:

$$\varepsilon_x(87\%) = \frac{4\sigma_x^2}{\beta_x}, \quad \varepsilon_x(95\%) = \frac{6\sigma_x^2}{\beta_x}. \tag{4.2.13}$$

The beam radius squared corresponding to 95% of particles in the Gaussian distribution is $a^2 \cong 6\sigma_x^2$.

4.3 The K–V envelope equations and space-charge (SC) intensity parameters

With *linear* transverse space charge forces arising from a K–V distribution, we can derive an equation governing the evolution of the rms beam radius in a linear uniform-focusing channel. From $x''(s) = -k^2x(s)$, and $X(s) \equiv \sqrt{\langle x^2 \rangle} = \sigma_x$, where the 'spring constant' k includes *both* external focusing and internal ('direct') space charge, we find, after straightforward differentiation,

$$X''(s) + k^2X(s) - \frac{\varepsilon_{x\text{rms}}^2}{X^3(s)} = 0. \tag{4.3.1}$$

The unnormalized rms emittance $\varepsilon_{x\mathrm{rms}}$ is related to the effective emittance by $\varepsilon_{x\mathrm{rms}} = \tilde{\varepsilon}_x/4$ (equation (4.1.7)). Equation (4.3.1) is related to equation (3.3.6) for the amplitude function $w(s)$ of the Courant–Snyder theory discussed in section 3.3. We can write $X(s) = \sqrt{\varepsilon_{x\mathrm{rms}}}\,w(s) = w_{\max}(s)$ to obtain an equation for the maximum amplitude function $w_{\max}(s)$ from equation (3.3.6). We also assume uniform focusing, and do the substitution $k_0^2 \to k^2$ to include space charge defocusing. Therefore, using the *effective beam radius* $R \equiv 2X$ and *effective emittance* $\tilde{\varepsilon}_x$, equation (4.3.1) can be cast in the alternative form

$$R''(s) + k^2 R(s) - \frac{\tilde{\varepsilon}_x^2}{R^3(s)} = 0, \tag{4.3.2}$$

which is the basis for the *beam envelope* calculations discussed in section 6.1. Note that the equations for either $X(s)$ or $R(s)$, unlike the ones for $w(s)$ or $w_{\max}$(s), involve the *statistical* quantity $\varepsilon_{x\mathrm{rms}}$ characterizing a beam distribution.

As mentioned above, 'k' includes both (linear) external focusing and space charge defocusing. Explicitly,

$$k^2 = k_0^2 - \frac{K}{R^2(s)} \to k_0^2 - \frac{K}{a^2}, \tag{4.3.3}$$

where K is the generalized beam perveance or 'space-charge parameter' defined in equation (4.2.4), and k_0 is the focusing constant. In the smooth approximation $R''(s) = 0$ in equation (4.3.2), and we have $R = a = \sqrt{\tilde{\varepsilon}_x/k}$ for the 'average' beam radius of the *rms-envelope matched* beam. The connection between the parameters of a periodic focusing lattice and those of the smooth approximation is made, as in equation (3.4.3), through $k = \sigma/S$, and $k_0 = \sigma_0/S$, where σ, σ_0 are the phase advances per period S, *with and without space charge*, respectively. Note that we have now a new phase advance that includes the effect of linear space charge but that we are *not* explicitly using a betatron function that includes space charge.

In figure 4.2 we present an example of calculations of beam envelope and single particle trajectories in a periodic solenoid lattice and in the equivalent uniform-focusing lattice. The beam perveance chosen is $K = 0.0015$ (equation (4.2.4)), while the effective emittances are $\tilde{\varepsilon}_x = \tilde{\varepsilon}_y = 60\ \mu\mathrm{m}$.

The lattice period is $S = 0.32$ m; the solenoid effective length is 0.065 m, and the peak focusing constant is $k_0^2 = 100\ \mathrm{m}^{-2}$. We solve the K–V envelope equation (4.3.2) with a lattice of hard-edge solenoids and also with uniform-focusing with an average focusing constant $k_{\mathrm{ave}}^2 = 20.31\ \mathrm{m}^{-2}$. By construction, the smooth-focusing model does not yield exactly the same phase advance and tune depression (see equation (4.3.4) below) as the piecewise focusing model (see figure 4.2). Details can be found in a Mathcad program briefly described at the end of the chapter.

From equations (4.3.2) and (4.3.3), a number of dimensionless *space charge (SC) intensity parameters* can be defined. The first one is called the *tune depression* η:

$$\eta = \frac{k}{k_0} = \frac{\sigma}{\sigma_0}, \tag{4.3.4}$$

applicable to periodic linear or circular machines, although the word 'tune' is directly relevant to circular machines only. The tune depression, however, is equal to 1

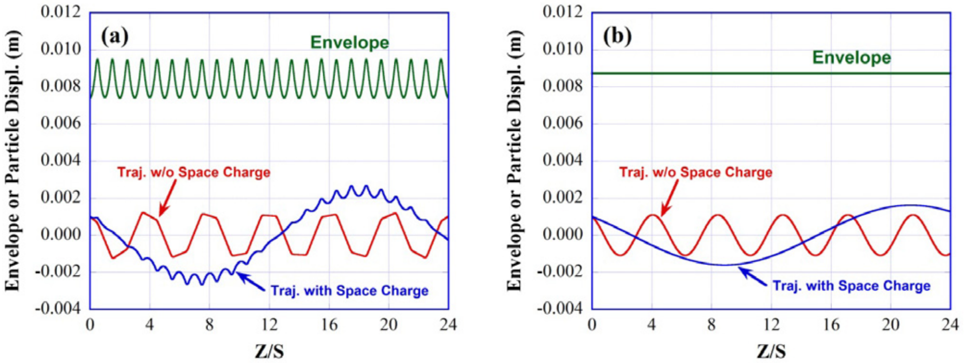

Figure 4.2. (a) Matched beam envelope and single particle trajectories in a *periodic* solenoid lattice. (b) Matched beam envelope and single particle trajectories in the equivalent uniform-focusing lattice. The tune depressions (equation (4.3.4)) are (a) 0.193, and (b) 0.175.

for ‘zero’ current ($K = 0$ in equation (4.3.3)) and to 0 for ‘zero’ emittance. In the latter case we approach *the space charge limit* $k \rightarrow 0$, whereby external focusing exactly balances direct space charge (equation (4.3.3)), and which implies $\lambda = 2\pi/k \rightarrow \infty$, i.e. perfectly laminar flow. Therefore, it is perhaps better to change the definition of an SC intensity parameter to

$$\chi = 1 - \eta^2 = \frac{K}{k_0^2 a^2}, \tag{4.3.5}$$

as has been done by Reiser and independently by Davidson (see [1, 6]), so the range of χ is from zero, in the limit of zero current, to 1 in the space charge limit. Note that χ is, from equations (4.3.2) and (4.3.3), equal to the ratio of space charge force K/a to external focusing force $k_0 a$ at the effective beam edge $R = a$. Another SC intensity parameter, related to χ and also used by Reiser, and Davidson and Qin, can be used to express more transparently the role of external focusing and the beam quantities:

$$u = \frac{K}{2k_0\tilde{\varepsilon}_x}. \tag{4.3.6}$$

In contrast to χ, u ranges from zero at zero current, to infinity at zero emittance. It is straightforward to show the connection between u and χ:

$$\chi = \frac{2}{1 + \sqrt{1 + u^{-2}}}. \tag{4.3.7}$$

To complement the equations above, it is interesting to note that the ratio of effective beam radii in the limits of zero emittance (a_B) and zero current (a_0) is given by

$$\frac{a_\mathrm{B}}{a_0} = \frac{\sqrt{K/k_0^2}}{\sqrt{\tilde{\varepsilon}_x/k_0}} = (2u)^{1/2}, \tag{4.3.8}$$

as can be easily shown from the envelope equation (4.3.2). For any combination of space charge and emittance, however, the effective ‘average’ beam radius a is better approximated by just adding a_B and a_0 in quadrature:

$$a \cong \sqrt{a_{\mathrm{B}}^2 + a_0^2} = a_0\sqrt{1 + 2u}, \tag{4.3.9}$$

with the provision that $u \leqslant 5$ ($\chi = 0.99$ for $u = 5$), approximately. The expression in equation (4.3.9) overestimates the beam radius a by a few percent relative to exact envelope calculations (see section 6.1). The *exact* smooth-approximation results for a in terms of χ or u, are:

$$\begin{aligned} a &= a_0(1 - \chi)^{-1/4}, \quad 0 < \chi < 1, \\ a &= a_0\sqrt{u + \sqrt{1 + u^2}}, \quad 0 < u, \end{aligned} \tag{4.3.10}$$

as can be easily derived from $a = \sqrt{\tilde{\varepsilon}_x/k}$, $a_0 = \sqrt{\tilde{\varepsilon}_x/k_0}$, and the definitions of χ and u in equations (4.3.5) and (4.3.6). In general, equations (4.3.10) underestimate a relative to exact envelope calculations.

We emphasize that the SC intensity parameters u, and χ are applicable only to *rms-envelope matched* beams in *periodic* lattices. Both parameters are needed to understand the role of space charge and how to reduce its effect: for constant current and emittance, we need stronger focusing to make the beam smaller (equation (4.3.6)), which increases the space charge force but also reduces the ratio of space charge force to external focusing force (equation (4.3.5)); see also [16]. In the ideal space charge limit, this latter ratio is maximum and equal to $\chi = 1$ (or $\eta = 0$), but we consider $\chi > 0.5$ (or $\eta < 0.71$) to be the regime of *space-charge dominated* beam transport because in this regime *plasma oscillations* dominate over zero-current betatron motion ([1], chapter 7). The term 'space-charge dominated *beam*' abounds in the literature, but it is more proper to speak of 'space-charge dominated *beam transport*' as a beam with given current and emittance can be either emittance or space-charge dominated depending on external focusing.

4.4 Incoherent space-charge (SC) betatron tune shift

The tune, i.e. the number of betatron oscillations in one revolution in a circular lattice, will change under the action of direct space charge and also from image forces that act when the beam is off center in the vacuum pipe. The first effect defines the *incoherent tune shift*, which can be easily calculated using the K–V envelope equation. If ν_{0x} is the bare tune (horizontal plane), defined in equation (3.4.4), and ν_x the *shifted tune* from direct space charge, we can write

$$\nu_{0x} - \nu_x = \nu_{0x}\left(1 - \sqrt{1 - \chi}\right), \tag{4.4.1}$$

from equations (4.3.4), (4.3.5), and $\nu/\nu_0 = \sigma/\sigma_0$. Further, if we assume *weak* space charge, i.e. small χ, we have $a \cong a_0 = \sqrt{\tilde{\varepsilon}_x/k_0}$, and with $k_0 = \nu_0/R_{\mathrm{m}}$ (see equation (3.4.4)) we can write

$$\nu_{0x} - \nu_x \cong \frac{\nu_{0x}\chi}{2} = \frac{KR_{\mathrm{m}}}{2\tilde{\varepsilon}_x}. \tag{4.4.2}$$

R_m above is the *machine radius*, not to be confused with the beam radius in the K–V envelope equation. Two more commonly quoted equations for the incoherent SC tune shift $\Delta\nu_x \equiv \nu_{0x} - \nu_x$ for *weak* space charge are

$$\Delta\nu_x \cong \frac{IR_\mathrm{m}}{I_0\beta^3\gamma^3\tilde{\varepsilon}_x} = \frac{Nr_\mathrm{e}}{2\pi\beta^2\gamma^3\tilde{\varepsilon}_x}, \quad \text{(K–V Distribution)}, \tag{4.4.3}$$

where we have used the expression for the beam perveance K in equation (4.2.4). For the second equality we employ the definition of the classical electron radius $r_\mathrm{e} = ec/I_0$, $I_0 = 4\pi\varepsilon_0 mc^3/\mathrm{e}$, and $I = Ne\beta c/2\pi R_\mathrm{m}$ in terms of the total number of particles N of a continuous beam. Other authors use $N/2\pi R_\mathrm{m}$ for the *number of particles per unit length*. Note that for a given energy and small direct space charge the incoherent tune shift is proportional to the beam-current/emittance ratio, and is independent of the bare tune ν_{0x}. The scaling of $\Delta\nu_x$ as $1/\gamma^3$ is, however, the most dramatic, explaining why direct SC effects are negligible in electron machines such as light sources, and not significant in most proton synchrotrons above some 10 GeV [8].

In general, the incoherent tune shift will depend on ν_{0x}, becoming comparable to it for very strong space charge. Therefore, another sensible measure of SC strength is the ratio of tune shift to bare tune:

$$\frac{\Delta\nu_x}{\nu_{0x}} = 1 - \sqrt{1-\chi} \cong \frac{\chi}{2}, \tag{4.4.4}$$

from equations (4.4.1) and (4.4.2). Note that the incoherent tune shift alone would not be a good measure of incoherent SC effects for overall beam transport; by contrast, the relative change in tune can be related to χ or u. For example, an incoherent betatron tune shift of 0.4 at an operating horizontal tune of 6.7, as in the Fermilab booster, yields a relative tune shift of about 6%. While significant for resonance crossing (see chapter 6), it does not correspond to very strong transverse SC effects, i.e. beam transport is still dominated by emittance.

Another—more common—approach used to derive the incoherent SC tune shift starts with the Courant–Snyder matrix treatment of a circular lattice and considers the SC effect as a distributed defocusing 'error'. The following tune-shift formula is obtained in a *linear approximation* in the strength of the defocusing error Δk_0^2 (see [3] or [9] for details):

$$\Delta\nu_x = -\frac{1}{4\pi}\oint \beta_x(s)\Delta k_0^2(s)\,\mathrm{d}s, \tag{4.4.5}$$

where the zero-current beta function is evaluated at the location of the error. From equation (4.3.3) we have $\Delta k_0^2(s) = -K/R^2(s)$ (note the sign); we can also define

$$\left\langle \frac{\beta_x(s)}{R^2(s)} \right\rangle = \frac{1}{2\pi R_\mathrm{m}}\int_0^{2\pi R_\mathrm{m}} \frac{\beta_x(s)}{R^2(s)}\,\mathrm{d}s. \tag{4.4.6}$$

Now, we can identify the average on the right as just $1/\tilde{\varepsilon}_{x\mathrm{rms}}$with $\beta_x(s)$ the *zero-current* beta function, and $\langle R^2(s)\rangle \cong a_0^2$. Therefore, we recover the result in equation (4.4.2) for the incoherent tune shift (for weak SC and a uniform particle distribution) by combining equations (4.4.5) and (4.4.6).

If the particle distribution is *Gaussian* as in equation (4.1.4), we can consider its projection in configuration space by integrating over p_x, and p_y (after defining also $f\,(y,\,p_y)$ for the vertical plane). Then we obtain a charge density of the form

$$n_q(r) = \frac{I}{2\pi\beta c\sigma^2}\exp\left(-r^2/2\sigma^2\right), \tag{4.4.7}$$

with $r = \sqrt{x^2 + y^2}$. The defocusing caused by such distribution is *non-linear*, but linearizing the SC force for small r, i.e. assuming $r \ll \sigma$, leads to a *small-amplitude tune spread* [8, 10] equal to *twice* the size of the tune shift for a uniform distribution having the same current and rms emittance:

$$\Delta\nu_x \cong \frac{2IR_\mathrm{m}}{I_0\beta^3\gamma^3\varepsilon_\mathrm{rms}} = \frac{2Nr_\mathrm{e}}{2\pi\beta^2\gamma^3(4\varepsilon_\mathrm{rms})}, \quad \text{(Gaussian Distribution)}. \tag{4.4.8}$$

Note that we now have a *tune spread* instead of a tune shift because particles moving at different amplitudes have different tunes.

So far we have assumed that the beam has a circular cross section, but in actual AG focusing the bare tunes in the two transverse directions may have different values, and the beam may have correspondingly different average horizontal and vertical dimensions. Therefore, if the beam has a uniform density but average dimensions a and b in the horizontal and vertical directions, respectively, the horizontal incoherent SC tune shift will depend on parameters for both the horizontal and vertical planes. The *small amplitude* incoherent tune shift in the vertical direction can be derived along the lines of equations (4.4.5) and (4.4.6) (see [8] or [11]):

$$\Delta\nu_y \cong \frac{Nr_\mathrm{e}}{\pi\beta^2\gamma^3\tilde{\varepsilon}_y}\left(1 + \sqrt{\bar{\beta}_x\tilde{\varepsilon}_x/\bar{\beta}_y\tilde{\varepsilon}_y}\right)^{-1}. \tag{4.4.9}$$

The result for $\Delta\nu_x$ (horizontal direction) is obtained by exchanging the x and y subscripts above.

We can calculate incoherent SC tune shifts for elliptical beams and *arbitrary* SC from the K–V envelope equations. In equations (4.3.2), (4.3.3) we presented the K–V envelope equation for an axisymmetric beam in a uniform solenoidal focusing channel. We generalize the equation to piecewise AG focusing (section 3.2) and write

$$\begin{aligned} X''(s) + k_{0x}^2(s)X(s) - \frac{2K}{[X(s) + Y(s)]} - \frac{\tilde{\varepsilon}_x^2}{X^3(s)} &= 0, \\ Y''(s) + k_{0y}^2(s)Y(s) - \frac{2K}{[X(s) + Y(s)]} - \frac{\tilde{\varepsilon}_y^2}{Y^3(s)} &= 0, \end{aligned} \tag{4.4.10}$$

where we have allowed for the possibility of different focusing functions as well as different effective emittances in the two transverse Cartesian planes. (The equations are often called 'K–V equations' although the K–V distribution is not a self-consistent distribution in an AG focusing lattice). The corresponding smooth-approximation, *coupled* algebraic equations are

$$k_{0x}^2 a - \frac{2K}{a+b} - \frac{\tilde{\varepsilon}_x^2}{a^3} = 0,$$
$$k_{0y}^2 b - \frac{2K}{a+b} - \frac{\tilde{\varepsilon}_y^2}{b^3} = 0, \tag{4.4.11}$$

with the understanding that all quantities are constants. Thus, following a procedure similar to the one used for beams with circular cross section, we define *tune depressions* $\eta_{x,y}$ in the two transverse planes by the equations

$$\eta_x \equiv \frac{k_x}{k_{0x}} = \frac{\nu_x}{\nu_{0x}}; \qquad \eta_y \equiv \frac{k_y}{k_{0y}} = \frac{\nu_y}{\nu_{0y}}, \tag{4.4.12}$$

and write for the tune shifts,

$$\nu_{0x} - \nu_x = \nu_{0x}\left(1 - \sqrt{1 - \chi_x}\right),$$
$$\nu_{0y} - \nu_y = \nu_{0y}\left(1 - \sqrt{1 - \chi_y}\right), \tag{4.4.13}$$

(see equation (4.4.1)) where the intensity parameters $\chi_{x,y}$are given by:

$$\chi_x = \frac{2K}{k_{0x}^2(a+b)a}, \qquad \chi_y = \frac{2K}{k_{0y}^2(a+b)b}. \tag{4.4.14}$$

For weak SC, we have from equation (4.4.13) and the first equality in the last equation,

$$\Delta\nu_x \cong \frac{\nu_{0x}\chi_x}{2} = \frac{KR_{\mathrm{m}}^2}{\nu_{0x}[1 + (b/a)]a^2}, \tag{4.4.15}$$

which is similar to equation (4.4.2). Further, from $b/a \cong b_0/a_0 = \sqrt{\tilde{\varepsilon}_y \bar{\beta}_x / \tilde{\varepsilon}_x \bar{\beta}_y}$, we find

$$\Delta\nu_x \cong \frac{KR_{\mathrm{m}}}{\tilde{\varepsilon}_x}\left(1 + \sqrt{\bar{\beta}_y \tilde{\varepsilon}_y / \bar{\beta}_x \tilde{\varepsilon}_x}\right)^{-1}, \tag{4.4.16}$$

in agreement with the x version of equation (4.4.9). Note that for arbitrary SC, equations (4.4.11) must be numerically solved first for a and b, then the intensity parameters are calculated from equation (4.4.14), and finally the incoherent tune shifts result from equation (4.4.13). Alternatively, we can solve the K–V envelope equations (4.4.10) for the piecewise focusing functions and then obtain the phase advances (per period) with and without space charge. One of the numerical examples described at the end of the chapter deals with incoherent SC tune shift calculations employing both the algebraic (smooth approximation) and envelope approaches. See also [12].

4.5 Coherent tune shift and Laslett coefficients

Beams require a good vacuum to be transported over long distances without losses or deleterious effects. In addition, bending magnets that use ferromagnetic materials are common in circular machines. Thus, the betatron tune can be affected significantly because particles that are off axis in the pipe are subject to *image forces*. These forces depend not only on the particle's energy but also on the geometry and magnetic properties of the boundaries. The problem of finding these forces for different beam and pipe geometries was solved by L J Laslett in the 1960s. For a round beam, for example, the formula for the *incoherent* SC tune shift, equation (4.4.3), must be supplemented with two terms involving the pipe height h, the half-gap g of bending magnets and the Laslett coefficients ε_1 and ε_2 for *incoherent* tune shift:

$$\Delta\nu_{x,\mathrm{inc}} \equiv \nu_{0x} - \nu_{x,\mathrm{inc}} \cong \frac{Nr_\mathrm{e}}{\pi\beta^2\gamma\tilde{\varepsilon}_x}\left[\varepsilon_1\left(\frac{1}{\gamma^2} + \frac{a_0^2}{h^2}\right) + \varepsilon_2\beta^2\frac{a_0^2}{g^2}\right], \tag{4.5.1}$$

where $\varepsilon_1 = 1/2 = \varepsilon_2$ for a circular pipe. Note that we recover equation (4.4.3) if a_0^2/h^2, $a_0^2/g^2 \ll 1$ (a_0 is the zero-current beam radius). Note also that equation (4.5.1) is valid for *weak* space charge, i.e. for tune shifts that are small when compared to the operating (bare) tune; this is the case for almost all accelerators in existence. When beam transport is dominated by transverse SC effects, on the other hand, equation (4.4.1) must be used to calculate the incoherent tune shift; we give examples in chapter 6.

The effect on the beam centroid, i.e. on the coherent motion leads to a *coherent* SC tune shift given, for *penetrating fields*, by the so-called 'integer formula' (see [8], [13], or [14]):

$$\Delta\nu_{x,\mathrm{coh}} \equiv \nu_{0x} - \nu_{x,\mathrm{coh}} \cong \frac{Nr_\mathrm{e}}{\pi\beta^2\gamma\tilde{\varepsilon}_x}\left[\xi_1\frac{a_0^2}{h^2} + \xi_2\beta^2\frac{a_0^2}{g^2}\right], \quad \text{for penetrating fields}, \tag{4.5.2}$$

where ζ_1 and ζ_2 are Laslett coefficients for *coherent* tune shift. For a round pipe, $\zeta_1 = 1/2$, $\zeta_2 = \pi^2/16 = 0.617$. For *non-penetrating fields*, the 'half-integer formula' applies:

$$\Delta\nu_{x,\mathrm{coh}} \cong \frac{Nr_\mathrm{e}}{\pi\beta^2\gamma\tilde{\varepsilon}_x}\left[\xi_1\frac{1}{\gamma^2}\frac{a_0^2}{h^2} + \beta^2\left(\varepsilon_1\frac{a_0^2}{h^2} + \varepsilon_2\frac{a_0^2}{g^2}\right)\right], \quad \text{for non-penetrating fields} \tag{4.5.3}$$

Note that the effect of images is always to defocus the beam, thus reducing the tune. For comparison, we quote the results presented by Reiser [1] for the effect of image forces in a cylindrical pipe in terms of phase advances and the beam perveance K:

$$\sigma_\mathrm{eff} = \begin{cases} \sigma_0\left(1 - \dfrac{K\gamma^2}{h^2\sigma_0^2}S^2\right)^{1/2}, & \text{penetrating fields,} \\[2ex] \sigma_0\left(1 - \dfrac{K}{h^2\sigma_0^2}S^2\right)^{1/2}, & \text{non-penetrating field.} \end{cases} \tag{4.5.4}$$

In these equations, σ_{eff} is the resulting effective phase advance per lattice period S, $\sigma_0 = k_0 S$ is the zero-current phase advance, and $k_0 = \tilde{\varepsilon}_x / a_0^2$. Recalling that tune and phase advance are connected through $\nu = (R_{\text{m}}/S)\sigma$, we can rewrite the second equation (4.5.4) in the form:

$$\nu_{\text{eff}} - \nu_0 \cong -\frac{K}{2\nu_0}\left(\frac{R_{\text{m}}}{h}\right)^2, \quad \text{or} \quad -\frac{KR_{\text{m}}}{2\tilde{\varepsilon}_x}\left(\frac{a_0}{h}\right)^2, \tag{4.5.5}$$

which agrees with equation (4.5.3) and is *always* a good approximation for small beams and small off-center displacements relative to the pipe radius. The result has been verified experimentally by Sutter *et al* [15]. Further, by comparing equation (4.5.5) with equation (4.4.2) we can see that the coherent tune shift is always much smaller than the incoherent tune shift.

From the results for incoherent and coherent SC tune shifts above we see that at high energies the tune shift is dominated by image effects ($1/\gamma^2 \to 0$ in equation (4.5.1)), but at low energies, or with complete neutralization of SC at high energies (see [13]), the direct SC dominates.

All the results discussed so far apply to coasting, i.e. unbunched, beams. See [8], for example, for a treatment of tune shifts in bunched beams; [8] also incorporates all cases in a single ‘practical’ formula and presents interesting examples of ways to overcome the ‘space-charge limit’ by increasing the injection energy into circular machines. The ‘space-charge limit’ is often called the ‘Laslett tune shift limit (or) criterion’ and put at $\Delta\nu \leqslant 0.5$. As mentioned before, this criterion is related to resonance crossing and not to reducing the SC intensity parameter χ. Direct SC and image forces, naturally, are parts of the physics of *instabilities*, a host of phenomena of increasing importance for accelerators. Instabilities put additional limits to the operation of accelerators, but discussing them is beyond the scope of this book.

Computer resources

The trace-space plots in figure 4.1 are generated with the Mathcad programs ***PhSp-Dist-Emitt4.xmcd*** and ***PhSp-Dist-Emitt-II3.xmcd***. The first program solves the equations of motion for a number of particles (typically 100 or less) in a linear uniform-focusing system 5 m in length and allows plotting the trace space at a number of locations. In addition, the program is used to calculate effective emittances at the same locations. The second program includes terms of third order (spherical aberration) to display the complex evolution of trace space. For both programs, all particles start with $x(0) = 0$, and with initial slopes following either uniform (rand := 0) or random (rand := 1) distributions. Note that the programs are started so that the same *seed* is used every time for the generation of the random slopes; this assures reproducibility. One interesting issue to explore is numerical convergence: for the random distribution of initial slopes, the effective emittance far from the source increases as the number of particles increases (why?).

Another Mathcad program, ***EnvEqn-SmApprox.xmcd***, is used to solve the K–V envelope equation in a periodic solenoid system with an arbitrary number of hard-edge solenoids. The program also includes uniform-focusing approximation calculations with and without space charge, as shown in figure 4.2(b). The envelope for the matched beam in the periodic solenoid system (figure 4.1(a)) relies on output from the Matlab program **Menv** used for matching calculations (see appendix).

References

[1] Reiser M 2008 *Theory and Design of Charged Particle Beams* 2nd edn (New York: Wiley)

[2] Wangler T P 2008 *RF Linear Accelerators* 2nd edn (Weinheim: Wiley)

[3] Edwards D A and Syphers M J 2004 *An Introduction to the Physics of High Energy Accelerators* (New York: Wiley)

[4] Barletta, Spentzouris and Harms 2012 US Particle Accelerator School Notes http://uspas.fnal.gov/materials/12MSU/emitlect.pdf

[5] Rhee M J 1986 Invariance properties of the root-mean-square emittance in a linear system *Phys. Fluids* **29** 3495

[6] Davidson R C and Qin H 2001 *Physics of Intense Particle Beams in High Energy Accelerators* (London: Imperial College Press)

[7] Bernal S 2015 Conceptual difficulties of a thermodynamics description of charged-particle beams *Proc. IPAC2015* (*Richmond, VA, 3–8 May 2015*) p 649

[8] Schindl K 2006 Space charge *CERN 2006-002*

[9] Rossbach J and Schümuser P 1994 Basic course on accelerator optics *CAS CERN* 94-01 p 76

[10] Cornacchia M 2012 Incoherent space charge tune shifts *UMER Technical Note* (unpublished) See book's website

[11] Hofmann A 1994 Tune shifts from self-fields and images *CAS CERN 94-01*

[12] Bernal S *et al* 2006 RMS envelope matching of electron beams from 'zero' current to extreme space charge in a fixed lattice of short magnets *Phys. Rev. ST Accel. Beams* **9** 064202

[13] Keil E 1972 Intersecting storage rings *CERN 72-14*

[14] Bryant P J 1987 Betatron frequency shifts due to self and image fields *CAS CERN 1987-010.62* pp 62–78

[15] Sutter D F, Cornacchia M, Bernal S, Beaudoin B, Kishek R A, Koeth T and O'Shea P G 2011 Current dependent tune shifts in the University of Maryland Electron Ring UMER *Proc. 2011 Particle Accelerator Conf.* (New York) p 1668

[16] Wangler T P 2008 Resolve the apparent paradox that the most effective approach for controlling space-charge effects is to apply strong focusing, which makes the beam size small and increases the space-charge-force *Unpublished Technical Note, University of Maryland, College Park, 2008*. See book's website

Chapter 5

Longitudinal beam dynamics and radiation

The charged particle beams treated in chapter 4 were continuous, i.e. ‘unbunched’, very often referred also as ‘coasting’ beams. This is a good approximation whenever the longitudinal extent of the beam is long compared with its transverse dimensions. However, in most accelerators and related devices the beam bunches have longitudinal dimensions comparable to their transverse sizes. This is the case, for example, in linear accelerators (linacs) where radio-frequency (RF) fields not only accelerate the beam but also impart a longitudinal density structure to it. We give a very brief introduction to RF linacs in section 5.1. In section 5.2, we describe *synchrotron oscillations*, the longitudinal counterpart of transverse betatron oscillations, and beam bunch stability. In section 5.3, we present the main ideas and basic equations related to *synchrotron radiation* (SR). Although the topic of ‘light sources’ would fill volumes, we focus in section 5.4 on just their main components, insertion devices, and also describe the essence of free-electron lasers (FELs). Finally, in section 5.5 we introduce a number of definitions of *longitudinal beam emittance*, continue our discussion of small synchrotron oscillations and delineate the basic model of longitudinal space charge: parabolic line-charge density profile and the Neuffer distribution, longitudinal beam perveance, bunch envelope equations, and the longitudinal SC intensity parameter. The computer resources of this chapter deal with synchrotron radiation, beam bunch stability calculations, longitudinal SC, and FELs.

5.1 Radio-frequency (RF) linacs [1]

The energy of particle accelerators based on dc accelerating voltages is limited to a few tens of MeV; an example is the Van de Graaf accelerator. By contrast, RF linear accelerators, or linacs, are based on the repeated application of electric fields to achieve voltage gains that greatly exceed the maximum applied voltage. Electromagnetic

doi:10.1088/978-1-6817-4076-8ch5

waves in vacuum, however, cannot be tapped to accelerate particles because the electric fields are perpendicular to the wave propagation and are also continually changing polarity. To solve both problems, special metallic structures called *resonant cavities* are used to produce longitudinal electric fields that not only have the right polarity but also keep up with the motion of the accelerated particles.

Linacs require many RF cavities to achieve high energies because the field strengths per cavity are limited to a few MV m^{-1}. This fact explains why linacs designed for the highest energies are very long machines. In a typical electron linac, the electrons from a dc thermionic source or a photocathode gun are injected into the RF accelerating structure. The first few RF cavities capture the low-velocity electrons and accelerate them to velocities close to the speed of light; at the same time, the electrons tend to be grouped in *bunches*. The geometry of the main accelerating cavities that follow is designed for acceleration of relativistic electrons. In the *traveling-wave* linac, for example, the electrons ride a traveling EM wave (whose *phase velocity* is essentially equal to c) as a surfer rides a sea wave. The cavity structure is periodic and is equivalent to a series of coupled oscillators that can sustain special field patterns called *modes* if the frequency of the RF is above a *cutoff frequency* that depends on the cell geometry. In the *stationary-wave* type of linac, the wavelength of a longitudinal E-field mode is equal to an integer multiple of the iris separation; this is shown in figure 5.1 for the $2\pi/3$ mode. The wavelength in this case is equal to three times the iris separation. In the traveling-wave linac, on the other hand, the *phase advance per cell* of the RF wave is specified (e.g. $2\pi/3$ for the linac at Stanford Linear Accelerator Center (SLAC); see chapter 6).

Ideally, all the RF power applied to a cavity would be transmitted to the beam, but this is not possible as significant losses occur at the cavity walls. The *power loss* per unit length, P_w, is related to the *peak accelerating field* E_p through a quantity called the *shunt impedance* per unit length, r_s:

$$P_w = \frac{E_\mathrm{p}^2}{r_s}. \tag{5.1.1}$$

Since the shunt impedance increases with frequency for normal-conducting cavities, higher operating RF frequencies are desired. But other important

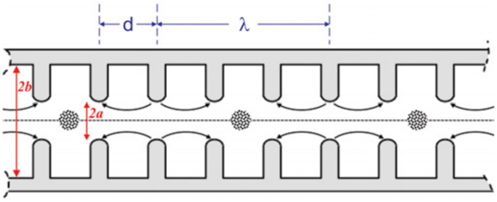

Figure 5.1. Cross section of RF cavities showing field variation of the $2\pi/3$ mode. See also section 6.3. Adapted from [1].

considerations that depend on the type of particle bunch desired may favor lower frequencies. Thus, the main design parameter in a linac is the frequency and is normally chosen as a compromise between power budget considerations and desired beam characteristics.

If W is the *stored energy* per unit length of cavity, the *transmitted energy flux* P_t (in Joule s^{-1}), is given by $P_t = v_g W$, where v_g is the *group velocity* of the RF wave. Furthermore, P_t decays along the axial direction with constant 2α (units of m^{-1}), i.e. $P_t \propto \exp(-2\alpha s)$, where

$$\alpha = \frac{\omega_{\mathrm{RF}}}{2v_g Q}. \tag{5.1.2}$$

In this equation ω_{RF} is the RF angular frequency, and Q defines the cavity's *quality factor*. In equilibrium W is constant, so the transmitted energy flux and power loss per unit length are connected through the equation

$$P_t = \frac{P_w}{2\alpha}. \tag{5.1.3}$$

Therefore, from equation (5.1.1) we get

$$E_{\mathrm{p}}^2 = 2\alpha r_s P_t. \tag{5.1.4}$$

The peak accelerating voltage E_{p} decays with a constant α if the shunt impedance r_s is the same throughout the accelerating structure. The *attenuation parameter* of the *constant impedance structure* is then equal to

$$\tau = \alpha L = \frac{\omega_{\mathrm{RF}} L}{2v_g Q}. \tag{5.1.5}$$

Finally, after integration over a structure of length L, we get the *maximum energy gain per section* (see e.g. [2] for details):

$$\Delta K_{\mathrm{CI}} = e\sqrt{P_{t0} L r_s}\sqrt{2\tau^{-1}}[1 - \exp(-\tau)], \tag{5.1.6}$$

where P_{t0} is the peak RF power. The subscript CI stands for constant impedance.

The shunt impedance r_s is constant if all the cells in the accelerating structure have the same geometry and dimensions. Furthermore, r_s is weakly dependent on the size of the iris in the cavity cell (see figure 5.1), but the group velocity v_g and thus the transmitted energy flux P_t are very sensitive to the iris dimensions. Therefore, by making the iris diameter progressively smaller for downstream cavity cells it is possible to achieve a constant accelerating peak field E_{p}. The structure so constructed is called a *constant gradient structure*. In this case, the transmitted energy flux decreases linearly with axial distance, i.e. $\partial P_t/\partial s = \text{const.} < 0$, so the group velocity also decreases gradually. With $\tau = \alpha L$, we have (see e.g. [2]):

$$v_{g\mathrm{CG}}(s) = \frac{\omega_{\mathrm{RF}}}{Q}\frac{L - [1 - \exp(-2\tau)]s}{1 - \exp(-2\tau)}, \tag{5.1.7}$$

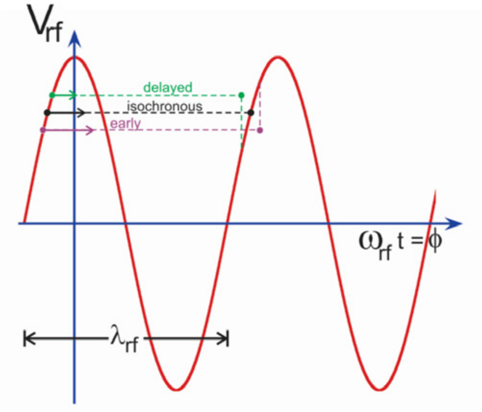

Figure 5.2. Principle of phase stability in a linac. From [1].

and a *maximum energy gain per section* equal to

$$\Delta K_{\rm CG} = e\sqrt{P_{t0}Lr_s}\sqrt{1-\exp(-2\tau)}\,, \tag{5.1.8}$$

where the subscript CG stands for constant gradient. Other factors that affect the operation of linacs are *beam loading*, i.e. the effect of the beam on the cavity fields, and the presence of wakefields especially for ultra-relativistic short bunches. Wakefields are scattered radiation that results from the interaction of the bunch fields with structures in the beamline. Wakefields can interact back with parts of the bunch and lead to deleterious effects and instabilities. Chapters 10 and 11 of [3] discuss these topics in detail.

5.2 Beam bunch stability and RF bucket

A crucial issue for linac operation is the beam bunch *stability*. Typically, the electron bunch is injected slightly ahead of the peak RF field. Therefore, and as shown in figure 5.2, the particles see a quasi-linear restoring force if the bunch length is small compared to the RF wavelength: the particles that arrive early at the accelerating cavity are given a smaller RF kick than those that arrive late, but those that arrive with just the right phase ϕ_S, the so-called *isochronous* particles, are given the same kick every time. Therefore, particles inside the bunch undergo longitudinal oscillations not unlike a pendulum; these oscillations are called *synchrotron oscillations*. The analogy with the pendulum can be carried out further if we picture a biased pendulum, i.e. a pendulum whose equilibrium position is off from the vertical by an angle ϕ_S (see [4]). The pendulum will be stable for oscillation angles that do not depart too much from ϕ_S. In fact, the phase space of the biased pendulum which is formed by the coordinates $(\dot{\phi}, \phi)$ is mathematically equivalent to the *longitudinal phase space* $(\delta U, \phi)$ of the bunch particles, where δU is the energy

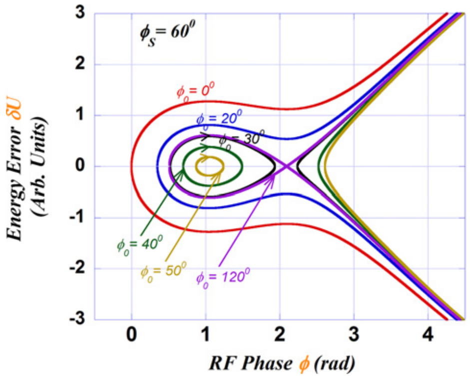

Figure 5.3. Longitudinal phase space (δU, ϕ) and RF bucket (see equation (5.2.1) and text). Particles inside closed curves are stable. From [1].

error, i.e. the energy deviation from the energy of the synchronous particles. For the pendulum we have (see [4], section 7.5),

$$\dot{\phi}^2 + \Omega_S^2\left(\frac{2}{\cos\phi_S}\left(\cos\phi_0 - \cos\phi\right) + 2\left(\phi_0 - \phi\right)\tan\phi_S - \dot{\phi}_0^2\right) = 0, \tag{5.2.1}$$

where Ω_S is the angular frequency of *small* ‘synchrotron’ oscillations, and ϕ_0 is the *initial* phase angle. In figure 5.3 we have plotted equation (5.2.1) for $\dot{\phi}_0 = 0$, $\Omega_S = 1\ \mathrm{s}^{-1}$, $\phi_S = 60°$ and six values of ϕ_0. (Naturally, the assumed synchrotron frequency is chosen only for illustration purposes; $\Omega_S/2\pi$ in a real accelerator can be of the order of KHz). The values of the initial phase (0°, 20°, 30°, 40°, 50°, and 120°) correspond to six values of the particle’s energy; the closer the initial phase is to $\phi_S = 60°$, the closer the oscillations are to pure harmonic oscillations. If the energy (initial phase) deviates too much, on the other hand, the particle motion will be unbound, as illustrated by the open curves in figure 5.3. The stability of particles in the bunch then depends on capturing particles with the right velocities inside a region of the longitudinal RF field; the corresponding region in phase space is called the *RF bucket* and is bounded by the *separatrix* curve (the curve labelled $\phi_0 = 120°$ in figure 5.3). The RF bucket contains a stable bunch of particles called a *micropulse*. If the RF is pulsed, then the group of beam bunches per pulse is called a *macropulse*. We will return to synchrotron oscillations in section 5.5.

5.3 Synchrotron radiation [1]

The force that accelerates a charged particle can be resolved into two components, one along and the other one perpendicular to the instantaneous velocity direction. The total power radiated by a charged particle is greater from transverse than from longitudinal acceleration by the relativistic factor γ^2:

$$P_\perp = \gamma^2 P_\parallel. \tag{5.3.1}$$

For highly relativistic particles, $\gamma \gg 1$; electrons with a kinetic energy of 10 MeV, for example, have $\gamma^2 = 423$. Thus, to generate copious EM radiation, it is more efficient to bend the trajectory of an energetic charged particle than to simply push it along a straight line. The radiation generated from transverse acceleration is called *synchrotron radiation* (*SR*).

In the *non-relativistic limit*, i.e. when the speed is a small fraction of the speed of light c, the total instantaneous power (in watts) radiated by an electron (electrical charge $-e$) with acceleration $a(t)$ is given by Larmor's formula:

$$P_{\mathrm{NR}}(t) = \frac{e^2 a^2(t)}{6\pi\varepsilon_0 c^3}. \tag{5.3.2}$$

If relativistic effects are included, Larmor's formula becomes

$$P_{\mathrm{R}}(t) = \frac{e^2 a^2(t)\gamma^4}{6\pi\varepsilon_0 c^3} = P_{\mathrm{NR}}(t)\gamma^4 \tag{5.3.3}$$

If an electron of *total energy E* moves on a circular orbit of radius ρ under the action of a uniform magnetic field B, equation (5.3.3) can be written in other useful forms:

$$P_{\mathrm{R}}(t) = \frac{e^2 c}{6\pi\varepsilon_0}\frac{\beta^4\gamma^4}{\rho^2} = \frac{e^4}{6\pi\varepsilon_0 m_e{}^4 c^5}E^2 B^2. \tag{5.3.4}$$

Equation (5.3.4) displays the scaling of SR power with bending radius ($P \propto 1/\rho^2$), rest mass ($P \propto 1/m^4$), and magnetic field of bending dipole ($P \propto B^2$). Especially noteworthy is the very strong dependence of SR power on the rest mass of the charged particle. The energy lost to SR per turn for electrons of total energy E (in GeV) in a field B (in Tesla) can be found from equation (5.3.4):

$$\frac{\Delta E}{\text{turn}}[\text{keV}] = 88.5 \times \frac{E^4}{\rho} = 26.6 \times E^3 B, \tag{5.3.5}$$

where the bending radius ρ is given in meters. This energy has to be replenished by RF accelerating cavities (see previous section) to keep the electrons circulating with the same radius ρ. From equation (5.3.4), we can see that the right-hand side of the first equality in equation (5.3.5) has to be multiplied by $(m_e/m_p)^4 = 0.88 \times 10^{-13}$ to apply it to protons of the same energy and orbit radius as the electrons. This shows the limitations of electron circular machines for achieving high energies. However, SR is in itself the reason for building electron machines as 'light sources'.

The most common SR light source is the *electron storage ring*. The main lattice components in a storage ring are dipole magnets for bending and steering, quadrupole magnets for focusing, and sextupole magnets for chromaticity corrections. Thus, the storage ring lattice is characterized by the local radius of curvature $\rho(s)$ of the reference orbit, the quadrupole focusing function $\kappa(s)$ (equation (2.3.10)), the horizontal betatron function β_x, and the dispersion function $D_x(s)$. The momentum compaction factor, introduced in chapter 3, the energy loss per turn, and other important storage ring parameters can be expressed in terms of integrals that were introduced by Helm *et al* in 1973. The first three *SR integrals* are given by

$$I_1 = \oint \frac{D_x(s)}{\rho(s)} \mathrm{d}s, \qquad I_2 = \oint \frac{\mathrm{d}s}{\rho^2(s)}, \qquad I_3 = \oint \frac{\mathrm{d}s}{|\rho^3(s)|}, \tag{5.3.6}$$

The momentum compaction factor as written in equation (3.6.5) is then

$$\alpha_c = \frac{I_1}{C_0}, \tag{5.3.7}$$

where C_0 is the length of the reference orbit. The energy loss per turn is,

$$U_0 = \frac{C_\gamma}{2\pi} E^4 I_2, \tag{5.3.8}$$

where

$$C_\gamma \equiv \frac{4\pi r_e}{3(m_e c^2)^3} \cong 8.844 \times 10^{-5} \frac{\mathrm{m}}{\mathrm{GeV}^3}. \tag{5.3.9}$$

The *nominal energy* is E, and r_e is the classical electron radius. Equation (5.3.8) generalizes the result in equation (5.3.4) or (5.3.5). The fourth SR integral is:

$$I_4 = \oint \frac{D_x(s)}{\rho^3(s)} [1 + 2\rho^2(s)\kappa_x(s)] \mathrm{d}s, \tag{5.3.10}$$

which is valid for a lattice made of sector magnets; for rectangular magnets, the factor in square brackets is reduced to $2\rho^2(s)\kappa_x(s)$. The fifth SR integral is

$$I_5 = \oint \frac{H(s)}{|\rho^3\,(s)|} \mathrm{d}s, \qquad H(s) = \beta_x D'^2{}_x + 2\alpha_x D_x D'_x + \gamma_x D_x^2. \tag{5.3.11}$$

The fourth and fifth SR integrals are used in expressions for the *damping constants* α_i ($i = x, y, z$) and stationary (or 'natural') *rms energy spread*, $(\Delta E)_\mathrm{rms}$, and *equilibrium transverse beam emittance*, ε_x, discussed next.

The emission of SR photons has important effects on the beam dynamics in storage rings and other SR sources. The first effect is the *radiation damping of betatron oscillations*. Because SR photons are emitted in a direction that is essentially identical to the direction of motion (i.e. tangential to the orbit) for highly relativistic charged-particles, conservation of momentum of particle + radiation leads to an overall decrease of momentum of the particle. However, because RF replenishes only the momentum lost along the direction of the beam line, the vertical component of momentum is reduced after acceleration. Simple considerations and algebra (see e.g. USPAS notes by Henderson *et al* [5] or Emery [6]) yield the following equation for the vertical component of the trajectory:

$$y'' + y' \frac{1}{E_0} \frac{\mathrm{d}E}{\mathrm{d}s} + \kappa_y y = 0. \tag{5.3.12}$$

The derivation depends on equating the fractional energy and fractional momentum gains: $\mathrm{d}E/E = \mathrm{d}p_{\mathrm{photon}}/p_z$, valid with $\beta_0 = 1$ for highly relativistic particles. Equation (5.3.12) has the form of a damped harmonic oscillator equation; after changing from spatial to time derivatives, we find a *damping time* and *damping constant for vertical oscillations* equal to:

$$\tau_y = \frac{2E}{U_0}T_0, \qquad \alpha_y = \frac{1}{\tau_y}, \tag{5.3.13}$$

where U_0 is given by equation (5.3.8), and T_0 is the revolution period. The damping of betatron oscillations occurs in all three dimensions and goes along with a reduction in corresponding emittances. Thus, without considering other effects, the vertical emittance evolves like $\varepsilon_y = \varepsilon_{y0}\exp(-\alpha_y t)$. The damping times and constants for the components of motion in the *horizontal and longitudinal directions* can be similarly derived (see e.g. [7, 8]):

$$\tau_x = \frac{2E}{J_x U_0}T_0, \qquad \alpha_x = \frac{1}{\tau_x}, \tag{5.3.14}$$

$$\tau_z = \frac{2E}{J_z U_0}T_0, \qquad \alpha_z = \frac{1}{\tau_z}. \tag{5.3.15}$$

Equation (5.3.15) corresponds to the damping parameters of *synchrotron or energy oscillations*. The parameters J_i are called the *damping partition functions* and are equal to:

$$J_x = 1 - \frac{I_4}{I_2}, \qquad J_z = 2 + \frac{I_4}{I_2}, \tag{5.3.16}$$

where I_2 and I_4 are the SR integrals defined before.

The damping of betatron oscillations and emittance cannot go on without limit, as it is accompanied by an 'anti-damping' effect caused by random *quantum excitation*. Since the emission of SR photons also implies a reduction in energy, the particle finds itself moving very rapidly along different closed orbits. This orbit 'noise' leads to emittance increase but, because of the opposite effect from damping, a balance is eventually reached. The *equilibrium ('natural') horizontal emittance* and the *equilibrium ('natural') rms energy spread* are found to be (see e.g. [7, 8]):

$$\varepsilon_x = C_q \gamma^2 \frac{I_5}{I_2 - I_4}, \qquad (\Delta E)_{\mathrm{rms}} = C_q^{1/2}\gamma\left(\frac{I_3}{2I_2 + I_4}\right)^{1/2}. \tag{5.3.17}$$

The 'quantum constant' C_q in equations (5.3.17) is

$$C_q = \frac{55}{32\sqrt{3}}\frac{h}{2\pi m_e c} \cong 3.83 \times 10^{-13}\ \mathrm{m}. \tag{5.3.18}$$

Note that the equilibrium emittance depends on the beam nominal energy through γ^2, the bending radii of the dipoles and the lattice functions (betatron and dispersion). The rms energy spread depends, on the other hand, on the nominal energy and bending radii. In machines where no vertical bending occurs, except possibly from quadrupole misalignment or other errors, the lack of vertical dispersion reduces the antidamping effect of quantum excitation. In these machines, which comprise most electron storage rings, the vertical emittance is much smaller (by a factor of the order of 100) than the horizontal emittance. Machines called 'damping rings' are designed to reduce the emittance of beams injected into linear colliders; a small vertical emittance can lead to luminosities that are higher by orders of magnitude (see e.g. [7, 17].)

5.4 Insertion devices and free-electron lasers (FELs) [1]

The radiation pattern of SR from ultra-relativistic particles forms a narrow beam cone with a vertical opening angle given by γ^{-1}. As an example, for electrons at 511 MeV the angle is 1 milliradian, or 3.4 min of arc. Synchrotron radiation can be obtained from bending by single magnets in circular machines, or by using a combination of magnets of alternating polarities in *insertion devices* called *wigglers* and *undulators*. The bend angles from individual magnets in wigglers are large compared to γ^{-1}. In contrast, bend angles in undulators, are of the same order as γ^{-1}. For bending magnet and wiggler sources the spectrum of SR is *continuous*. Half the power is radiated above and half is radiated below a *critical photon energy* E_{cr}, which for electrons, is given by:

$$E_{\text{cr}} = \frac{3}{4\pi}\frac{hc}{\rho}\gamma^3, \qquad \text{or} \qquad E_{\text{cr}}[\text{keV}] = 0.665 \times B[T] \times E^2[\text{GeV}]. \tag{5.4.1}$$

By contrast, interference effects in undulators yield a discrete spectrum, i.e., a spectrum formed by a series of sharp peaks at certain wavelengths:

$$n\lambda = \frac{\lambda_u}{2\gamma^2}\left(1 + \frac{K^2}{2}\right), \tag{5.4.2}$$

where $n = 1, 2, 3, \ldots$ gives the harmonic number, λ_u is the period of the undulator structure, and $K = \gamma\theta$ is the *undulator parameter*. Since the bend angle in an undulator is $\theta \approx \gamma^{-1}$, we get $K \approx 1$.

The figure of merit in many applications of SR is the *spectral brightness* or *brightness* for short (also called *brilliance* in Europe). Brightness is defined as the number of photons emitted by the SR source per unit time, per unit solid angle, per unit area at the source, and per unit bandwidth around a given frequency:

$$\text{Brightness} = \text{Photons}/(\text{s} \cdot \text{mm}^2 \cdot \text{mrad}^2 \cdot \text{BW}) \tag{5.4.3}$$

Another important property of SR radiation is the degree of *coherence*. The electrons in a beam bunch emit SR from bending by a simple magnet or from the oscillating trajectories in an insertion device (wiggler or undulator). The SR emitted by individual electrons in single magnets and wigglers adds *incoherently*: if the bunch contains N particles, the total intensity (per unit frequency or *spectral bandwidth*) is simply N times the intensity from an individual particle. In contrast, if the electron trajectories at a given pole are all in phase, the resulting intensity of SR will be proportional to N^2. This type of radiation is called *coherent synchrotron radiation* or

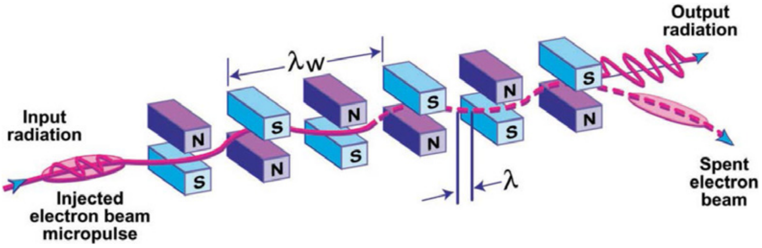

Figure 5.4. Free-electron laser concept: an electron beam interacts with a planar wiggler to produce radiation of wavelength λ. Source: O'Shea and Freund (2001). Reproduced with permission of IEEE. See [9].

CSR, which is seen from undulators. Although SR from wigglers is incoherent, they yield more intense SR than single-bend magnets because they are longer and involve multiple bends. Further, since the number of particles in a typical bunch can be very large (10^{10} for a 1.6 nC bunch, for example), the intensity of a coherent source can be many orders of magnitude larger than the intensity of an incoherent one. In reality, the SR intensity always has incoherent and coherent components; their ratio is intimately related to the structure of the beam bunch, i.e. its *line density profile*, and the geometry and dimensions of the storage ring and/or the insertion device. In free-electron lasers (FELs), to be described briefly below, additional effects occur from the interaction of the emitted SR and the electrons themselves.

In FELs the electron trajectories are modulated by the magnetic field of a wiggler, radiating photons that interact back with the electrons to produce *coherent bunching* accompanied with coherent radiation. Figure 5.4 shows the schematics of a basic FEL.

To understand the process in some detail, we can describe the wiggler field as a traveling EM wave in the reference frame of the electron beam. This wiggler wave adds up to the SR wave to produce a beat wave with the same frequency of the SR wave but smaller phase velocity. Because the beat wave speed is less than c, it can get in synchronization with the electron beam (of axial speed v) and generate coherent bunches: essentially, the beat wave is an interference pattern that traps and synchronizes electron motion and radiation leading to a process akin to stimulated emission in atomic systems. If k is the light wave number and k_w the wiggler wave number, the phase-matching or resonance condition is $\omega/(k+k_w) \approx v$. Combining this expression with the basic formula for the light wave, $\omega = ck$, we obtain the following basic relation among FEL wavelength λ, wiggler spacing λ_w, and electron beam energy (as given by the gamma factor γ) for highly relativistic electrons [19]:

$$\lambda \approx \frac{\lambda_w}{2\gamma^2}. \tag{5.4.4}$$

A more detailed derivation shows that a factor $(1 + K^2/2)$, as in equation (5.4.2) for undulator SR at discreet wavelengths, is needed in equation (5.4.4). K, called the FEL parameter, is of order 1. From equation (5.4.4), it is clear that the FEL wavelength is *tunable* through the electron energy. For example, at electron energies of 4.54 and 14.35 GeV, and undulator period $\lambda_w = 3$ cm, and $K = 3.71$ (parameters of the Linac Coherent Light Source (LCLS) at SLAC) we get $\lambda = 1.5$ nm, 0.15 nm.

FELs can be implemented as either *oscillators* or *amplifiers*. In the first case, the radiation is bounced back by mirrors like in a regular laser cavity until the coherent radiation builds up and escapes through a semi-transparent mirror. These oscillator FELs, which can be implemented in storage rings, are low-gain devices that use high-energy, low-current electron beams. In the amplifier scheme, on the other hand, laser radiation of the desired wavelength passes once through the wiggler and is amplified by the generated coherent electron bunches; this is the type of FEL called 'seeded'. Alternatively, coherent radiation can build up from noise alone in a process called SASE (self-amplified spontaneous emission). In SASE FELs there is output power saturation because of bunch degradation as the electrons recoil randomly with every emitted photon. The SASE FELs (e.g. FLASH at DESY and LCLS at SLAC) are high-gain devices that require electron beams with very high peak current (kA) and low transverse emittance.

5.5 Longitudinal beam emittance and space charge

Since the longitudinal velocities of particles in a beam are typically orders of magnitude larger than the transverse velocities, and the energy spreads relative to the design energies are also small, the beams are considered 'cold' in the longitudinal direction. Thus, the Hamiltonian is separated into transverse and longitudinal components, with Boltzmann factors and corresponding temperatures defined for the transverse and longitudinal directions. This separation is of course artificial as there are many instances of longitudinal-transverse coupling that tend to equalize over time the transverse and longitudinal kinetic temperatures (see [10], chapters 5 and 6). However, we will assume here that this coupling can be neglected over the time and spatial scales of interest.

We augment the 4D vector (x, p_x, y, p_y) of the transverse case with two additional components for the longitudinal direction: $(z, \Delta p_z/p_o)$. The longitudinal coordinate and momentum difference are: $z(t) = s(t) - s_o(t)$, $\Delta p_z(t) = p(t) - p_o(t)$, where the quantities $s_o(t)$ and $p_o(t)$ represent the beam centroid position and design momentum, respectively. The *longitudinal rms emittance* (unnormalized) can be defined in terms of rms spread in longitudinal position and rms fractional momentum deviation:

$$\varepsilon_{z\text{rms}} = z_{\text{rms}} \frac{\left(\Delta p_z\right)_{\text{rms}}}{p_0}. \tag{5.5.1}$$

The normalized rms longitudinal emittance is defined as in the transverse case (chapter 4):

$$\varepsilon_{zn} = \gamma_0 \beta_0 \varepsilon_{z\text{rms}}, \tag{5.5.2}$$

where γ_0, β_0 are the design values of the relativistic parameters. If we choose the total energy E and time t as canonical conjugate variables instead of z, $\Delta p_z/p_0$, the normalized emittance is defined as

$$\varepsilon_{zn}^* = (\Delta E)_{\text{rms}} (\Delta t)_{\text{rms}}, \tag{5.5.3}$$

where the asterisk distinguishes this emittance from the one in equation (5.5.2). In terms of the RF phase ϕ (sections 5.1, 5.2), we can use $(\Delta\phi)_{\text{rms}} = \omega_{\text{RF}}(\Delta t)_{\text{rms}}$ instead of $(\Delta t)_{\text{rms}}$. The emittances in equations (5.5.2) and (5.5.3) are connected by the relation

$$\varepsilon_{nz} = \frac{\varepsilon^*_{nz}}{mc}, \tag{5.5.4}$$

as can be seen from $\Delta E = mc^2\Delta\gamma$, $\Delta p_z = mc\beta^{-1}\Delta\gamma$, and $\varepsilon_{zn} = z_{\text{rms}}(\Delta p_z)_{\text{rms}}/mc$.

It is also convenient to use (z, z') as variables, where the *longitudinal angle* z' is defined by

$$z' \equiv \frac{\mathrm{d}z}{\mathrm{d}s} = \frac{\Delta\beta}{\beta_0} = \frac{\Delta p}{\gamma_0^2 p_0}. \tag{5.5.5}$$

The axial distance was defined above: $z(t) = s(t) - s_0(t)$. Equation (5.5.5) follows from $\mathrm{d}z/\mathrm{d}s = (\mathrm{d}z/\mathrm{d}t)(\mathrm{d}t/\mathrm{d}s) = \Delta v_z/v_0$, and $\Delta v_z = \Delta p_z/(m\gamma_0^3)$—see [10], prob. 5-11a. With this definition, the unnormalized rms emittance in (z, z') space, $\varepsilon^{\text{rms}}_{zz'}$, is related to $\varepsilon_{z\text{rms}}$ (equation (5.5.1)) by

$$\varepsilon^{\text{rms}}_{zz'} = \frac{\varepsilon_{z\text{rms}}}{\gamma_0^2}. \tag{5.5.6}$$

The factor γ_0^{-2} reflects the Lorentz contraction of a straight bunch. From equations (5.5.1), (5.5.6), (5.5.17), and $\varepsilon_{zz'} = z_m z'_m = 5\varepsilon^{\text{rms}}_{zz'}$ (see below), we can write for the *total longitudinal emittance*

$$\varepsilon_{zz'} = \frac{5\varepsilon_{z\text{rms}}}{\gamma_0^2} = \frac{5z_m}{\gamma_0^2\sqrt{5}}\frac{(\Delta p_z)_{\text{rms}}}{p_0}, \tag{5.5.7}$$

which can be cast in terms of the rms energy spread as

$$\varepsilon_{zz'} = \frac{5z_m}{\beta_0^2\gamma_0^3\sqrt{5}}\frac{(\Delta E)_{\text{rms}}}{mc^2}. \tag{5.5.8}$$

We have used $(\Delta p_z)_{\text{rms}}/p_0 = (\Delta E)_{\text{rms}}/\beta_0^2 mc^2$. The CERN technical note by Bovet *et al* (see [11]) presents a good summary of formulas that are useful for the derivations above.

We now set up the stage for a simple treatment of *longitudinal space charge*. Let us assume that we have a traveling-wave linac (see section 5.1) and a beam bunch that is short compared to the RF wavelength. With this short-bunch approximation, the applied longitudinal force is *linear* (figure 5.2). The use of a traveling-wave, on the other hand, provides a physical basis for a *smooth approximation* of the actual periodic RF longitudinal focusing system.

The *applied external force* is defined relative to the synchronous particle (i.e. in the beam frame of reference) with phase ϕ_S (section 5.2):

$$F_{az} = qE_m\left[\sin\phi - \sin\phi_s\right] \cong -\left(\frac{qE_m\omega_{\rm RF}}{\beta_0 c}\cos\phi_s\right)z, \tag{5.5.9}$$

where E_m is the peak longitudinal electric field of the RF wave, $\phi - \phi_s = -(\omega_{\rm RF}/\beta_0 c)z$, and $\phi \approx \phi_s$. Thus, the equation of motion for *small synchrotron oscillations* without space charge and with a *small rate of acceleration* can be written as [3, 4, 10]:

$$z'' + \kappa_{z0}z = 0, \qquad \kappa_{z0} = \frac{2\pi}{\lambda_{\rm RF}}\frac{qE_m}{mc^2\beta_0^3\gamma_0^3}\left|\cos\phi_s\right|. \tag{5.5.10}$$

In the time domain, we have

$$\ddot{z} + \Omega_s^2 z = 0, \qquad \Omega_s^2 = \frac{2\pi}{\lambda_{\rm RF}}\frac{qE_m}{m\beta_0\gamma_0^3}\left|\cos\phi_s\right|, \tag{5.5.11}$$

since $\Omega_s^2 = v_0^2 k_{z0}^2 = \beta_0^2 c^2 \kappa_{z0}$. A more general version of equation (5.5.11) valid for large or small oscillations leads to equation (5.2.1); this equation was used to plot the curves of figure 5.3 in $(\Delta E \equiv \delta U, \phi)$ space. We note that the treatment of synchrotron oscillations in [4], the source of equation (5.2.1), is done for circulating beams, but the translation to straight machines is simple. For a circulating beam in a ring synchrotron, equation (5.5.11) is replaced by

$$\ddot{z} + \Omega_s^2 z = 0, \qquad \Omega_s^2 = \frac{\omega^2 h\,|\eta_{\rm tr}|}{2\pi}\frac{qV}{mc^2\beta_0^2\gamma_0}\left|\cos\phi_s\right|, \quad \text{circular machine.} \tag{5.5.12}$$

The angular RF frequency is an integer multiple h (normally very large), called the *harmonic number*, of the bunch circulating frequency: $\omega_{\rm RF} = h\omega$. Here $\omega = \beta_0 c/R_{\rm m}$, with $R_{\rm m}$ the machine radius. The peak field E_m and the *peak voltage gain per turn* V are connected by $E_m = V/2\pi R_{\rm m}$. Finally, the parameter $\eta_{\rm tr}$ (equation (3.6.6)) is $-1/\gamma_0^2$ for a straight accelerator because the momentum compaction factor is zero in that case (equation (3.6.1)).

In addition to a linear external force, we would like the force from longitudinal space charge to be linear also. An attempt to extend the 4D K–V distribution (chapter 4) to 6D, however, yields a nonlinear space charge field in the longitudinal direction ([10], prob. 5-12). This extension would involve a uniformly charged 6D hyperellipsoid in phase space. If we consider instead an ellipsoid in 3D with uniform volume charge density ρ_0 (in C m^{-3}), as illustrated in figure 5.5, the electrical potential can be found analytically.

If the ellipsoid shape satisfies the equation $(r/a)^2 + (z/z_m)^2 = 1$, where a, z_m are half-dimensions along r and z (figure 5.5), the *free-space potential* (i.e. with no pipe

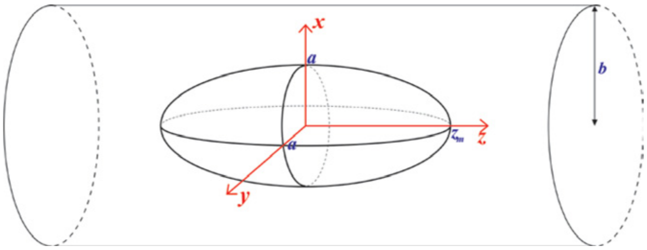

Figure 5.5. Ellipsoidal uniformly-charged bunch in a cylindrical pipe.

present) will be quadratic in r and z, and the *line charge density* (in C m^{-1}) takes a parabolic profile:

$$\Lambda(z) = \Lambda_0\left(1 - \frac{z^2}{z_m^2}\right), \qquad \Lambda_0 = \rho_0 \pi a^2. \tag{5.5.13}$$

Then, the longitudinal component of the self-electric-field is linear in z:

$$E_{sz}(z) = -\frac{g(z)}{4\pi\varepsilon_0\gamma_0^2}\frac{\partial\Lambda}{\partial z} = \frac{2g(z)}{4\pi\varepsilon_0\gamma_0^2}\frac{\Lambda_0}{z_m^2}z. \tag{5.5.14}$$

The function $g(z)$ defines the dimensionless 'geometry g-factor'; it is of order unity and depends on the distance z from the bunch centroid, and the aspect ratio z_m/a of the bunch. Reiser quotes results for the g-factor g_0 in free space, the g-factor at the center of the bunch $g(0)$, and the average (over the beam distribution) g-factor g that includes image effects. We only quote the asymptotic result for a *long bunch*:

$$g_{\text{asymp.}}(0) = 2\ln\left(\frac{b}{a}\right), \tag{5.5.15}$$

where b is the radius of the cylindrical pipe (figure 5.5). (A detailed derivation of equation (5.5.15) can be found in USPAS notes by Barnard and Lund [12]). In reality, because of image charges the longitudinal self-electric field will be affected by the presence of the conducting pipe. Thus, deviations from linearity will be significant near the ends of long bunches. Additional considerations related to the g-factor of line-charge density *perturbations* are discussed in chapter 6 of [10].

Referring again to figure 5.5, we find that the *rms bunch's length* z_{rms} is

$$z_{\text{rms}} = \langle z^2\rangle^{1/2} = \left(\frac{\int_{-z_m}^{z_m}\Lambda(z)z^2\,\mathrm{d}z}{\int_{-z_m}^{z_m}\Lambda(z)\,\mathrm{d}z}\right)^{1/2}, \tag{5.5.16}$$

which can be easily calculated from equation (5.5.13):

$$z_{\text{rms}} = \frac{z_m}{\sqrt{5}}. \tag{5.5.17}$$

It turns out that the line density profile of equation (5.5.13) corresponds to the limit of *zero longitudinal temperature* of the general line-charge density derived from the longitudinal Boltzmann factor for a matched (to the RF system) bunch. In this limit, the longitudinal space charge force is exactly balanced by the applied *linear* external RF force (equation (5.5.9)). Furthermore, and as in the transverse case, the high-temperature limit or zero-longitudinal-space-charge limit yields a Gaussian density profile for $\Lambda(z)$, which is by far the most commonly used model in computer simulations of longitudinal beam dynamics.

Neuffer has derived in his seminal 1979 paper [13] the form of the particle distribution in (z, z') space that is the equivalent longitudinal version of the K–V distribution (equation (4.2.7)):

$$f(z, z', s) = \frac{3N}{2\pi\varepsilon_0}\sqrt{1 - \frac{z^2}{z_m^2} - \frac{z_m^2}{\varepsilon_{zz'}^2}\left(z' - \frac{z'_m}{z_m}z\right)^2}, \tag{5.5.18}$$

where N is the total number of particles in the bunch, z' is defined by equation (5.5.5), and the *total emittance* $\varepsilon_{zz'} = z_m z'_m$ satisfies the Courant–Snyder formula for the ellipse in longitudinal phase space (z, z'):

$$\gamma_z z^2 + 2\alpha_z zz' + \beta_z z'^2 = \varepsilon_{zz'}. \tag{5.5.19}$$

From equation (5.5.14) we can obtain the *focusing constant of longitudinal linear space charge*. Following the pattern of equation (5.5.10) we find

$$\kappa_z^{\text{sp–ch.}} = \frac{q^2 g}{2\pi\varepsilon_0 mc^2\beta_0^3\gamma_0^5}\frac{\Lambda_0}{z_m^2}. \tag{5.5.20}$$

Further, since the total charge in the bunch is $Q = qN = (4/3)\Lambda_0 z_m$, and we normally have electrons, i.e. $q = -e$, we obtain $\kappa_z^{\text{sp–ch.}} = K_\text{L}/z_m^3$. K_L defines the *longitudinal beam perveance* (in m):

$$K_\text{L} = \frac{3}{2}\frac{gNr_\text{e}}{\beta_0^2\gamma_0^5}. \tag{5.5.21}$$

The constant r_e is the classical electron radius. With this notation, we combine equations (5.5.10) and (5.5.14) to write a *single-particle* equation of longitudinal motion that includes external and internal linear forces:

$$z'' + \kappa_{z0}\, z - \frac{K_\text{L}}{z_m^3}z = 0. \tag{5.5.22}$$

The *longitudinal envelope equation*, i.e. the equation for the bunch's half-width z_m can be derived from the Neuffer distribution, equation (5.5.18), and Vlasov equation (see [13]), or more simply by just doing the substitution $z \to z_m$ and adding and emittance term to equation (5.5.22):

$$z''_m + \kappa_{z0} z_m - \frac{K_\text{L}}{z_m^2} - \frac{\varepsilon_{zz'}^2}{z_m^3} = 0. \tag{5.5.23}$$

In terms of rms quantities, the envelope equation is rewritten as

$$z''_{\rm rms} + \kappa_{z0}\, z_{\rm rms} - \frac{K_{\rm L}}{5\sqrt{5}\, z^2_{\rm rms}} - \frac{(\varepsilon^{\rm rms}_{zz'})^2}{z^3_{\rm rms}} = 0, \tag{5.5.24}$$

from equation (5.5.17), and $\varepsilon_{zz'} = z_m z'_m = 5\varepsilon^{\rm rms}_{zz'}$. Note that the *effective bunch half-length* is $\sqrt{5}\; z_m \cong 2.24\, z_m$, compared to the factor of $\sqrt{4} = 2$ for the transverse case (chapter 4); the corresponding effective longitudinal angle is $\sqrt{5}\; z'_m$. Another major difference between the envelope equations for the transverse and longitudinal cases is the dependence of the space-charge term on the effective beam envelope half-width. We have the space charge term $K/2X(s)$ for the transverse case (equations (4.3.2) and (4.3.3) with $R = 2X$), but $K_{\rm L}/5\sqrt{5}\, z^2_{\rm rms}$ above.

Just as in the transverse case, a *tune depression* and a corresponding space-charge *intensity parameter* (Harris, [16]) can be defined for the longitudinal beam dynamics. Furthermore, an equivalent Neuffer distribution can be defined for non-parabolic line density profiles, just as an equivalent K–V is defined for arbitrary transverse particle distributions with elliptical symmetry. From the smooth approximation $z''_{\rm rms} = 0$ of equation (5.5.24), we can easily obtain a longitudinal SC intensity parameter in parallel with the transverse case (equation (4.3.5)):

$$\chi_{\rm L} = \frac{K_{\rm L}/5\sqrt{5}\, z^2_{\rm rms}}{\kappa_{z0}\; z_{\rm rms}} = \frac{K_{\rm L}}{K_L + \dfrac{5\sqrt{5}\,(\varepsilon^{\rm rms}_{zz'})^2}{z_{\rm rms}}}. \tag{5.5.25}$$

An equivalent expression ([16]) is $\chi_{\rm L} = K_{\rm L}/[K_{\rm L} + (\varepsilon^2_{zz'}/z_m)]$. Beam bunches are considered to be emittance dominated if $0 \leqslant \chi_{\rm L} < 0.5$ and space-charge dominated if $0.5 < \chi_{\rm L} \leqslant 1$.

Because of the small energy spreads of most beams of practical interest, which implies small longitudinal emittances, longitudinal SC effects can be significant even at high energies. In particular, in the absence of longitudinal focusing, beams ‘debunch’, i.e. elongate until the bunch ends meet after relatively few turns in circular machines. To illustrate this expansion we estimate the debunching length for the 6 mA (flat-top current), 100 ns (initial duration) bunch at the University of Maryland Electron Ring – UMER (see chapter 6). The results of solving equation (5.5.23) are shown in figure 5.6. First of all, it is straightforward to show that the rms half-length of a (initially) rectangular line-charge density profile is $z_{m0}/\sqrt{3}$, where z_{m0} is the initial half-length. Thus, to construct the *equivalent parabolic profile* we need to set the equivalent maximum half-length to $z_{\rm par0} = \sqrt{5/3}\, z_{m0}$; in this way the two profiles (figure 5.6(a)) yield the same rms half-lengths. Furthermore, the peak line-charge density of the parabolic profile must be $\Lambda_{p0} = (3/4)(Q/z_{p0})$, so that both the rectangular and parabolic bunches have the same total charge $Q = 0.6$ nC. Finally, we assume that the two bunches have the same *rms energy spread* of 100 eV, i.e. 1% of the nominal 10 keV in UMER, and use equation (5.5.8) to calculate the total longitudinal emittance. We find that the bunch doubles its length filling the ring in a little more than 20 turns.

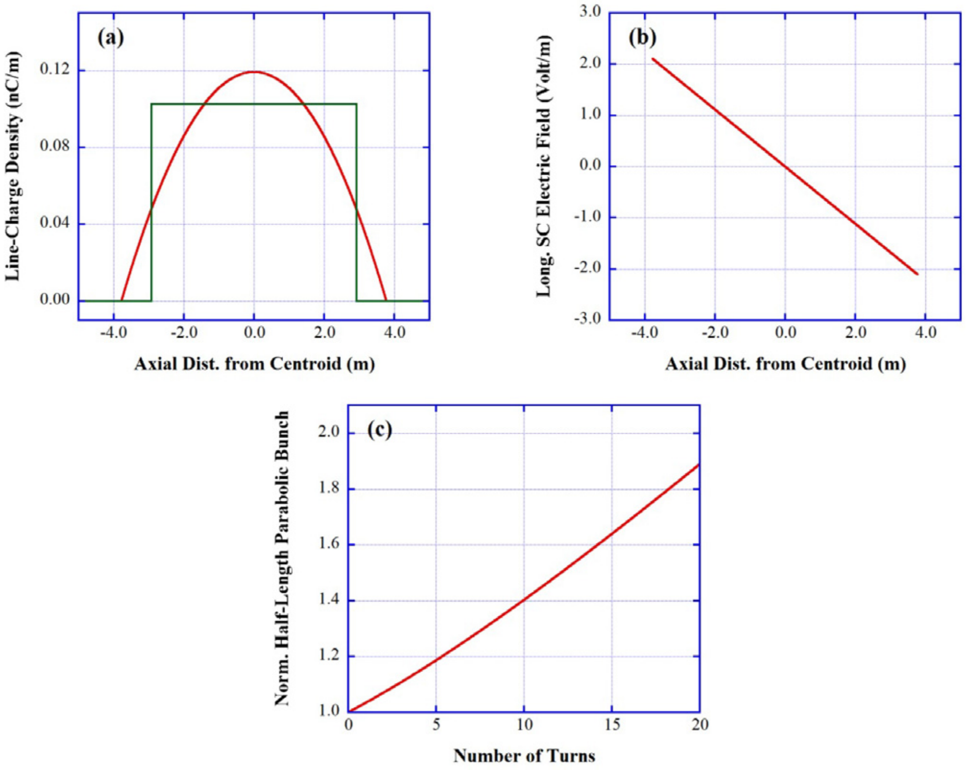

Figure 5.6. Debunching calculation of 6 mA, 10 keV, 100 ns, 100 eV (rms energy spread) electron bunch: (a) line-charge density profiles of rectangular and (equivalent) parabolic bunches; (b) space-charge longitudinal electric field of parabolic bunch; (c) bunch expansion versus number of turns in UMER (see chapter 6).

The calculation can be approached differently, taking advantage of a simple 1D fluid model (see e.g. [14]). In this model the ‘sound’ (line-charge density rarefaction) speed inside the beam is

$$C_S = \sqrt{\frac{eg\Lambda_0}{4\pi\varepsilon_0\gamma_0^5 m_e}}, \tag{5.5.26}$$

where g, Λ_0 were defined before. We find $C_S = 7.7\times10^5\ \mathrm{ms}^{-1}$, which implies a debunching time of 1.83 μs, or about 10 turns. This latter result is closer to experimental observations [15], indicating that the fluid model may be better in this instance. Further, the main reason for the discrepancy may be that the longitudinal space charge forces at the *bunch ends* are much stronger for an initially ‘square’ current profile (see first equality in equation (5.5.14)), as in the UMER beam, than for the parabolic profile assumed in the Neuffer model.

To conclude this section, we point out that the K–V and Neuffer models of linear space charge can be combined in an *ad hoc* fashion. Thus, a set of *coupled envelope equations* can be written ([10], section 5.4.11) which include a redefined beam perveance containing *both* the beam radius and bunch length. The smooth approximation form of the equations leads to algebraic equations which can be solved in cases of practical interest such as when the aspect ratio of the bunch is small (‘short’ bunch) and the radius of the vacuum pipe is much larger than the beam radius.

Computer resources

A free program called ***Radiation2D***, written by Tsumoru Shintake of RIKEN in Japan, provides a great educational tool for illustrating the radiation pattern of a moving charged particle following different geometries. For example, the reader can study: 1) the change in electric field lines for different speeds (as fractions of the light speed) of a particle moving uniformly on a straight path; 2) the radiation pattern (again for different speeds) of a particle moving in a circle; 3) the radiation pattern in a bending magnet; 4) the radiation pattern in an undulator. Other similar programs are freely available, such as the Java applet ***radiating-charge_en.jar***, which can be downloaded or run directly at http://phet.colorado.edu/en/simulation/radiating-charge.

A Java applet written by Wolfgang Christian from Davidson College illustrates very nicely a 1D pendulum model of a FEL. It can be run online or as a standalone; it requires Java. In Ubuntu Linux, the simple terminal instruction ‘java-cp . FelOde’ will work. The webpage http://webphysics.davidson.edu/Applets/FELPart/FelOde.html includes the applet and instructions and ideas for exploration. Especially interesting is the illustration of electron bunching in an energy-phase diagram, similar to the workings of RF in accelerators.

We also include in the book’s website a number of Mathcad programs: ***DipoleRadiation.xmcd*** is used to calculate the basic pattern of dipole radiation. ***BiasPend_RFBucket.xmcd*** can be employed to reproduce the results of figure 5.3. ***LongEmitt-SpCharge.xmcd*** reproduces the calculations of bunch elongation illustrated in figure 5.6 and based on the longitudinal envelope equation (5.5.23).

There is also the Android app TAPAS (see appendix) which is useful for quick calculations of e.g. energy gain and RF power in linacs, synchrotron radiation parameters for electron storage rings and insertion devices, and others.

References

[1] Joseph C L and Bernal S 2016 *Modern Devices: The Simple Physics of Modern Technology* (New York: Wiley) www.wiley.com/go/joseph/moderndevices

[2] Wiedemann H 2007 *Particle Accelerator Physics* 3rd edn (Berlin: Springer)

[3] Wangler T P 2008 *RF Linear Accelerators* 2nd edn (Weinhem: Wiley)

[4] Conte M and MacKay W W 1991 *An Introduction to the Physics of Particle Accelerators* (Singapore: World Scientific)

[5] Henderson S, Holmes J and Zhang Y 2009 *Lecture 9a Synchrotron Radiation* (Nashville, TN: USPAS)

[6] Emery L 2002 *Lecture Notes Physics 575 – Accelerator Physics and Technologies for Linear Colliders, winter 2002, Chapter 5 – Damping Rings* (Lemont, IL: Argonne National Laboratory)

[7] Wolski A 2014 *Beam Dynamics in high Energy Particle Accelerators* (London: Imperial College Press)
[8] Lee S Y 2004 *Accelerator Physics* 2nd edn (Singapore: World Scientific)
[9] O'Shea P G and Freund H P 2001 Free-electron lasers: status and applications *Science* **292** 8
[10] Reiser M 2008 *Theory and Design of Charged Particle Beams* 2nd edn (New York: Wiley)
[11] Bovet C, Gouiran R, Gumowski I and Reich K H 1970 A selection of formulae and data useful for the design of A.G. Synchrotrons *CERN Technical Note DL/70/4*
[12] Barnard J and Lund S 2015 *Injectors and Longitudinal Physics – II, USPAS Notes* (Hampton, VA: USPAS)
[13] Neuffer D 1979 Longitudinal motion in high current ion beams—a self-consistent phase space distribution with an envelope equation *IEEE Trans. Nuclear Sci.* **NS-26** 3
[14] Ho D D-M, Brandon S T and Lee E P 1991 Longitudinal beam compression for heavy-ion inertial fusion *Part. Accel* **35** 15
[15] Koeth T W, Beaudoin B, Bernal S, Haber I, Kishek R A and O'Shea P G 2011 Bunch-end interpenetration during evolution to longitudinal uniformity in a space-charge-dominated storage ring 2011 *Proc. of 2011 Particle Accelerator Conference, New York*
[16] Harris J R 2002 Longitudinal effects and focusing in space-charge dominated beams *Master's Thesis*, University of Maryland, College Park, MD
[17] Winick H (ed) 1994 *Synchrotron Radiation Sources—A Primer* (Singapore: World Scientific)
[18] Bryant P J and Johnsen K 1993 *The Principles of Circular Accelerators and Storage Rings* (Cambridge: Cambridge University Press)
[19] Freund H P and Antonsen T M 1996 *Principles of Free-Electron Lasers* 2nd edn (London: Chapman & Hall)

Chapter 6

Applications and examples

We discuss in the first two sections of this chapter two applications or extensions of the basic theory discussed so far: *RMS periodic envelope matching*, and *betatron resonances*. The first topic is in practice a computer exercise that many accelerator designers and operators have to address. Charged-particle beams are born with parameters that are normally not suited for transport in the periodic lattice of a linac or ring accelerator or storage ring. Thus a transfer/injection section is required to modify the beam before it can be transported in the periodic lattice. However, instead of discussing the 'matching-to-target' problem we study examples of matching in the periodic lattice, including full *incoherent space charge*. We present useful relations for calculating 'average' RMS beam dimensions; these numbers can be used as initial guesses in any algorithm that finds periodic envelope solutions. In section 6.2, we present a simple treatment of *betatron resonances*, starting with integer resonances and then moving on to a more general theory. In the last two sections we show how to employ theory developed in the previous chapters to verify typical parameter tables found in the home websites of accelerators. Thus, we give in section 6.3 examples of two *linacs* and their characterization, and in the last section we illustrate calculations for three *rings*, two light sources and a high intensity storage ring. Space charge does not play a significant role for the operation of standard electron circular machines, but it is the main feature of the low-energy machine of the third example. The computer resources include MAD-8 and Winagile files for the machines discussed, a Matlab program for envelope matching, Mathcad worksheets, and simulation movies for resonances.

6.1 Periodic-envelope FODO matching

Beams typically traverse a transport section for matching and injection into a periodic lattice which can be linear or closed. In the latter case the lattice is often

doi:10.1088/978-1-6817-4076-8ch6

referred to as 'circular' although the actual shape of the beam line is much closer to a regular polygon. We discuss in this section the problem of finding periodic solutions of the K–V envelope equations (chapter 4) in a periodic lattice. We do not cover the problem of matching *or* injection into the periodic lattice by means of a transfer beam-line; this problem, when space charge is not a factor, is covered in books such as Bryant and Johnsen [1]. When space charge is important, the paper by Bernal *et al* [2] is relevant.

We consider an unbunched beam, centered on the vacuum pipe, and having a transverse distribution with elliptical symmetry. Therefore, an equivalent K–V distribution and the K–V envelope equations can be applied. We are interested in calculating the periodic beam envelopes in an asymmetric FODO lattice with specified zero-current phase advance per period, σ_{0X}, σ_{0Y}. We start by obtaining the quadrupole strengths that are required. The simplest calculation employs thin quadrupoles with focal lengths $f = \pm(1/\kappa_q l_q)$ and equal zero-current phase advances per period, $\sigma_{0X} = \sigma_{0Y} = \sigma_0$. We obtain, after straightforward matrix multiplication,

$$|\kappa_q| = 4\frac{\sin(\sigma_0/2)}{Sl_q} \tag{6.1.1}$$

The latter equation yields a peak quadrupole strength that is correct within a few percent. However, more accurate and general results can be derived using matrices that include trajectory changes inside the quadrupoles, as well as $\sigma_{0X} \neq \sigma_{0Y}$. The relevant equations were presented in chapter 3, equations (3.2.4) through (3.2.7), and examples given for specified zero-current phase advances. Let us start with a *symmetric* FODO lattice as in figure 3.2. We assume again a lattice period S = 0.32 m, quadrupoles with effective length $l_q = 0.0516$ m, and a zero-current phase advance $\sigma_0 = 30°$. We found by solving equation (3.2.4) for θ that $\kappa_q = 70.78\ \text{m}^{-2}$. The beam envelope in the FODO cell will depend not only on the quadrupole strength just found, but also on the beam perveance K (determined by the energy, beam current and type of particle) and emittance. Before proceeding to numerically solve the K–V envelope equations, we can obtain a good estimate of the 'average' beam envelope transverse dimension by using the smooth approximation. For an emittance-dominated beam we can employ the zero-current result $a_0 = \sqrt{\tilde{\varepsilon}_{\text{rms}}/k_0}$, with $k_0 = \sqrt{\kappa_q}$. As an example, let us consider a beam with perveance $K = 1.5 \times 10^{-6}$ (e.g., 0.1 mA, 10 keV electron beam) and effective emittance $\tilde{\varepsilon}_{\text{rms}} = 6.0$ µm in both transverse planes. Thus we find $a_0 = 1.9$ mm. We can use this estimate as the first guess for solving the K–V envelope equation (4.4.10) in the FODO cell. The solution for the periodic envelope is found using the periodic-matcher routine of the Matlab code Menv described in the appendix. The result is shown in figure 6.1. Note from the figure that the 'average' beam semi-axis dimension is 2.0 mm, very close to a_0.

The same result of figure 6.1 can be obtained with essentially any of the codes described in the appendix, but the popular matrix code Trace 2D would perhaps be the best alternative.

The beam envelope is dramatically different if the beam is strongly space-charge dominated. Let us repeat the calculation for a $K = 1.5 \times 10^{-3}$ beam (e.g., 100 mA,

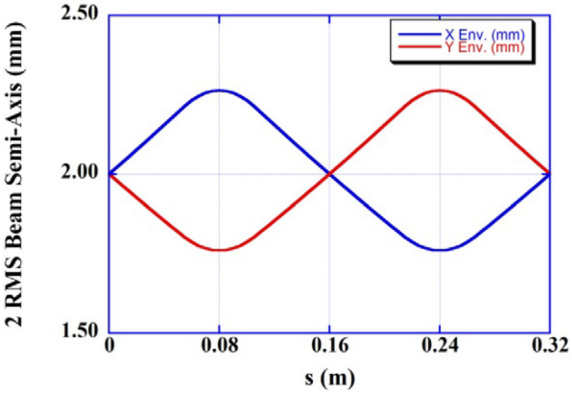

Figure 6.1. Beam envelope in a symmetric FODO lattice. The beam perveance is $K = 1.5 \times 10^{-6}$, and the effective emittance is 6.0 μm (emittance-dominated beam). The quadrupole strengths yield a zero-current phase advance $\sigma_0 = 30°$.

10 keV electron beam) with effective emittance $\tilde{\varepsilon}_{\text{rms}} = 60$ μm. To estimate the beam transverse dimension we can use $a_{\text{B}} = \sqrt{K/k_0}$ (see equation (4.3.8)). We get $a_{\text{B}} =$ 24 mm. The beam envelopes calculated with Menv are shown in figure 6.2.

For intermediate space charge intensities, a surprisingly good approximation for the average beam radius is provided by the relation

$$a \cong \sqrt{a_0^2(k_0, \tilde{\varepsilon}_{\text{rms}}) + a_{\text{B}}^2(k_0, K)}, \tag{6.1.2}$$

where we have explicitly indicated the dependence on the *smooth-approximation* constant k_0, and the emittance and generalized beam perveance.

If the FODO lattice is *asymmetric* (as in figure 3.4) and $\sigma_{0X} = 30°$, $\sigma_{0Y} = 45°$, the solution for the quadrupole strengths is obtained from equations (3.2.6) and (3.2.7): $\kappa_1 = 84.67\ \text{m}^{-2}$, and $\kappa_2 = 94.40\ \text{m}^{-2}$. We assume the same beam perveances and emittances of the examples with the symmetric FODO lattice. This time, we expect different 'average' beam dimensions in the two transverse planes. If a and b represent these dimensions, the smooth-approximation equations to be solved to estimate these values are given by:

$$\begin{aligned} k_{0x}^2 a - \frac{2K}{a+b} - \frac{\tilde{\varepsilon}_x^2}{a^3} &= 0, \\ k_{0y}^2 b - \frac{2K}{a+b} - \frac{\tilde{\varepsilon}_y^2}{b^3} &= 0, \end{aligned} \tag{6.1.3}$$

which are the same as equations (4.4.11). We find $(a, b) = (2.0, 1.6)$ mm for the emittance-dominated beam used before, and $(a, b) = (27.8, 12.6)$ mm for the strongly space-charge dominated beam. The envelopes for both cases are shown in figure 6.3.

No bending dipole magnets were present in the previous examples. If dipoles are present, they change the FODO matching solution because of edge focusing. Trace 2D and 3D are more suitable for matching in these cases.

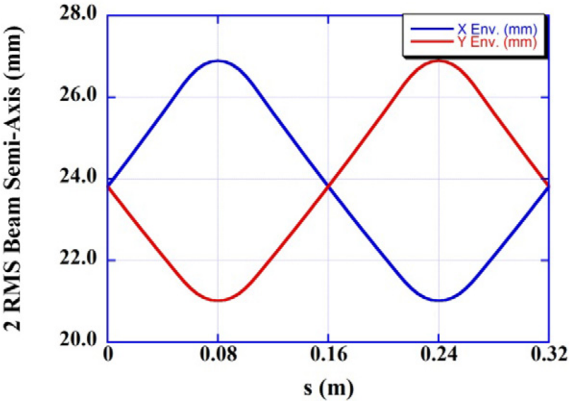

Figure 6.2. Beam envelope in a symmetric FODO lattice. The beam perveance is $K = 1.5 \times 10^{-3}$, and the effective emittance is 6.0 μm (strongly space-charge dominated beam). The quadrupole strengths yield a zero-current phase advance $\sigma_0 = 30°$.

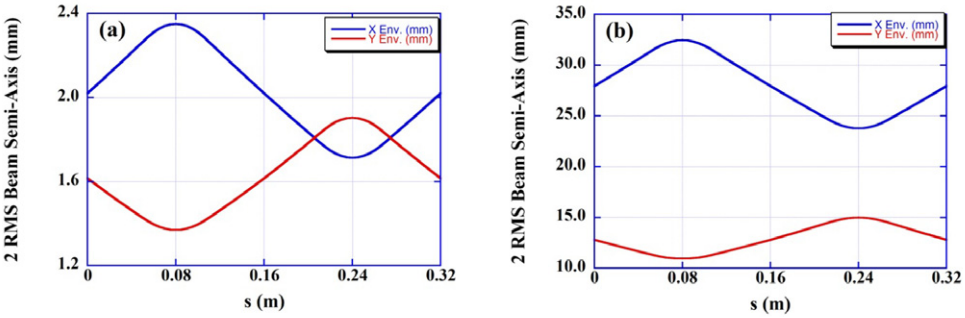

Figure 6.3. Beam envelopes in an asymmetric FODO lattice. (a) $K = 1.5 \times 10^{-6}$, 6.0 μm effective emittance; (b) $K = 1.5 \times 10^{-3}$, 60 μm effective emittance. The quadrupole strengths yield zero-current phase advances $\sigma_{0X} = 30°$, $\sigma_{0Y} = 45°$.

To conclude this section, we present a brief discussion of the beam envelope oscillations that ensue when the beam is not perfectly matched. Starting with the K–V envelope equations, equations (4.4.10), we define the *average* rms envelope semi-axis dimensions in the two transverse planes, $\bar{X}$ and $\bar{Y}$, as the solutions of the equations in the *smooth approximation*. Next we assume that the $X(s)$ and $Y(s)$ envelopes deviate by a small amount from their average values. The analysis of the linearized 'small oscillations' problem is standard (see e.g. [3]); it leads to two fundamental envelope modes with phase advances per period given by:

$$\begin{aligned} \sigma_{\text{sym.}} &= \sqrt{2\sigma_0^2 + 2\sigma^2}, \quad \text{symmetric mode,} \\ \sigma_{\text{asym.}} &= \sqrt{\sigma_0^2 + 3\sigma^2}, \quad \text{antisymmetric mode.} \end{aligned} \tag{6.1.4}$$

In the equations, σ_0, σ are the zero-current and full-current betatron phase advances per period. The first normal mode is the in-phase or 'breathing' mode; the second mode is the ‘antiparallel’ or quadrupolar mode. The modes are analogous to the ones occurring in two coupled harmonic oscillators such as pendula. In the first mode, the pendula swing in phase, while in the second mode the phases are 180° apart. The general motion of the oscillators is a linear superposition of the two modes. With zero current the two modes become one with a phase advance $\sigma_{\text{env}} = 2\sigma_0$, i.e. the envelope of the mismatched beam oscillates at twice the betatron frequency.

6.2 Betatron resonances

The betatron resonance condition in a circular machine such as a synchrotron or storage ring is expressed by

$$n\nu_{X0} \pm m\nu_{Y0} = Np, \tag{6.2.1}$$

where n, m. p and N are integers, and ν_{X0} and ν_{Y0} are the horizontal and vertical bare tunes (the notation Q_{X0}, Q_{Y0} is used in Europe). N is the *super-periodicity* of the machine, and $|n| + |m|$ is the *order* of the resonance. When $N > 1$, integer, we have ‘structure’ or ‘systematic’ resonances, whereas when $N = 1$, the resonances are associated with random errors in magnet strengths or locations. These latter resonances are called ‘non-structure’ resonances. A *working or operating point* (ν_{X0}, ν_{Y0}) is chosen so as to avoid the condition equation (6.2.1).

The most destructive resonances are the *linear resonances*, i.e. the first- and second-order resonances. First-order resonances are associated with dipole strength and rotational errors and also from quadrupole displacement errors. *Second-order resonances*, on the other hand, are caused by quadrupole (i.e. gradient) errors. The names integer and half-integer resonances are also employed to describe first- and second-order resonances, respectively. Further, linear resonances are independent of particle amplitude, while *non-linear* resonances, i.e., resonances of third or higher order, are not. We will give a motivation for equation (6.2.1) after discussing a simple treatment of integer resonances.

Dipole errors arise from bending magnet errors and also from quadrupole transverse displacement errors. We show now that integer resonances grow linearly by the turn. A dipole error will lead to an angle error (or ‘kick’) given by (see chapter 3)

$$x' = \frac{\delta B}{B\rho}\Delta s, \tag{6.2.2}$$

where Δs is the dipole’s effective length and ρ is the bend radius. Therefore, if x_0' is the initial slope at a given point in the reference orbit, the kick will lead to new slopes

$$x_1' = x_0' + \frac{\delta B}{B\rho}\Delta s, \qquad x_2' = x_1' + \frac{\delta B}{B\rho}\Delta s, \ \ldots, \tag{6.2.3}$$

after the first, second, and so on, revolutions. In general we’ll have

$$x_{\text{n}}' = x_0' + n\frac{\delta B}{B\rho}\Delta s, \tag{6.2.4}$$

for the nth turn. Now, we also know that $x_{n\,\max} = \sqrt{C\beta_n}$, $x'_{n\,\max} = \sqrt{C\gamma_n}$, where β, γ are the Courant–Snyder parameters for the horizontal motion, and C is the Courant–Snyder invariant (chapter 3). Therefore,

$$x'_{n\,\max} = x_{n\,\max}\sqrt{\frac{\gamma_n}{\beta_n}} = x_{n\,\max}\frac{\sqrt{1+\alpha_n^2}}{\beta_n}. \tag{6.2.5}$$

Finally, by setting $x'_n = x'_{n\,\max}$, $x'_0 = 0$, we get

$$x_{n\,\max} = n\frac{\delta B}{B\rho}\Delta s\frac{\beta_n}{\left(1+\alpha_n^2\right)^{1/2}} \to n\frac{\delta B}{B\rho}\Delta s\beta_{n\,\max}. \tag{6.2.6}$$

In the last step, we have used the fact that for $\alpha_n = 0$ we have $\beta_n = \beta_{n\,\max}$, i.e., we have assumed that the kick error occurs at the location of maximum β. This would be the case exactly for kicks from quadrupole displacement errors, since the quads are placed at the maxima (or minima) of the betatron function, but it is only an approximation for arbitrary location of a bending dipole with an error. If there are N_d dipoles in the ring, on the other hand, with a field error distribution having an *rms integrated error* $(\delta B/B)\Delta s$, equation (6.2.6) would have to be multiplied by $\sqrt{N_\mathrm{d}}$ to obtain the total orbit excursion. Figure 6.4 illustrates the change in orbit from an integer resonance. Additional considerations are given in [13].

As an example, we consider the compact University of Maryland Electron Ring [11]: $N_\mathrm{d} = 36$, $\Delta s = 0.0376$ m, $\beta_{x\,\max} = 0.54$ m (at $\nu_{0X} = 6.0$), $\rho = 0.275$ m. Therefore, for a 1% rms dipole field error ($(\delta B/B) = 0.01$), we get an orbit change of 4.4 mm per turn; the beam centroid would reach the vacuum pipe in less than six turns. Integer resonances are very destructive! We have implemented a simulation of the resonance in the code Winagile (see appendix); we include further details and hyperlinks to movies at the end of the chapter.

We can base a simple general treatment of resonances on the first equation of motion in equation (3.3.1), which we copy for reference:

$$x''(s) + \kappa_x(s)x = 0. \tag{6.2.7}$$

We now apply to equation (6.2.7) *Floquet's transformation* of variables,

$$\phi(s) = \frac{\psi(s)}{\nu_{X0}}, \qquad \eta(s) = \frac{x(s)}{\sqrt{\beta(s)}}, \tag{6.2.8}$$

to obtain

$$\frac{\mathrm{d}^2\eta(\phi)}{\mathrm{d}\phi^2} + {\nu_{X0}}^2\eta(\phi) = 0. \tag{6.2.9}$$

Equation (6.2.9) is a simple harmonic oscillator equation for the normalized variable η, and ν_{X0} can be recognized as the bare tune (no space charge included), introduced in chapter 3.

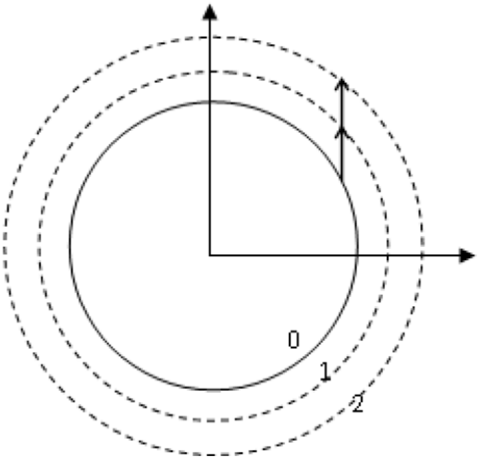

Figure 6.4. Schematic representation of an integer resonance—bird's view of how a particle is deflected by a dipole error kick into an orbit that grows linearly.

With field errors $\Delta B(\eta, \phi)$ representing all fields not defining the reference orbit, i.e., all random field errors from magnet construction, we have now the inhomogeneous equation [5, 6]:

$$\frac{\mathrm{d}^2\eta(\phi)}{\mathrm{d}\phi^2} + \nu_{X0}{}^2\eta(\phi) = -\nu_{X0}{}^2\beta^{3/2}\frac{\Delta B(\eta, \phi)}{(B\rho)}, \tag{6.2.10}$$

where $(B\rho)$ is the magnetic rigidity, and $\Delta B = B_0[b_0 + b_1(\phi)x + b_2(\phi)x^2 + \ldots]$ is a 1D (not the most general) expansion of the field errors. Therefore, equation (6.2.10) can be written as

$$\begin{aligned} \frac{\mathrm{d}^2\eta(\phi)}{\mathrm{d}\phi^2} + \nu_{X0}\eta(\phi) &= -\frac{\nu_{X0}{}^2B_0}{(B\rho)}[\beta^{3/2}b_0 + (\beta^{4/2}b_1)\eta + (\beta^{5/2}b_1)\eta^2 + \ldots] \\ &= -\frac{\nu_{X0}{}^2B_0}{(B\rho)}\sum_{k=\text{integer}} C_k\mathrm{e}^{\pm\mathrm{i}k\phi}, \end{aligned} \tag{6.2.11}$$

where we have written the inhomogeneous part of the equation as a sum of *driving terms*. An *integer resonance* would be excited if the dipole error represented by $\beta^{3/2}b_0$ is equal to $C_k\mathrm{e}^{\pm\mathrm{i}k\phi}$, with $k = \nu_{X0} =$ integer; a *half-integer resonance* would occur if $\beta^2b_0 = C_k\mathrm{e}^{\pm\mathrm{i}k\phi}$ such that $k - \nu_{X0} = \nu_{X0}$, i.e., $k = 2\nu_{X0}$. The difference $k - \nu_{X0}$ arises from the beat frequency between the kth harmonic of the quadrupole gradient error β^2b_0 and the oscillation at frequency ν_{X0} contained in the factor η in equation (6.2.11). By similar reasoning, the first nonlinear resonance, or *third-integer resonance*, occurs if $k - 2\nu_{X0} = \nu_{X0}$, or $k = 3\nu_{X0}$.

We assumed a super-periodicity $N = 1$ in the Fourier expansion of equation (6.2.11), second equality; in other words, the period of expansion was *one entire turn* on the circular accelerator. If the lattice has higher periodicity, however, the period of expansion would be equal to the length of the shorter repeating structure. Thus, in

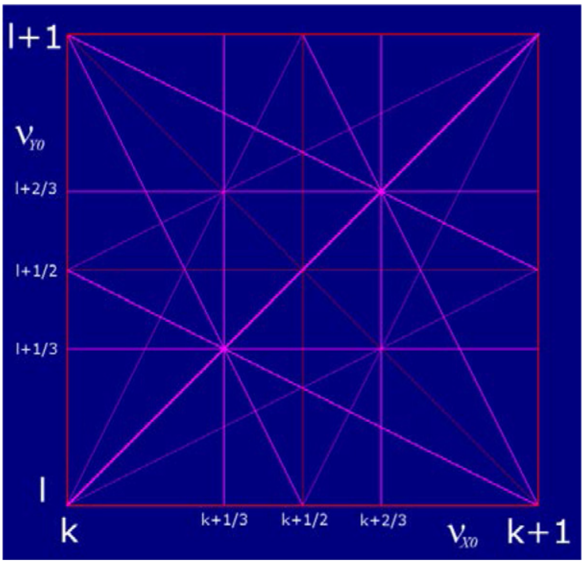

Figure 6.5. Resonance diagram for first-, second- and third-order resonances and super-periodicity $N = 1$. The numbers k and l are integers. The diagram is based on an original Winagile chart. See also [14].

an ideal 'ring' with six sections or super-periods we would have $N = 6$, with a correspondingly shorter period in the Fourier expansion. In an actual ring, the super-periodicity may be broken by the injection line which may contain special magnets and other elements. We can represent graphically the resonance condition equation (6.2.1) by plotting ν_{y0} versus ν_{X0} for a range of values of m, n and p. The *resonance diagram* with lines up to third order, and with $N = 1$, is shown in figure 6.5.

If the super-periodicity is $N > 1$, i.e., higher symmetry, the resonance condition equation (6.2.1) leads to more widely spaced resonances, which is desirable. However, these resonances are generally strong. *Sum resonances* occur when $\nu_{X0} + \nu_{Y0} =$ integer, while *difference resonances* are characterized by $\nu_{X0} - \nu_{Y0} =$ integer. These resonances are examples of *coupling resonances* arising from coupled motion in the transverse (betatron) degrees of freedom. The coupling may arise from rotated quadrupoles from misalignment, from skew quadrupole components present in even leveled magnets, or from solenoid fields. It turns out that the difference resonances are *stable*, while the sum resonances are *unstable* (see e.g. [6], chapter 5).

The actual resonance lines have width, unlike the chart in figure 6.5. This width, called the *resonance stop band*, is narrower the higher the order of the resonance. Furthermore, radiation damping (chapter 5) reduces the growing betatron amplitude near a resonance.

For the interested reader, a detailed treatment of resonance theory using Hamiltonian perturbation theory can be found in a 1978 classic monograph by G Guignard [7].

6.3 Examples of linacs

We present in this section two examples of linear accelerators: the SLAC electron linac, a facility near Stanford University in California, and the LEDA (Low-Energy Demonstration Accelerator) proton linac at Los Alamos National Laboratory.

Table 6.1. Main parameters of the SLAC 3 m linac unit.

RF Frequency, f_{RF}	2856 MHz
Shunt Impedance, r_s	53–60 MΩ/m
Length, L	3.048 m
Iris Separation, d	35.001 mm
Disk Diameter, $2b$	8.4–8.2 cm
Iris Diameter, $2a$	2.6–1.9 cm
Number of Cells	86
Quality Factor, Q	13 000–14 000
Phase between cells	120°
Accelerating Gradient,	>17 MV m^{-1}
Attenuation Constant, τ	0.57
RF Filling Time, t_{F}	0.95 μs
Peak RF Power, P_{t0}	35 MW

The original SLAC linac accelerated electrons to 50 GeV over a distance of about 3 km. The basic 3 m accelerating unit of the SLAC linac has become an industry standard and is in use in many normal-conducting linacs around the world. The unit, briefly mentioned in chapter 5, is an S-band, disk-loaded, constant-gradient, traveling wave structure. Table 6.1 summarizes its main parameters.

The first calculation from the data in the table is the RF wavelength and its relationship to the iris separation d: $\lambda_{\mathrm{RF}} = 0.105$ m, $\lambda_{\mathrm{RF}}/d = 3$. This last result reflects the $2\pi/3$ operating mode of the cavity (see figure 5.1), or, equivalently, the 120° phase advance between cells. The number of cavities is 86, which is close to L/d. Further, and as discussed in chapter 5, the tapered construction of the cavity geometry (gradual reduction in $2a$ and $2b$—see figure 5.1) guarantees that the peak accelerating field is constant, i.e. that the structure has a constant gradient. The variation of the group velocity along the 3 m structure can be calculated using equation (5.1.7): $v_g(0) = 0.018\mathrm{c}$, and $v_g(L) = 0.006\mathrm{c}$. The *filling time* is $t_{\mathrm{F}} = 2\tau Q/\omega_{\mathrm{RF}} \approx 1$ μs.

The energy gradient can be calculated using equation (5.1.8); we obtain 62.0 MeV over 3.05 m, i.e. 20.3 MeV m^{-1}. The RF peak power of the original design, 8 MW, leads to a gradient equal to 9.73 MeV m^{-1}. Finally, the energy at the end of a 3 km linac comprising the 3 m sections would be equal to 61 GeV. The actual linac uses 960, 3 m structures.

The second example of a linac is a proton machine at Los Alamos. Table 6.2 contains parameters of the LEDA proton linac collected from publications related to experiments on beam halo conducted around 2001 (see [8]). The proton beam is initially accelerated and focused by an 8 m, 350 MHz RF quadrupole (RFQ—see [15]) and matched with the first 4 quadrupoles into an 11 m strong focusing lattice. Several beam diagnostics allow measurements of beam profiles and emittances under different matching conditions.

Envelope mismatch is a major factor that contributes to halo formation. As seen at the end of section 6.1, the envelope of a mismatched beam undergoes symmetric

Table 6.2. Main parameters of LEDA halo experiment at Los Alamos.

Energy, E	6.7 MeV
Particle	Proton
Total Length, L	11 m
Lattice Period, S	0.42 m
Beam Current, I_b	<75 mA, CW
Emittance (rms, unnorm.), $\tilde{\varepsilon}_{\text{un.}}$	>3.0 µm
Undep. Phase Advance, σ_0	80°
Phase Adv. Depression, $\sigma/\sigma_0 = \eta$	0.82–0.95
RMS-Matched Beam Radius, a	>1.1 mm

(‘breathing’) and antisymmetric (‘quadrupole’) envelope modes. These modes can resonate with particles in the core of the beam expelling the particles to a maximum radius that depends on the degree of mismatch and the size of the core. We use data in the table to verify the quoted ‘tune’ depression η, effective beam radius with and without space charge (a, a_0), and the number of envelope mode oscillations over the length of the beamline. We find $\eta = \sigma/\sigma_0 = 0.97$, and $(a_0, a) = (1.90, 1.93)$ mm, from equations in section 4.3. Thus, beam transport in the halo experiments at LEDA was emittance dominated, but space charge effects were appreciable, much more than in electron linacs after acceleration. The values for ‘tune’ depression in the table are smaller but not too different from our result. Further, the effective matched beam radii (see K–V distribution in chapter 4) must be divided by 2 to obtain the rms value; thus we have $(a_{\text{rms}}, a_{0\text{rms}}) = (0.95, 0.97)$ mm, only about 10% smaller than the value in the last row of table 6.2.

To compute the number of envelope oscillations over 11 m, we first find the phase advances per period for the symmetric and anti-symmetric modes. From equations (6.1.4) and a 0.97 ‘tune’ depression, we obtain $(\sigma_{\text{sym}}, \sigma_{\text{asym}}) = (157°, 156°)$; from the wavenumbers $k_{\text{sym}} = \sigma_{\text{sym}}/S$, and $k_{\text{asym}} = \sigma_{\text{asym}}/S$ we get $L/\lambda_{\text{sym}} = 11.4$ oscillations, and $L/\lambda_{\text{asym}} = 11.3$ oscillations. The original paper (see [8]) reports ‘about ten mismatch oscillations’.

In conclusion, the K–V distribution and smooth-approximation models yield good results even when applied to emittance-dominated beam transport problems as in the LEDA experiments.

6.4 Examples of rings

We present here three examples of ‘circular’ accelerators or rings, two of which are synchrotron radiation (SR) sources (chapter 5): 1) the first generation (ca 1970), *weak-focusing* machine, SURF II (Synchrotron Ultraviolet Radiation Facility) at NIST in Gaithersburg, MD in the US, which is not exactly a ‘ring’; 2) one of the first second generation light sources (1982), the double-bend achromat (DBA) storage ring NSLS VUV (National Synchrotron Light Source) at Brookhaven National Laboratory (BNL) in Upton, NY; and 3) the room-size University of Maryland Electron Ring (UMER), which is a very-low energy, high current machine built

Table 6.3. SURF II parameters.

Energy, E	0.30 GeV
Super-Period, N	1
Bending Radius, ρ	0.837 m
Betatron Horizontal Tune, ν_{0X}	0.640
Vertical Betatron Tune, ν_{0Y}	0.768
Momentum Compaction, α	2.44
Emittance (natural), ε	0.350 μm
Natural Hor. Chromaticity, ξ_X	−1.79
Natural Vert. Chromaticity, ξ_Y	1.49
Transition Gamma, $\gamma_{\rm tr}$	0.640

around 2000 and located at the Institute for Research in Electronics and Applied Physics (IREAP), University of Maryland, College Park, MD.

Table 6.3 summarizes the parameters of SURF II. The SURF II lattice is one of the examples in the code Winagile (see appendix), and a MAD input file and additional information can be found in Jim Murphy's Data Book [9]. Further, a working MAD-8 input file for SURF II (SURFII.MAD) can be found in the book's website. In these files, the single bending magnet of SURF II is modeled with eight 45° sector magnets. The numbers for the tunes and chromaticity in table 6.3 can be extracted from the Winagile or MAD-8 files, but it is instructive to derive some of them from available relations. First, the *field index n* (chapter 2) can be deduced to be $n = 0.595$; this follows from equation (2.4.5) and the fact that the focusing constant ('K1' in MAD-8) $\kappa = 0.8496\ \text{m}^{-2}$ applies to the vertical plane. The betatron tunes are then obtained from equations (2.4.7) and (2.4.8); naturally for a weak focusing machine, the betatron tunes are less than 1.0. The momentum compaction factor and transition gamma are found from equations (3.6.4) and (3.6.6). The betatron function and dispersion values (not shown in the table) as well as the chromaticity can also be found from equations in chapter 3. Finally, the *natural emittance* in μm can be found from equation (5.3.17) after adapting the result to a weak focusing machine (see [9], p 41):

$$\varepsilon[\mu\text{m}] = \frac{C_q\gamma^2}{n\sqrt{1-n}}, \qquad C_q = 3.83 \times 10^{-13}\ \text{m}. \tag{6.4.1}$$

Important additional calculations pertain to the SR that can be produced with SURF II. First of all, note from table 6.3 and equation (5.3.4) the scaling of the radiated power per electron; SURF II has a very small radius but also low energy relative to other SR sources. Furthermore, the synchrotron radiation from SURF II has a continuous spectrum with a *critical energy* (chapter 5) given by equation (5.4.1). We obtain $E_{\rm cr} = 0.072$ keV, or a critical wavelength (h = Planck's const.) $\lambda_{\rm cr} = hc./E_{\rm cr} = 17$ nm, which is outside the 'water window' between 2.34 and 4.4 nm. The total radiated power per electron is, from equation (5.3.4), $P_{\rm R} = 7.9$ nW.

Table 6.4. Main parameters of the second-generation light source NSLS VUV.

Energy, E	0.808 GeV
Super-Period, N	4
Circumference	51.02 m
Horizontal Betatron Tune, ν_{0X}	3.123
Vertical Betatron Tune, ν_{0Y}	1.178
Synchrotron Tune, ν_{0S}	0.0018
Momentum Compaction, α	0.0235
Equilibrium Hor. Emittance, ε_x	0.154 μm
Natural Hor. Chromaticity, ξ_X	−3.44
Natural Vert. Chromaticity, ξ_Y	−5.77
Transition Gamma, $\gamma_{\rm tr}$	6.52

Assuming a current of $I_{\rm B} = 100$ mA, we can calculate the number of electrons as $N_{\rm e} = 2\pi\rho I_{\rm B}/e\beta c = 1.1 \times 10^{10}$. Therefore, the total irradiated power is $P_{\rm T} = N_{\rm e}P_{\rm R} =$ 86 W. A good exercise for the reader is to repeat the calculations for SURF III, which has a higher energy (0.38 GeV) and adjustable field index n. The SURF III website http://physics.nist.gov/MajResFac/SURF/SURF/accjavan.html is a good guide. We now turn our attention to a strong-focusing ring.

Table 6.4 summarizes the parameters of NSLS VUV. The basic cell of LNLS is a double-bend achromat (DBA) or Chasman–Green lattice. It consists of two bending dipoles with a quadrupole doublet between them; sextupoles are also present for correcting the chromatic aberration of the quadrupoles. See [16] for more details about the DBA. Figure 6.6 illustrates the basic lattice of NSLS-VUV. The betatron tunes are greater than 1 as expected for a strong-focusing machine. The numbers in table 6.4 are taken from calculations with Winagile and MAD-8 and from the BNL website. We obtain the same tunes in Winagile and MAD-8, but the website quotes (3.14, 1.26); the chromaticities are from MAD-8. Figure 6.7 shows the graphical output from MAD-8.

Additional calculations on SR and damping are based on the SR integrals whose equations are presented in chapter 5. The results for these integrals are summarized in table 6.5; the values were extracted from the 'Synchrotron Radiation Data' feature in Winagile.

The default *total particle energy* in MAD-8 is 1.0 GeV, while Winagile uses 1.0 GeV as default for the *kinetic energy*. Naturally, total energy and kinetic energy are very close to each other for highly relativistic particles, but not identical. Furthermore, the strengths of magnets (e.g. 'K1' for quadrupoles in MAD-8, MADX, Elegant and other accelerator codes) are independent of energy as they are given as focusing constants. The radiation integrals, partition numbers and momentum compaction are likewise independent of energy, but other derived quantities such as energy loss per turn, energy spread, equilibrium emittance and damping times will depend very critically on energy and type of particle.

We use equation (5.3.8) to calculate the energy loss per turn; the total radiated power for a 1.0 A beam current at NSLS-VUV is then: 19.7 kW. Further, the *natural*

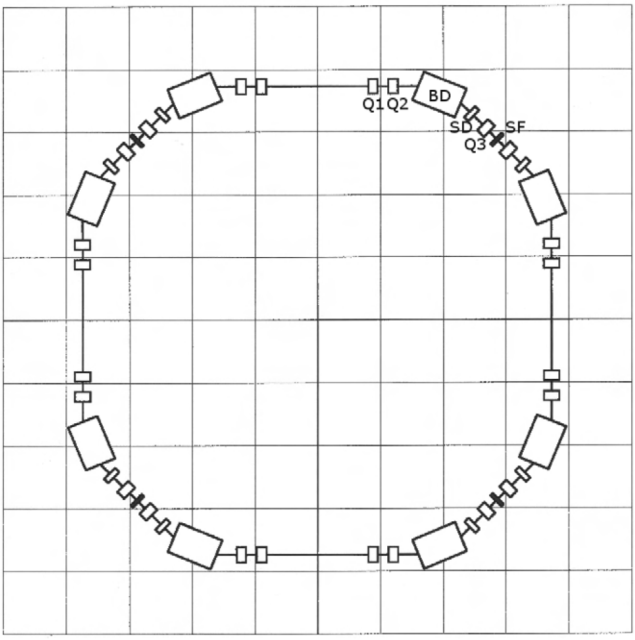

Figure 6.6. Lattice schematics of the second-generation light source NSLS VUV. The basic half-cell on the upper right is labelled: Q is quadrupole, BD bending dipole, SD, SF sextupoles. The grid size is 2.00 m. Adapted from Winagile code output.

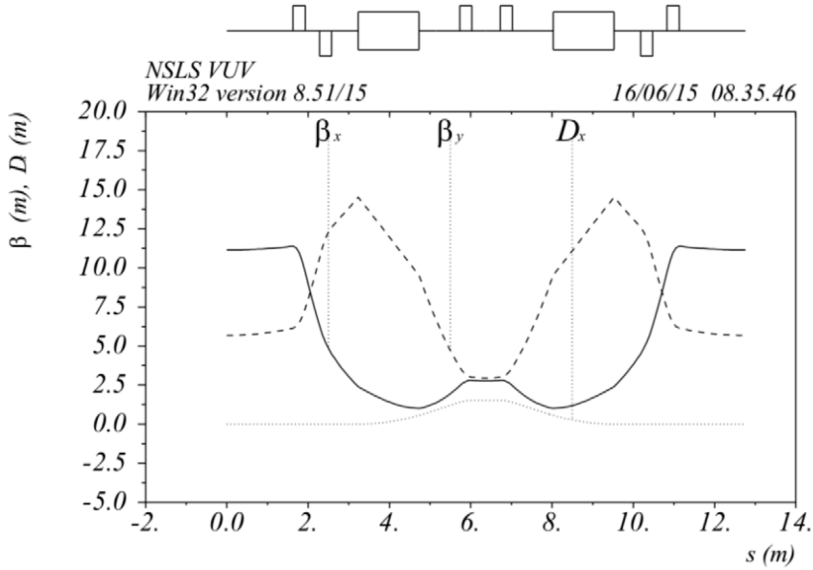

Figure 6.7. MAD-8 graphical output of lattice functions for NSLS-VUV. The magnet layout on top corresponds to a complete cell. The super-periodicity of the ring is $N = 4$.

Table 6.5. Synchrotron radiation integrals for NSLS-VUV (from Winagile).

I_1	1.199775 m
I_2	3.289868 m^{-1}
I_3	1.722571 m^{-2}
I_4	−0.246102 m^{-1}
I_5	0.567642 m^{-1}

Table 6.6. Main parameters of the University Of Maryland Electron Ring (UMER).

Energy, E	10 keV
Super-Period, N	1
Circumference	11.52 m
Beam Current, I_B	0.6 to 100 mA
Horizontal Betatron Tune, ν_{0X}	6.68
Vertical Betatron Tune, ν_{0Y}	6.85
Momentum Compaction, α	0.0214*
Tune Depression, ν/ν_{0X}	0.15 to 0.86
Coherent Tune Shift, $\Delta\nu_{coh}$	0.0036 to 0.61
Emittance (rms, norm.), $\tilde{\varepsilon}_n$	<3.2 μm
Natural Hor. Chromaticity, ξ_X	−7.31*
Natural Vert. Chromaticity, ξ_Y	−7.39*

* Elegant, with no space charge

energy spread and the *equilibrium horizontal emittance* are 5×10^{-4}, and 0.154 μm, respectively (see equations (5.3.17)). To find the damping times we need the bending radius ρ from the dipoles. We get ρ from the parameter sheet found at the NSLS-VUV website http://www0.bnl.gov/ps/nsls/facility/accelerator/vuv/; the magnetic rigidity is quoted there as $B\rho = 1.41$ Tesla × 1.91 m. Therefore, the damping times are (see equations in chapter 5) $\tau_x = \tau_y = 13$ ms, and $\tau_\varepsilon = 7.2$ ms.

Table 6.6 summarizes the parameters of the University of Maryland Electron Ring (UMER) relevant to our discussion; the UMER lattice schematics are shown in figure 6.8. The betatron tunes are determined experimentally (see [10]) For comparison, a simple-minded matrix calculation without bending dipoles yields equal bare tunes $\nu_{0X} = \nu_{0Y} = 6.83$ (equations (3.2.6), (3.2.7)). If the bending dipoles are included with edge effects, we obtain (Elegant—see files in appendix) $\nu_{0X} = 6.82$, $\nu_{0Y} = 6.88$. These edge effects include not only the standard vertical edge focusing from the rectangular bending magnets (see chapter 3) but also the field variation at the fringes. An additional effect from the Earth's magnetic field in the low-energy UMER can be modeled in Elegant but becomes problematic in other codes such as Winagile. Essentially, the *reference orbit* is determined in all rings by the bending and steering elements, but in UMER the bending dipoles are powered down because the Earth's magnetic field provides about 1/3 of the bending (!). Thus, the correct model must somehow keep the reference orbit for 36, 10° bending dipoles, while

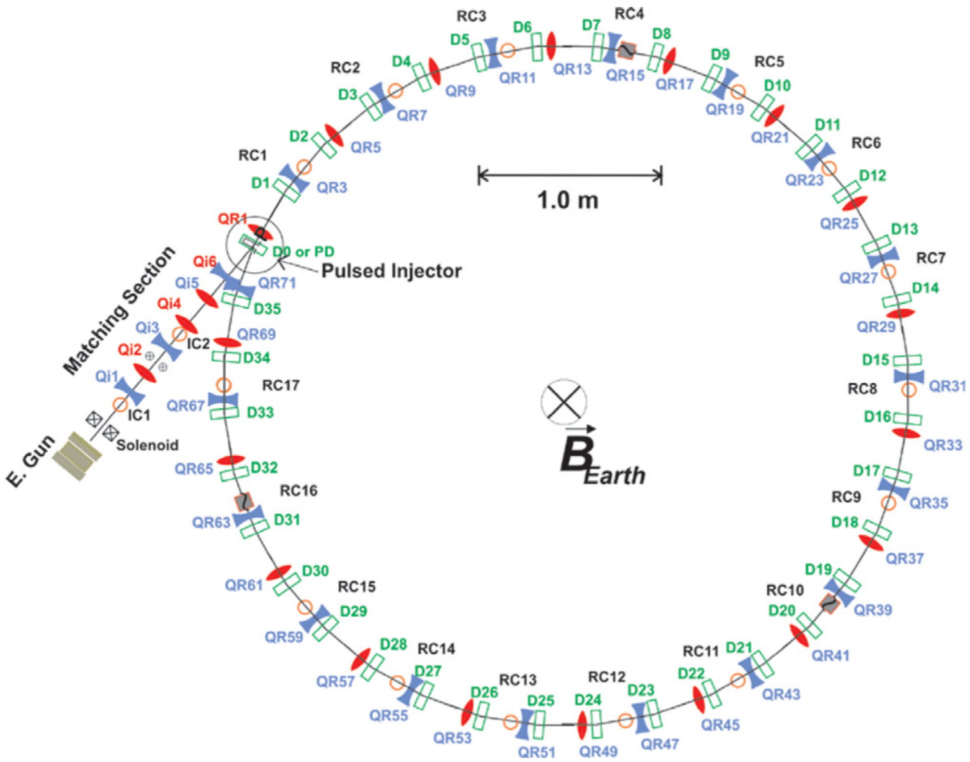

Figure 6.8. Schematics of University of Maryland Electron Ring (UMER). This low-energy, high-current machine has a high density of short printed-circuit quadrupoles. A typical bunch is 5 m long. Reproduced with permission from [11]. Copyright 2016, AIP Publishing LLC.

using actual 7°, approximately, dipoles. This is accomplished in Elegant through the FSE (field strength error) parameter.

The most interesting calculations in UMER relate to the effects of incoherent and coherent space charge (SC). We limit our brief discussion here to transverse dynamics effects, although longitudinal space-charge phenomena also play a significant role in UMER. At the lowest beam current, 0.6 mA, beam transport in UMER is *emittance-dominated*, although the fractional incoherent SC tune shift, equation (4.4.4), is sizable, about 14%. The corresponding SC tune depression is $\nu/\nu_{0X} = 0.86$. At the other end of the beam current range, 100 mA, we obtain a fractional incoherent SC tune shift of 85% (!) or a SC tune depression of $\nu/\nu_{0X} = 0.15$. UMER operates most of the time, however, with 6.0 mA beam current; the tune depression in this case is $\nu/\nu_{0X} = 0.64$, strongly SC dominated transport.

The *coherent tune shift* caused by image forces is also appreciable in UMER, despite the low-energy. We use equation (4.5.3) for the case of non-penetrating fields (see [4]). We obtain $\Delta\nu_{\text{coh}} = 0.0036$ for 0.6 mA, and 0.61 for 100 mA; at the typical 6.0 mA operating current, $\Delta\nu_{\text{coh}} = 0.035$. The contributions from the term

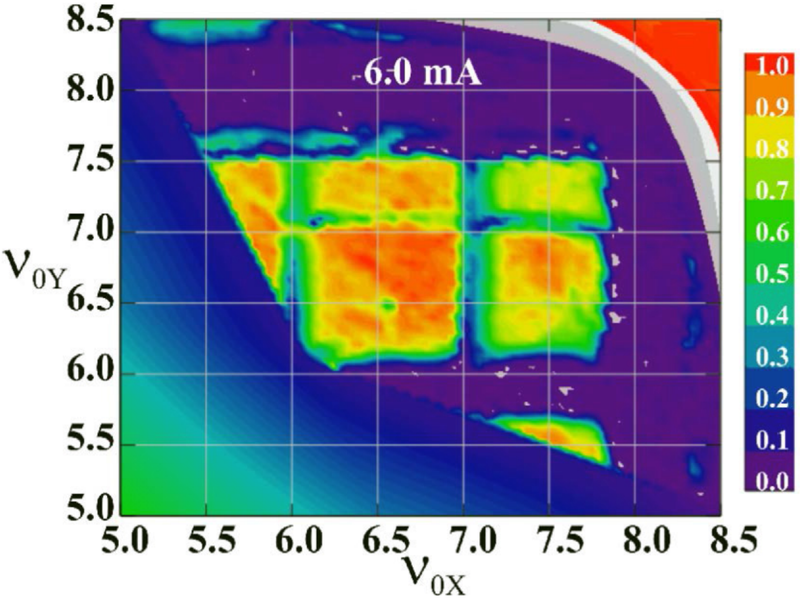

Figure 6.9. Beam lifetime chart at 10th turn as a function of estimated bare tunes (x: horizontal, y: vertical) for 6 mA, 10 keV beam in UMER. Red indicates *complete* beam transmission while purple indicates *zero* transmission. The green and red areas on opposite corners are artifacts of the graphics. From [10]. Used under CC-BY 3.0, http://creativecommons.org/licenses/by/3.0/deed.en_US

proportional to β^2 in equation (4.5.3) are small, of the order of 1% for 0.6 mA and negligible for higher beam currents.

The effect of the coherent tune shift for the 6.0 mA can be seen in resonance experiments in UMER (see [10]). In figure 6.9, we see the bands for linear resonances as well as the sum resonance $\nu_{0X} + \nu_{0Y} = 13$.

Calculations with SC in the context of the K–V envelope equations (chapter 4), i.e. with the assumption of linear SC can be done with K–V envelope or matrix codes (see appendix). We have already presented results of RMS envelope matching with strong SC in section 6.1; the parameters correspond to UMER's 10 keV, 100 mA beam. It is also possible to use a simple SC model in the code Elegant which yields good results up to about 6 mA in UMER for envelope, dispersion, emittance and other calculations (see [12]).

Computer resources

The computer codes MENV and SPOT for RMS envelope matching including SC, as well as the specification files of the examples presented in section 6.1, are available in the book's website. The appendix contains a brief description of these codes. In addition, TRACE2D and TRACE3D, freely available from Los Alamos (see appendix for hyperlink) are also very useful. Calculations related to integer resonances (section 6.2) are presented in the Mathcad worksheet **IntegerResonance.xmcd**. Two movies, **IntRes_Movie-I.avi**, and **IntRes_Movie-II.avi,** demonstrate the destructive effects of dipole and quadrupole errors in UMER.

The basic numerical calculations for the linacs and rings discussed are summarized in Mathcad worksheets, **SLAC-3m.xmcd, LEDA.xmcd**, **SURF II.xmcd, NSLS-VUV.xmcd, UMER-TuneShift.xmcd.** These files can be downloaded from the book's website. Also available in the website are the MAD8 and Winagile input files for SURF II and UMER.

Finally, the Android application TAPAS (see appendix) provides an instructive tool for synchrotron radiation calculations from bending magnets, storage rings and insertion devices.

References

[1] Bryant P J and Johnsen K 1993 *The Principles of Circular Accelerators and Storage Rings* (Cambridge: Cambridge University Press)

[2] Bernal S *et al* 2006 RMS envelope matching of electron beams from 'zero' current to extreme space charge in a fixed lattice of short magnets *Phys. Rev. ST Accel. Beams* **9** 064202

[3] Reiser M 2008 *Theory and Design of Charged Particle Beams* 2nd edn (New York: Wiley)

[4] Sutter D F, Cornacchia M, Bernal S, Beaudoin B, Kishek R A, Koeth T and O'Shea P G 2011 Current dependent tune shifts in the University of Maryland Electron Ring UMER *Proc. 2011 Particle Accelerator Conf.* (New York) p 1668

[5] Wille K 2000 *The Physics of Particle Accelerators, An Introduction* (New York: Oxford University Press) section 3.14.3

[6] Edwards D A and Syphers M J 2004 *An Introduction to the Physics of High Energy Accelerators* (New York: Wiley)

[7] Guignard G 1978 A general treatment of resonances in accelerators *CERN report CERN* 79–11

[8] Allen C K *et al* 2002 Beam-halo measurements in high-current proton beams *Phys. Rev. Lett.* **89** 214802

[9] Murphy J 1993 Synchrotron light source data book, Version 3.0, October 1993, Brookhaven National Lab., BNL 42333 (revised) Informal Report.

[10] Bernal S, Beaudoin B, Cornacchia M and Sutter D 2013 Stability of emittance vs. space-charge dominated beams in an electron recirculator *Proc. of PAC2013 (Pasadena, CA) TUPAC31*

[11] Bernal S *et al* 2015 Nonlinear dynamics with space-charge in a small electron recirculator *Proc. of the 16th Advanced Accelerator Concepts Workshop, AIP Conf. Proc*. at press

[12] Bernal S, Beaudoin B, Koeth T and O'Shea P G 2011 Smooth approximation model of dispersion with strong space charge for continuous beams *Phys. Rev. ST Accel. Beams* **14** 104202

[13] Le Duff J 1979 Integer resonance crossing in H.I. Accumulator Ring *Proc. of the Heavy-Ion Fusion Workshop* (*Berkeley, CA, 29 October–9 November 1979*) p 310

[14] Wiedemann H 2007 *Particle Accelerator Physics* 3rd edn (Berlin: Springer) chapter 13

[15] Wangler T P 2008 *RF Linear Accelerators* 2nd edn (Weinheim: Wiley)

[16] Winick H (ed) *Synchrotron Radiation Sources—A Primer* (Singapore: World Scientific) (the article 'Lattices' by Max Cornacchia is especially recommended)

A Practical Introduction to Beam Physics and Particle Accelerators

Santiago Bernal

Appendix

Computer resources and their use

Instead of having end-of-chapter problems and exercises, this book includes a section on 'Computer Resources' for each chapter. Therefore, the exploration and pace of learning does not depend on completing a minimum number of problems. Instead, the reader is free to explore the available resources, and only he or she can decide when the math, the physics and the software all come together to the point of 'understanding', before moving on to the next chapter.

Computer software has been an integral part of learning any technical or scientific field, particularly since the popularization of personal computers almost forty years ago. We can use software of three general types: low-level and high-level programming codes, and specific application software. We do not cover here (except for a very brief description of Python) the use of popular languages like C++, Python or Java. Python, in particular, is very popular for writing input files and scripts in several particle-accelerator codes. The names of some codes (e.g. JMAD and PyOrbit) reveal their dependence on Java or Python. Furthermore, Java is the basis for many 'applets' available online as educational tools in many areas.

We advocate in this book the use of Mathcad and Matlab or their freeware counterparts Smath Studio and Octave for general calculations and programming, with no prejudice towards the powerful Mathematica which we think is superior to the rest for symbolic calculations. (Besides Mathematica, Wolfram has created a stand-alone educational tool called 'CDF Player' that is essentially a read-only Mathematica. A large collection of CDF demonstration projects from Wolfram and third parties is freely available. CDF projects work in most cases better than Java applets of similar content). As for specific application software, we concentrate here on a number of popular codes for particle accelerator design and also on a few general optics programs (mostly for chapters 1 and 2). One area which we do not cover in the present edition of this book is magnet design; it is a highly specialized field for which many computer resources are also available.

doi:10.1088/978-1-6817-4076-8ch7

All particle accelerator codes described below, except for PBO Lab and some auxiliary software such as VMware Fusion, are freely available and can be installed in the most popular operating systems without any special difficulty. In particular, no compilation or any other gymnastics is necessary, other than running scripts to build packages or implementing the code in a virtual machine or emulation software (e.g. Wine under Ubuntu Linux) to get around compatibility issues. Furthermore, a few 'Apps' for Google's Android and Apple's IOS will be mentioned because of their instructional and 'fun' values.

In our opinion, the best approach to learning any of the codes is by example, and not by reading manuals. Manuals should be used only as references, and initially to check for general information such as sign conventions and important approximations (e.g. relativistic versus non-relativistic, symplectic versus non-symplectic, zero-current versus space-charge effects, etc).

The following steps may be a good guide towards learning not only the codes but also the physics: 1) open one of the example files provided and run the code to familiarize yourself with the basic GUI (or command-line) mechanics and capabilities; 2) edit the file to explore the scaling of different parameters; 3) do 'sanity' checks, i.e. back-of-the-envelope or Mathcad calculations to make sure the code is yielding expected results; 4) do your own concept design and either modify an existing file or start from scratch to implement your model in the code; 5) go back to 3); and 6) try a different code for cross-checking, or simply to compare programs and decide on which one to use. Regarding the last point, it is advisable to learn to be reasonably proficient in one code before switching to a different one. Naturally, there is no single code that can do everything that you will eventually need, so learning a (small!) number of codes may be a good idea. Exactly following the latter idea led to this book!

The tables below summarize the computer codes that are described in the following sections. Not all compatibility issues have been explored in depth, so it is possible that some of the codes can actually run in a particular OS despite the annotation '**×**'. The book's website provides example files for most codes.

A.0 Symplecticity

As discussed in the first section of chapter 4, Hamilton's equations of motion in classical mechanics lead to Liouville's theorem. This theorem asserts that the flow of representative points in phase space for systems without dissipation is similar to the flow of an incompressible fluid. In addition, the evolution of Hamiltonian systems can be described in terms of *canonical transformations* or, equivalently, *symplectic* matrices. The standard classical mechanics textbook by Goldstein [1] discusses these topics with clarity and detail in the chapter on canonical transformations. We only quote here the condition that a matrix $\boldsymbol{M}$ must satisfy in order to be symplectic, i.e. to represent a canonical transformation:

$$\boldsymbol{MJM}^T = \boldsymbol{J}, \qquad \text{or} \qquad \boldsymbol{M}^T\boldsymbol{JM} = \boldsymbol{J} \tag{A.1}$$

Table A.1. Code compatibility for particle accelerator programs used in the book.

	OPERATING SYSTEMS						
	Microsoft			Linux		Apple	
COMPUTER CODE ↓	Win 7-8	Win XP	Win XP, 7 + Cygwin	Ubuntu 14.04 LTS	Ubuntu 14.04 LTS + Wine	MAC OSX	MAC OSX + VMware Fusion[3], or Wine[4]
Elegant	×	×	✓	✓	×	✓	✓
SPOT[1]	×	✓	×	×	✓	×	✓
MENV[2]	✓	✓	×	✓	×	✓	✓
MAD-8	✓	✓		✓			
MAD-X	✓	✓		✓			
PART. BEAM 2007	✓	✓	×	×	✓	×	✓
PBO Lab	✓	✓	×	×		×	✓
TRACE2D	✓	✓	×	×	✓	×	✓
TRACE3D	✓	✓	×	×	✓	×	✓
Winagile	×	✓	×	×	✓	×	✓

[1] Originally written for Win 3.1
[2] MatLab program
[3] VMware Fusion + Ubuntu Linux or + WinXP
[4] Wine under Ubuntu Linux, or MacOS Wine.

Table A.2. Code compatibility for optics software and other packages used in the book.

	OPERATING SYSTEMS						
	Microsoft			Linux		Apple	
COMPUTER CODE or App ↓	Win 7-8	Win XP	Win XP, 7+ Cygwin	Ubuntu 14.04 LTS	Ubuntu 14.04 LTS + Wine	MAC OSX	MAC OSX + VMware Fusion
Optgeo	✓	✓	×	✓	×	✓	✓
2D Ray Tracer[1]	✓	✓	×	×	×	×	✓
Ray Optics				Android App			
RayLab				IOS App			
TAPAS				Android App			
Radiation2D	✓	✓	×	×	✓	×	✓
CDF Player	✓	✓	×	✓	×	✓	✓

[1] Mathcad program.

Table A.3. Computer code homepage or relevant website.

COMPUTER CODE↓	HOMEPAGE / WEBSITES
Elegant	http://www.aps.anl.gov/Accelerator_Systems_Division/Accelerator_Operations_Physics/software.shtml
SPOT	http://www.ipr.umd.edu/faculty/bernal
MENV	http://www.ipr.umd.edu/faculty/bernal
MAD-8	http://MAD-8.web.cern.ch/MAD-8/
MAD-X	http://mad.web.cern.ch/mad/ http://madx.web.cern.ch/madx/madx.old/
PART. BEAM 2007	http://uspas.fnal.gov/materials/materials-downloads.shtml
PBO Lab	http://www.ghga.com/accelsoft/
TRACE2D	http://laacg.lanl.gov/laacg/services/download_trace.phtml
TRACE3D	http://laacg.lanl.gov/laacg/services/download_trace.phtml
Winagile	http://www.isa.au.dk/accfys/E08/default.htm. http://espace.cern.ch/test-juas/documentation.aspx
Optgeo	http://jeanmarie.biansan.free.fr/optgeo.html
Ray Optics	https://play.google.com/store/apps/details?id=com.shakti.rayoptics&hl=en
2D Ray Tracer	http://www.physic.ut.ee/~kiisk/mcadapps/ Look for “RAYTRACE.ZIP”
RayLab	https://itunes.apple.com/us/app/raylab/id710190065?mt=8
TAPAS	https://play.google.com/store/apps/details?id=borland.TAPAs&hl=en
Radiation2D	http://www.shintakelab.com/en/enEducationalSoft.htm
CDF Player	http://www.wolfram.com/cdf-player/

where $\boldsymbol{J}$ is the antisymmetric matrix defined by

$$\boldsymbol{J} = \begin{bmatrix} \mathbf{0} & \mathbf{1} \\ -\mathbf{1} & \mathbf{0} \end{bmatrix}. \tag{A.2}$$

For a system with n degrees of freedom, the symbol $\mathbf{0}$ stands for a $n \times n$ matrix composed of zeros as elements, an $\mathbf{1}$ is a $n \times n$ unit matrix. In Hamiltonian mechanics $\boldsymbol{M}$ represents the $2n \times 2n$ *Jacobian* matrix of a canonical transformation. Using this language, Hamilton’s equations of motion for a system of n degrees of freedom are written as

$$\dot{\boldsymbol{\eta}} = \boldsymbol{J}\frac{\partial H}{\partial \boldsymbol{\eta}}, \tag{A.3}$$

with $\boldsymbol{\eta}$ representing a column vector with $2n$ elements: $\eta_i = q_{i,} \eta_{i+n} = p_i$ for $i \leqslant n$. H is the Hamiltonian, and the dot indicates time derivative. Equation (A.3) is shorthand notation for $2n$, first-order differential equations with a sign asymmetry between p and q equations.

Numerical methods involve transforming the initial state of the system over many successive time intervals. In general, however, these transformations are not symplectic and thus do not represent the evolution of a Hamiltonian system. For example, the simple first-order implicit or explicit numerical Euler methods (see any textbook on numerical methods) are not symplectic; even the standard fourth-order Runge–Kutta method, the workhorse of numerical work, is not symplectic. As a consequence, the use of these non-symplectic 'integrators' often yields unphysical results particularly for simulations over extended integration intervals (e.g. instabilities not seen in real accelerator experiments). Naturally, this is not acceptable for studies involving, for example, hundreds of thousands or millions of turns in circular accelerators, or simulations of the evolution of galactic systems over millions of years.

It is possible, however, to construct *symplectic integrators*. Numerical symplecticity not only yields the correct Liouvillian flow, but also prevents the numerical total energy from deviating monotonically from the correct conserved value. For example, a combination of implicit and explicit first-order Euler methods yields a first-order symplectic integrator. This case and other higher order methods are discussed in the context of the simple harmonic oscillator in an *American Journal of Physics* article by Dennis Donnelly and Edwin Rogers [2]. More general discussions of symplectic integrators can be found in an article by H Yoshida in the *Handbook of Accelerator Physics and Engineering* [3], and the books by Étienne Forest [4], or Andrzej Wolski [5].

Tracking through *thin* elements is symplectic; we can use the matrix for a thin lens, equation (1.1.5), and equation (A.1) above to prove it. Although symplectic tracking using *thick* elements is also possible, the computational speed of using thin elements is greater. We have included a simple Mathcad document, **Simplecticity.xmcd**, in the book's website, to display matrix calculations of thin and thick lenses to test symplecticity.

The MAD8 and MADX codes (see section A.5 below) have the command 'MAKETHIN' to turn thick elements into symplectic thin ones. In the code Elegant (see section A.3 below), non-symplectic sector magnets (SBEN) or quadrupoles (QUAD), or their symplectic counterparts CSBEND and KQUAD can be used. The canonical bend CSBEND, for example, is described in the Elegant manual as using the *exact* Hamiltonian, i.e. all orders of the momentum offset and curvature. This is particularly important for tracking in rings.

Non-Liouvillian processes such as the generation of synchrotron radiation are non-symplectic. Even in this case, tracking is best performed with symplectic integrators ignoring radiation. However, the use of all approximations, especially the *paraxial approximation*, must be checked, because it may yield larger errors than the ones originating from non-symplectic elements. This is particularly important for tracking in small rings.

A.1 Software and hardware

With usage of Microsoft Windows (all versions) versus Apple's Mac OSX (all versions) versus Linux (all flavors) running about 90% versus 8% versus 2% (early

2015), it is no wonder that software developers and vendors focus heavily on the Windows platform. Two obvious advantages of Windows domination come to mind: first, the most popular application's software is optimized for the most popular platform, and second, backwards compatibility is made more important for Windows. Thus, it is easy to run most Windows software that was developed 20 years ago or before; this backwards compatibility is facilitated by the existence of emulation programs and software for running virtual machines.

This book and the programs developed for it were written using software for MS Windows 7. Some programs were also tested in Mac OSX 10.10.1 (Yosemite) and Ubuntu Linux 14.04 LTS; the latter with and without the Windows emulation application Wine (also available for OSX). Wine was particularly useful for running old software written for MS Windows XP or 3.1 (see tables above). In addition, the VMware Player (freeware for Windows and Linux) and VMware Fusion (commercial software for Mac OSX) were also employed to implement virtual machines (e.g., Win 7 and Ubuntu on a Mac host, and Ubuntu, and Win XP on a PC host running Win 7). Although machines using the old Core 2 Duo Pentium processors or equivalent AMD processors, with at least 2 GB RAM, are good enough to run most software described here, very significant speed and compatibility are gained with machines employing Pentium i5 and i7, or equivalent AMD processors, and 4–8 GB RAM. We also tested some applications on iOS and Android mobile devices. The book's website contains additional information.

A.2 General tools: Mathcad, Matlab and Python

Mathcad is a self-documenting code for general calculations in math, science and engineering. The code is particularly appealing for those not willing to learn a programming language and interested in applications where speed is not a main factor. Mathcad, introduced in 1986 for DOS by MathSoft, is now owned by PTC. Mathcad is currently available for Microsoft Windows only, but can be run in MAC OSX or Linux through a Windows virtual machine. The current version of Mathcad is 15, but few users would see significant differences between that version and Mathcad 11 which was released over 10 years ago. PTC is currently supporting versions 14 and 15 and the related products Prime 2.0 and 3.0. Students can get Mathcad 15 for around $100; others can obtain a free trial version that will revert to Mathcad Express if the full license is not purchased by the end of the trial period. Mathcad Express will retain only the basic features of Mathcad. There is also a freeware alternative to Mathcad called SMath Studio, available for Windows and Linux. SMath Studio does not have all the functionality of Mathcad but it is a respectable 'clone'.

Almost all numerical examples quoted in the 'Computer Resources' sections of the book were written in Mathcad 14 and 15, but Mathcad 11 versions (and a few SMath Studio as well) are also available in the book's website. In figure A.1 we show a Mathcad document for the solution of the damped harmonic oscillator. We present equivalent examples in Matlab and Python below.

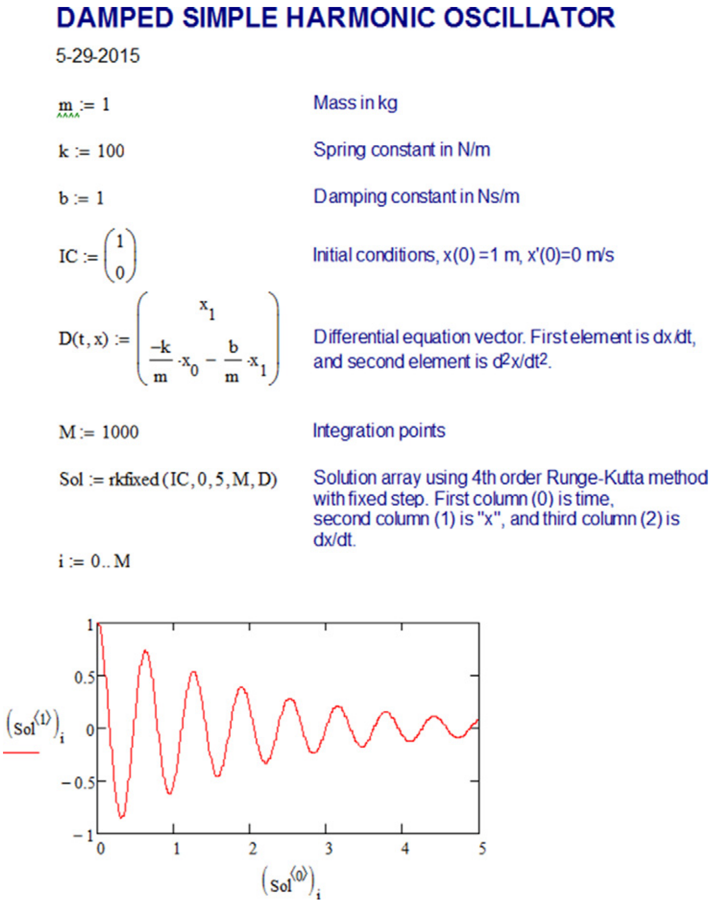

DAMPED SIMPLE HARMONIC OSCILLATOR

5-29-2015

$m := 1$	Mass in kg
$k := 100$	Spring constant in N/m
$b := 1$	Damping constant in Ns/m
$IC := \begin{pmatrix} 1 \\ 0 \end{pmatrix}$	Initial conditions, x(0) =1 m, x'(0)=0 m/s
$D(t,x) := \begin{pmatrix} x_1 \\ \frac{-k}{m}\cdot x_0 - \frac{b}{m}\cdot x_1 \end{pmatrix}$	Differential equation vector. First element is dx/dt, and second element is d2x/dt2.
$M := 1000$	Integration points
$Sol := \mathrm{rkfixed}(IC, 0, 5, M, D)$	Solution array using 4th order Runge-Kutta method with fixed step. First column (0) is time, second column (1) is "x", and third column (2) is dx/dt.
$i := 0..M$	

Figure A.1. Simple example of Mathcad document.

Matlab is possibly the most popular general computing tool for engineers, scientists and educators worldwide. It was initially developed in the 1970s and 1980s by Cleve Moler and others from the University of New Mexico and Stanford University. Matlab's name derives from 'Matrix Laboratory', as its original signature strength was, and still is, matrix calculations. Matlab is owned by MathWorks and is available for all major platforms. Several freeware Matlab 'clones' have appeared over the years, most notably Octave and Scilab, for various operating systems. Although not as transparent as Mathcad, Matlab's learning curve is well within the abilities of freshmen, and, as with many programming languages, can be learned faster through the use of existing sample programs or templates. In fact, many free as well as commercial packages or 'Toolboxes' for various applications (e.g., signal processing, image processing, data acquisition and control, etc) are available, including one for particle accelerators. The latter is called the 'Accelerator Toolbox' or just 'AT', and was introduced by Andrei Terebilo from SLAC in 2001.

Only to illustrate the use of Matlab, we present below a simple example and instructions for solving the damped harmonic oscillator. (Obviously, there is an analytical solution to this problem, and also multiple ways within Matlab of finding numerical solutions).

1) Write *and* save the '*M-file*' named `oscillator.m` (use the built-in script editor):

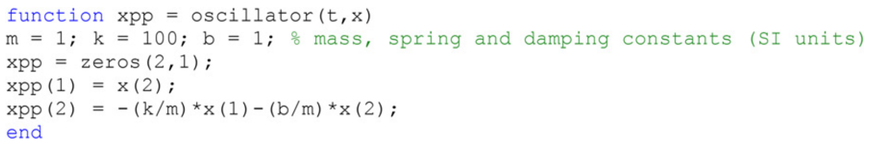

```
function xpp = oscillator(t,x)
m = 1; k = 100; b = 1; % mass, spring and damping constants (SI units)
xpp = zeros(2,1);
xpp(1) = x(2);
xpp(2) = -(k/m)*x(1)-(b/m)*x(2);
end
```

2) In *command* window run

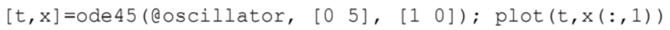

```
[t,x]=ode45(@oscillator, [0 5], [1 0]); plot(t,x(:,1))
```

to generate x versus t. Compare with Mathcad document in figure A.1 above.

We are in the process of translating some of the book Mathcad documents into Matlab (see book's website).

Python is an extremely popular general-purpose programming language. Python's syntax is very similar to Matlab's, and their speeds are also comparable, as both are interpreted languages. Python's trademarks are clarity and simplicity; it is highly readable and extensible, with a large body of numerical and scientific libraries or packages. Python is freely available for all major platforms. Some implementations, such as Anaconda, come with an excellent editor (Spyder) and all major scientific packages (e.g., `numpy`, `matplotlib`, `simpy`). Guido van Rossum from the Netherlands started Python in 1989. Python 2.0 was released in 2000, and Python 3.0 in 2008. Python 2.7 is run by default in Ubuntu Linux 14.04, but Python 3.4 is also installed; when running the latter, the command 'python3' is used instead of just 'python'. With these versions, it is possible to run any of thousands of programs available mostly in websites associated with computer and physics courses at universities worldwide. Using these programs is also a good way to learn Python by example. In addition, a visual Python is available to facilitate the graphical simulation of simple and some complex physical systems.

To conclude this section, we show a simple Python program to solve the damped simple harmonic oscillator. A key difference between Python and other languages is that *indenting* in Python is crucial. Compare the Python script below with Matlab's version. Note that in Python, unlike Matlab, there is no need to do two operations to run the code (the *M-file* plus the command instruction). Another important difference is that indexing of arrays starts at 0 in Python and 1 in Matlab. In Mathcad, the start index is 0 by default, but can be changed to 1 by typing ORIGIN:=1.

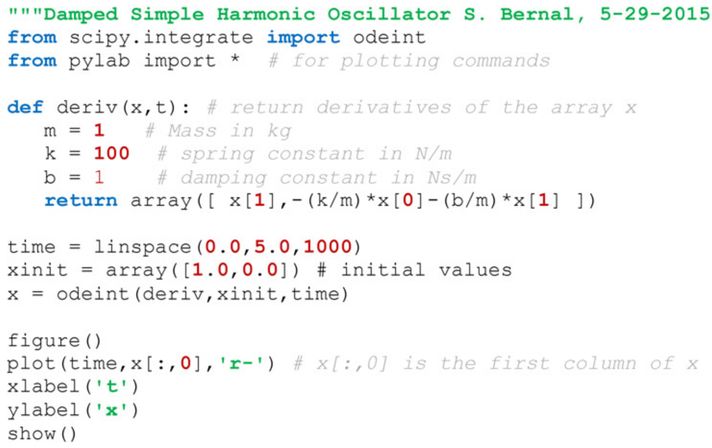

```
"""Damped Simple Harmonic Oscillator S. Bernal, 5-29-2015"""
from scipy.integrate import odeint
from pylab import *  # for plotting commands

def deriv(x,t): # return derivatives of the array x
   m = 1    # Mass in kg
   k = 100  # spring constant in N/m
   b = 1    # damping constant in Ns/m
   return array([ x[1],-(k/m)*x[0]-(b/m)*x[1] ])

time = linspace(0.0,5.0,1000)
xinit = array([1.0,0.0]) # initial values
x = odeint(deriv,xinit,time)

figure()
plot(time,x[:,0],'r-') # x[:,0] is the first column of x
xlabel('t')
ylabel('x')
show()
```

Other general software can be employed to model and do design calculations for accelerators. For example, Microsoft Excel has been used by Dr David Douglas *et al* at Jefferson Lab in Virginia [6] to do basic linear optics modeling of the free electron laser driver.

A.3 Elegant

Elegant is a powerful third-order matrix code widely used to model light sources and other accelerators, from the Advanced Photon Source (APS at Argonne National Lab) to x-ray FELs such as the Linac Coherent Light Source, LCLS, at Stanford National Lab. Elegant was started by Michael Borland from APS in 1988, and is maintained by him and others at APS and elsewhere [7, 8]. There is also the 'Elegant forum' where users can almost always find solutions to code or model-related problems. The code is freely available from the APS website for all major platforms, but you will need to register with your e-mail to get a key to download the files and documents (Elegant, SDDS, examples, and manuals).

DOWNLOAD: You can download all the files from the APS website. See table A.3.

INSTALLATION: For the Windows installation, you will need to first install CYGWIN and MS Visual C++. Follow the steps in the APS website. Installation in Ubuntu Linux is relatively straightforward; we recommend building the 'rpm' packages using the script in Step 1 instead of trying the pre-built RPMs. Details and corrections not covered in the APS instructions can be found in the book's website. The instructions for the Mac latest OSX (10.10.1—Yosemite—at the time of writing, February 2015) are not current in the forum. The best route is to download the binary OSX executables for both SDDS and Elegant (darwing-x86 compressed folders). Additional instructions can be found in the book's website.

RUN/EXAMPLE: the main files in Elegant are the Elegant *input* file with extension '.ele' and the *lattice* file with extension '.lte'. These files can be edited with any text editor such as WordPad in Windows, 'gedit' in Linux, or TextEdit in the Mac. Below is an example of a *lattice file*, ‘umer1.lte’, corresponding to the University of Maryland Electron Ring (UMER):

```
!umer1.lte
!Simple Example from UMER

DR1: DRIF,L=0.05418
QD1: QUAD,L=0.05164,K1=-153.419
DR2: DRIF,L=0.03538
DIP1:
SBEND,L=0.0376,ANGLE=0.1745329252,E1=0.0872664626,E2=0.0872664626,
HGAP=0.0287,FINT=0.3,&
FSE=-0.0
DR3: DRIF,L=0.03538
QF1: QUAD,L=0.05164,K1=153.419
DR4: DRIF,L=0.05418
DR5: DRIF,L=0.05418
QD2: QUAD,L=0.05164,K1=-153.419
DR6: DRIF,L=0.03538
DIP2:
SBEND,L=0.0376,ANGLE=0.1745329252,E1=0.0872664626,E2=0.0872664626,
HGAP=0.0287,FINT=0.3,&
FSE=-0.0
DR7: DRIF,L=0.03538
QF2: QUAD,L=0.05164,K1=153.419
DR8: DRIF,L=0.05418

!Define Beamlines

FODO1: LINE=(DR1,QD1,DR2,DIP1,DR3,QF1,DR4)
FODO2: LINE=(DR5,QD2,DR6,DIP2,DR7,QF2,DR8)
SECTION: LINE=(FODO1,FODO2)
RING: LINE=(18*SECTION)
```

The notation and structure of this file is similar to those of files used in the MAD codes (A.5 below). UMER consists of 18 sections, each having two FODO periods. There are two bend dipoles and 4 quadrupoles per section (see figure 6.8 and section 6.4 for additional details). K1 represents the quadrupole focusing constant κ_0 in m^{-2}; the bend dipoles are rectangular 10^0 bend magnets (two 5^0 edge angles E1 and E2), and FINT is a constant (‘field integral’) that is introduced to implement edge effects (see TRANSPORT manual [12] for definition). Note that ‘!’ must precede comments. The Elegant manual describes in detail a large number of accelerator lattice elements and their parameters.

The Elegant input file is ‘umer1.ele’:

```
!umer1.ele

   !Simple Example from UMER

   &divide_elements
      maximum_length=0.002
      name = *
   &end

   &run_setup
   lattice = umer1.lte
   default_order = 3
```

```
          rootname = umer1
       use_beamline = "ring"
       output = %s.out
          sigma = %s.sig
       p_central = 0.199
       final = %s.fin
       magnets = %s.mag
    &end

    &run_control
       n_steps = 1
       n_passes=5
    &end

    &twiss_output
       matched = 1,
       beta_x = 3.119e-1,
       alpha_x = 1.324,
       beta_y = 3.090e-1,
       alpha_y = -1.315,
       eta_x = 0.0,
       etap_x = 0.0,
       eta_y = 0,
       etap_y = 0,
       filename = %s.twi
    &end

    !&bunched_beam
       bunch = %s.bun
       n_particles_per_bunch = 10000,
       emit_x = 8.048e-6,
       emit_y = 8.048e-6,
       beta_x = 3.119e-1,
       alpha_x = 1.324,
       beta_y = 3.090e-1,
       alpha_y = -1.315,
       eta_x = 0.0,
       etap_x = 0.0,
       eta_y = 0,
       etap_y = 0,
       use_twiss_command_values = 0,
       Po = 0.199,

   sigma_dp = 0.01,
   sigma_s = 1.69,
   distribution_cutoff[0] = 2.5
   distribution_cutoff[1] = 2.5
   distribution_cutoff[2] = 1.73
   distribution_type[0] = "gaussian"
   distribution_type[1] = "gaussian"
   distribution_type[2] = "hard-edge"
   save_initial_coordinates =1;
!&end

!&track &end

&save_lattice filename = %s.new
   output_seq = 1
&end

&stop   &end
```

Notice that the ‘umer1.ele’ file above is divided into blocks that begin with ‘&name of block’ and end in ‘&end’. For example, we have ‘&run_setup’, ‘&twiss_output’, ‘&run_control’, ‘&bunched_beam’, ‘&track’, and others. The elements of all available blocks are explained in detail in the Elegant manual. Notice how the lattice file and the beamline are called in the ‘&run_setup’ block. Also, an entire block can be commented out by using ‘!’, as is the case with the ‘&bunched_beam’ block above.

The code is run by typing

```
elegant umer1.ele
```

In the example above, the code finds the matched lattice functions `Betax, Betay, Etax` and `Etay`, i.e., the transverse betatron and dispersion functions. To plot `Betax`, for example, type

```
sddsplot umer1.twi -col=s,betax
```

Notice the command ‘sddsplot’; it is part of the SDDS tools, an important component of Elegant. To print the betatron tunes one would type

```
sddsprintout umer1.twi -par={nux,nuy}
```

In order to track and plot *beam* functions, as opposed to *lattice* functions, we need the ‘&bunched_beam’ block in the ‘.ele’ file. Thus, we specify the initial beam parameters, distribution types in x,y,z and number of particles (10000 in the example). As an example, we type

```
sddsplot umer1.sig -col=s,Sy
```

to plot the rms envelope in the vertical plane as a function of the reference-orbit coordinate ‘s’. Figure A.2 below shows the output plots of Betax with use_beamline = “ring”, and use_beamline = “section” in the ‘&run_setup’ block.

Running Elegant and plotting lattice and beam functions and also doing complex operations can be made very convenient by writing SDDS scripts. For example, we can have a simple script, ‘simple_script.txt’ that will run ‘umer1.ele’, and display the

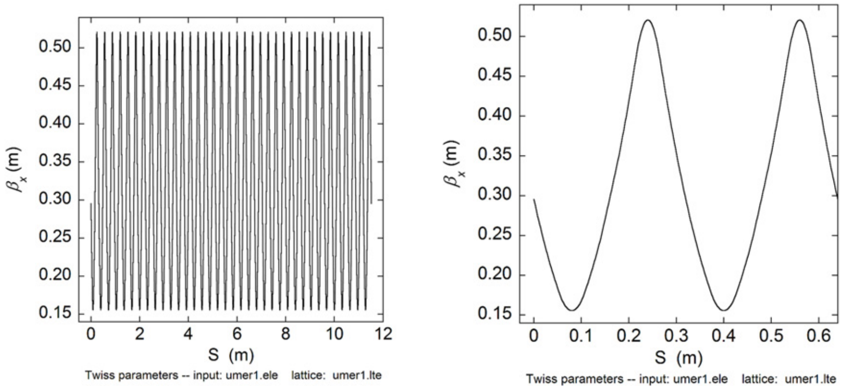

Figure A.2. Horizontal betatron functions calculated in Elegant: (left) one turn or 18 sections, and (right) one section of the University of Maryland Electron Ring (UMER).

betatron tunes, horizontal and vertical chromaticities, momentum compaction, and plot `Betax, Betay`:

```
sddsmakedataset settings.sdds \

elegant umer1.ele

sddsprintout umer1.twi -par={nux,nuy}
sddsprintout umer1.twi -par={dnux/dp,dnuy/dp}
sddsprintout umer1.twi -par=alphac
sddsplot umer1.twi -col=s,betax
sddsplot umer1.twi -col=s,betay
```

The script can be run by typing './simple_script' (no quotation marks) in MS Windows (under Cygwin), but the text file must be first converted to a Unix text file using the command 'd2u simple_script.txt'; 'd2u' stands for 'dos-to-unix'. Such conversion is not required in Linux or OSX. Finally, a very useful command in Elegant is 'sddsquery filename'; for example, 'sddsquery umer1.twi', 'sddsquery umer1.sig' will list all parameters that are part of the lattice and beam sets, respectively.

A.4 Envelope codes (SPOT and MENV)

The code SPOT solves the envelope equations, equations (4.4.10), for either a unit FODO cell or a general matching section. In the first case, the periodic envelope solution is found for given beam parameters (generalized perveance and edge emittances) and fixed quadrupole strengths corresponding to desired zero-current phase advances (section 6.1). These quadrupole strengths can be found from equations (3.2.6) and (3.2.7) for hard-edge gradient models. The other, more interesting, case of matching is the optimization of a nonperiodic envelope leading from the input plane at $s = s_i$ to the periodic envelope starting at $s = s_f$. A major feature of SPOT is the use of a *reference trajectory*. If the average values of the beam excursions X and Y are known, the reference trajectory or trajectories can be set to be equal to those constant values, except at the beginning of the matching section. With a specified reference trajectory and an initial guess for the strengths of the matching lenses, SPOT minimizes a functional, essentially the squared distance between the envelope solution and the reference trajectory. This functional can be extended to include the weighted beam target parameters, e.g., the beam transverse semi-axes and slopes at the terminal state. The optimizing techniques in SPOT utilize tools from nonlinear programming developed for control problems in engineering and mathematics. Additional details can be found in [14].

SPOT runs under MS Win 3.1 or Win XP, or through emulation software such as Wine (Linux and Mac OSX). Dr Hui Li, a former graduate student at University of Maryland, wrote a Matlab version of SPOT with a GUI and added functionality. The Matlab version is called MENV for 'Matlab Envelope'. The optimization in MENV uses tools from Matlab directly, which in some cases lead to solutions that converge more rapidly than in SPOT.

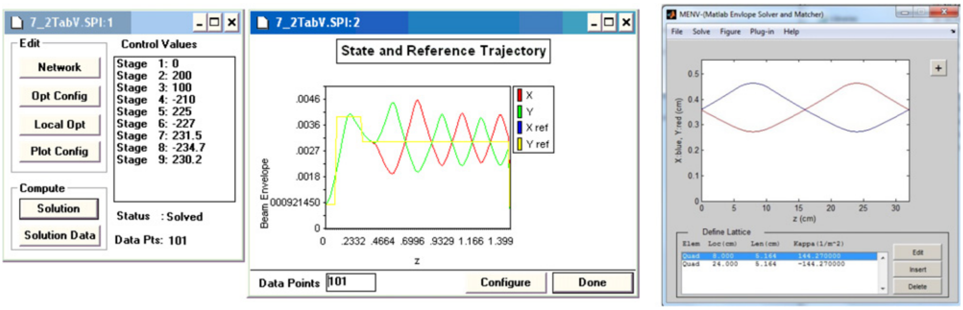

Control Values

Stage 1: 0
Stage 2: 200
Stage 3: 100
Stage 4: -210
Stage 5: 225
Stage 6: -227
Stage 7: 231.5
Stage 8: -234.7
Stage 9: 230.2

Status : Solved
Data Pts: 101

Data Points 101

Elem	Loc(cm)	Len(cm)	Kappa(1/m^2)
Quad	8.000	5.164	144.270000
Quad	24.000	5.164	-144.270000

Figure A.3. Working windows in envelope codes SPOT and MENV. The reference trajectory is shown in yellow for the non-periodic matching problem in SPOT (middle plot). The MENV window (right) displays an example of periodic envelope matching. The examples are from UMER. See [9, 14].

Typical working spaces for SPOT and MENV are shown in figure A.3. Both SPOT and MENV can be obtained through the book's website.

A.5 MAD-8 and MAD-X

The Methodical Accelerator Design (MAD) program has been used at CERN for over 20 years to simulate, design and optimize large linear and circular particle accelerators. A few major examples are the Proton Synchrotron (PS), the Super Proton Synchrotron (SPS), the Large Electron-Positron collider (LEP), and the Large Hadron Collider (LHC). The old version MAD-8 was 'retired' in 2002, but at least two versions are still available for download (see table A.3): 8.23.06 and 8.51/15 from SLAC and CERN.

MAD does not have a GUI, as it is more a *language* than a code. The User's manual [10] is a massive book, as for the old code TRANSPORT [12], with a plethora of physics and detailed explanation of all commands, syntax, etc but very little on how to actually run the code. On the other hand, there are a few very useful tutorial presentations available online. We have adapted an example from one of them [15] to use it with the latest (March, 2015) MAD-X release, version 5.02.04. We emphasize that we are only scratching the surface of a very powerful and complex program for single-particle simulations of accelerators. Space-charge effects can be simulated also, but in conjunction with another code called PTC. The CERN website has more details.

DOWNLOAD: To download MAD-8 or MAD-X use the hyperlinks on table A.3. For MAD-X click 'Releases' on the left list and then 'production releases repository'. For the Mac, click on 'development releases repository'.

INSTALLATION: for Windows, move the madx-win64.exe (64-bit Win) or madx-win32.exe (32-bit Win) file to a folder 'MAD-X'. Rename the file to simply 'madx.exe'.

RUN/EXAMPLE: the MAD-X language is not case sensitive. The file below, FODOUMER.MADX, is self-explanatory for the most part. A FODO unit cell for the UMER machine is defined, and the beta functions plotted for arbitrary initial values `BETX=0.9,BETY=0.7,ALFX=0,ALFY=0,` and then for *periodic* matched conditions ('cell matching' in the terminology of the MAD User's Reference Manual). Comments are preceded by //, /*, or !.

Notice that the energy 'PC' is in units GeV c^{-1} (very small for the 10 keV UMER!) Also notice that in our example the drift spaces and quadrupoles are subdivided into 10 slices to obtain smooth plots.

```
//FILE: FODOUMER.MADX
//MADX Example 1: FODO cell
//Author: S. Bernal, IREAP, U. of MD
//Date: March 2nd, 2015

BEAM, PARTICLE=ELECTRON,PC=10158E-06;

D: DRIFT,L=0.010836;
QF: QUADRUPOLE,L=0.005164/2,K1=168.36;
QD: QUADRUPOLE,L=0.005164/2,K1=-168.36;

FODO: LINE=(10*(QF),10*(D),10*(QD),10*(QD),10*(D),10*(QF));
USE, PERIOD=FODO;

TWISS,SAVE,BETX=0.9,BETY=0.7,ALFX=0,ALFY=0;
PLOT, HAXIS=S, VAXIS=BETX, BETY;

TWISS;
MATCH, SEQUENCE=FODO;
PLOT, HAXIS=S, VAXIS=BETX, BETY;
```

The program is run by typing

```
madx < FODOUMER.MADX
```

The output is in the form of the postscript file 'madx.ps' which can be opened with GhostView in Windows. In the example above, two plots (one per page) are generated. The plots are shown in figure A.4. Additional examples can be found in [13].

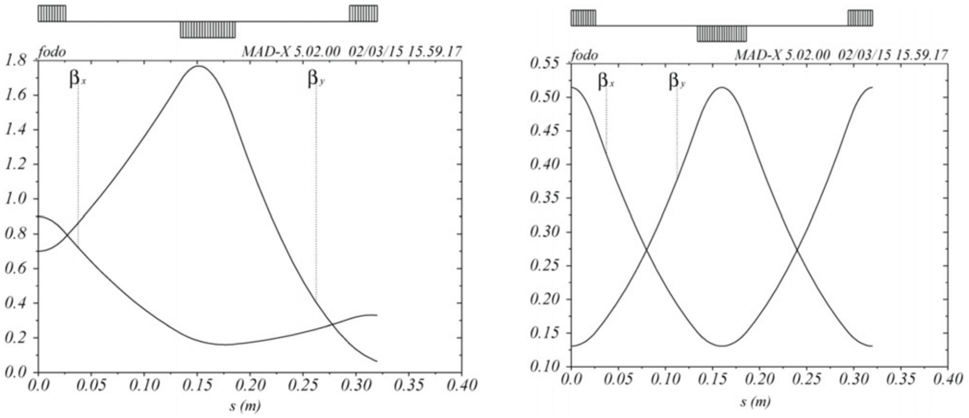

Figure A.4. Output plots from MAD-X: unmatched FODO cell (left), and matched FODO cell (right). Notice the diagram for the FODO cell on top.

A.6 Particle Beam 2007

This is a program written by Professor Helmut Wiedemann from Stanford University and employed at the US Particle Accelerator School (USPAS). The USPAS website (see link in table A.3) describes the program: '(it) lets the user design a beam transport line or a storage ring. The program calculates single particle trajectories, betatron functions, periodic betatron/dispersion functions (if there is a solution). After insertion of sextupole magnets it is possible to track particle trajectories, RF-parameters are calculated as well as beam lifetimes … Many graphs are available for particle trajectories, betatron functions, RF-phase space and tracking.'

Many examples of lattices are included (files with extension .LAT). When opened, the lattice functions are displayed. One very useful feature of the program is that the individual accelerator elements displayed at the bottom of the plots can be accessed by just clicking (as with PBO Lab—see below). In this way the user can examine the lattice in detail and introduce changes to find new solutions. The main functions of the program appear under the 'Optics' menu where matrix elements for one period can be selected for display, or trajectories and beam sizes calculated. In figure A.5 below we show an example using the SESAME.LAT file. The lattice functions and the parameters for a magnet are displayed.

A.7 PBO Lab

The Particle Beam Optics Laboratory is a product of AccelSoft Inc. of Del Mar, CA [16]. The trademarks of PBO Lab are its modular nature and a drag-and-drop GUI based on icons representing accelerator components. There are modules available for TRANSPORT, TRACE-3D, MARYLIE and others. The software is available for MS Windows only, although some of the old versions were available for the Mac. The learning curve is very fast, and there is a good built-in tutorial on basic accelerator physics. We have found that the TRACE module is particularly useful, as well as the included tools for trajectory tracking. Other modules are being developed, such as one for MAD-8.

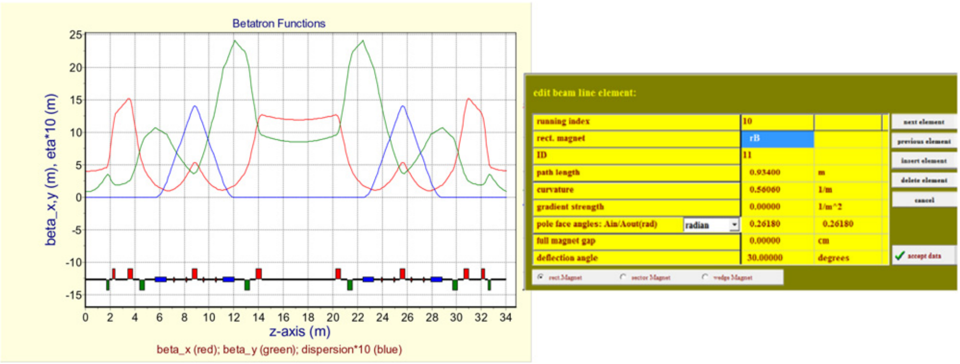

running index	10	
rect. magnet	rB	
ID	11	
path length	0.93400	m
curvature	0.56060	1/m
gradient strength	0.00000	1/m^2
pole face angles: Ain/Aout(rad) radian	0.26180	0.26180
full magnet gap	0.00000	cm
deflection angle	30.00000	degrees

Figure A.5. Particle Beam 2007 – Lattice functions for the SESAME light source (left), and parameters for rectangular magnet located at $z = 6$ m, approximately (right).

A.8 TRACE-2D and TRACE-3D

The best description of the TRACE programs comes from the abstract to the Trace 3D documentation [17]: ‘TRACE 3D is an interactive beam-dynamics program that calculates the envelopes of a bunched beam, including linear space-charge forces, through a user-defined transport system. TRACE 3D provides an immediate graphics display of the beam envelopes and phase-space ellipses, and accommodates fourteen different types of fitting or beam matching options’. The documentation includes several appendices with excellent concise discussion of basic topics such as the σ-matrix, Twiss parameters, mismatch factor and others. Furthermore, a summary of TRACE 2D commands is given in appendix K. TRACE 2D is used for unbunched, i.e., continuous or coasting beams.

DOWNLOAD: the codes are freely available from Los Alamos National Laboratory after a simple registration process. See table A.3.

INSTALLATION: the .zip file is decompressed to reveal the executable file ‘trace2d.exe’ or ‘trace3d.exe’ which can be moved to the desktop in Windows. The examples and input files can remain in any folder, but the Windows system folder ‘Program Files (x86)’ is not recommended.

RUN/EXAMPLE: clicking on the TRACE icon will produce a file-opening page. In our example, the input file is ‘fodotest.t2d’ (TRACE-2D). A blank page is produced after opening the file, but simply typing ‘g’ (for ‘graph’) will render the beam horizontal and vertical phase- space ellipses at the input (left pane) and output (right pane) planes, together with the beam line and the transverse beam envelopes at the bottom. Figure A.6 is an illustration of the output screen obtained after performing envelope matching in a FODO cell of UMER.

```
&DATA
ER= 0.511  Q= -1.  W= 0.010  XI= 7.000
EMITI =  16   16
BEAMI = -0.914037      1.8      0.914037      1.8
BEAMF =  0.00000       1.8      0.00000       1.8
BEAMCI=  0.00000       0.00000  0.00000       0.00000
FREQ=    425.000  PQEXT=  2.50  ICHROM= 0  IBS= 0  XC=   0.0000
XM=  10.0  XPM=    50.0000  YM=  10.00
XMI=   5.0 XPMI=   50.0000  XMF=   5.0 XPMF=  50.0000
N1= 1 N2= 5 SMAX= 0.5 PQSMAX= 2.0 nel1= 1 nel2= 5 NP1= 1 NP2= 5
MT= 1 NC= 4 MP=0,000 0,000 0,000 0,000
MVC=0,000,0 0,000,0 0,000,0 0,000,0

CMT(001)='DRIFT' NT(001)= 1  A(1,001)= 54.18
CMT(002)='Quad'  NT(002)= 3  A(1,002)= 0.57049E-01 51.64
CMT(003)='DRIFT' NT(003)= 1  A(1,003)= 108.36
CMT(004)='Quad'  NT(004)= 3  A(1,004)= -0.57049E-01 51.64
CMT(005)='DRIFT' NT(005)= 1  A(1,005)= 54.18

WS(1)= 0.00000 0.00000 0.00000 0.00000 0.00000 0.00000 0.00000
WS(8)= 0.00000 0.00000 0.00000 0.00000 0.00000 0.00000 0.00000
SIGI(1,1)= 45.216  -186.84  0.00000E+00 0.00000E+00 0.00000E+00
SIGI(1,2)=-186.84   851.67  0.00000E+00 0.00000E+00 0.00000E+00
SIGI(1,3)=0.000E+00 0.000E+00 34.734 57.21 0.0000E+00
SIGI(1,4)=0.000E+00 0.000E+00 157.21 815.21 0.0000E+00
SIGI(1,5)=0.000E+00 0.000E+00 0.000E+00 0.000E+00 131.21
COMENT='FODO match for 7.0 mA, 10keV'
&END
```

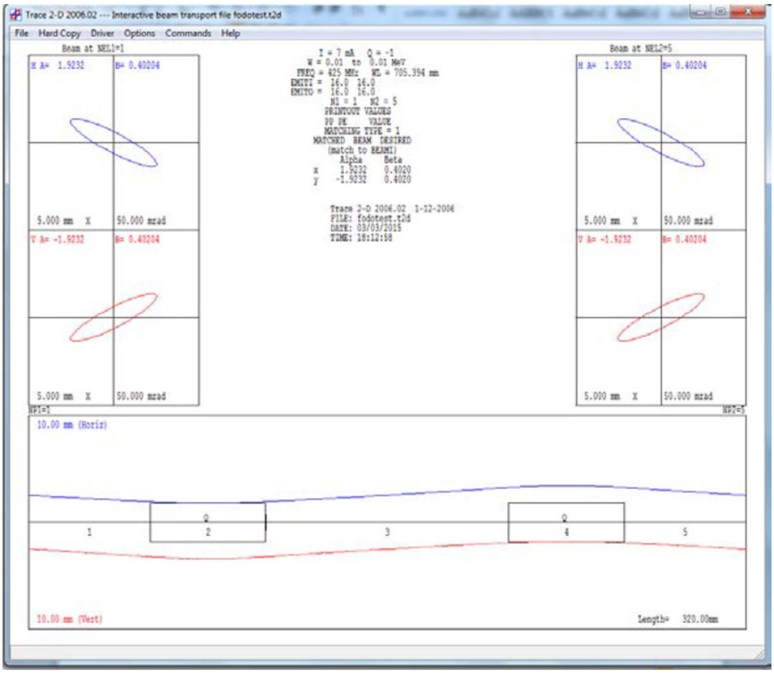

```
        I = 7 mA   Q = -1
      W = 0.01  to  0.01 MeV
    FREQ = 425 MHz   WL = 705.394 mm
   EMITI =  16.0  16.0
   EMITO =  16.0  16.0
           N1 = 1   N2 = 5
          PRINTOUT VALUES
          PP PE     VALUE
          MATCHING TYPE = 1
        MATCHED  BEAM  DESIRED
           (match to BEAMI)
              Alpha     Beta
        x     1.9232    0.4020
        y    -1.9232    0.4020

            Trace 2-D 2006.02  1-12-2006
            FILE: fodotest.t2d
            DATE: 03/03/2015
            TIME: 18:12:58
```

Figure A.6. TRACE 2D window after matching the beam envelopes in one cell of UMER for a 10 keV, 7 mA, 16 μm (x and y edge emittances) electron beam.

The second line of 'fodotest.t2d' defines the beam: 'ER' is rest mass in MeV, 'W' the kinetic energy in MeV, and 'XI' the beam current in mA (continuous beam). The next line contains the initial transverse edge emittances (EMIT) in mm-mrad. BEAMI (BEAMF) contains the initial (final) Courant–Snyder parameters α and β in the horizontal and vertical planes. XMI, XPMI, XMF, XPMF define the scales (in mm) for the initial and final phase-space ellipses. XM, YM define the scales for the envelopes. There are five elements in the beam line, 3 drift spaces and 2 quadrupoles; the drifts are in mm, and the quadrupole parameters are the gradient in T/m, and hard edge effective length (51.64 mm in our case).

The matching type is MT = 1, for ellipse parameters α_x, β_x, α_y, β_y. Envelope matching is carried out by typing 'm' and then 'g'. The phase advance and Courant–Snyder parameters are displayed by typing 'f'. A list of commands is provided in a dropdown menu. The input file can be modified and run again without saving or exiting the program. As an example, the current can be set to zero by typing 'I', and then 'xi = 0' in the new window; notice how the beam is mismatched. After re-matching, the new phase advances can be obtained; comparing these values with those obtained previously with full beam current illustrates the effect of linear transverse space charge (see chapter 4).

A.9 Winagile

Winagile is a free, Windows-based, computer code for beam transport calculations in transfer lines and rings. It is very good for doing things like tracking, envelopes, closed-orbit, closed-orbit corrections, resonances, etc. Both incoherent and coherent space-charge effects can be included as well, but the models are not very accurate. The code was written by P J Bryant from CERN, who is also the author, with Kjell Johnsen, of *The Principles of Circular Accelerators and Storage Rings* [11]. With some guidance, running the basic Winagile can be learned in a matter of minutes. The GUI is not the best in the world, plus more than a few bugs remain in the current version (ver. 3.5), but it is nonetheless a working code which can be easily applied to model many accelerators.

DOWNLOAD: You can download the code from Aarhus University (Denmark) website or from the Joint Universities Accelerator School website (see table 3). The file 'package(ver3.5_D054).zip' includes the windows-executable file, lattice examples (extension 'LAT') and help file 'winagile.hlp'.

INSTALLATION/RUN: the code will run under MS Windows XP, or under Wine in Ubuntu Linux. It is possible to run Winagile in Win 7-8 but only inside a virtual Win XP machine through VMware Player or Oracle's Virtual Box.

EXAMPLE: thinl1l2.lat – this lattice has two thin quadrupoles of opposite strengths and separated by a distance shorter than their individual focal lengths $f = 0.1$ m, in magnitude (see chapter 2). The total length of the beam line is 1.0 m.

1) Run Winagile and open the example file **thinl1l2.lat** (this you will find in the book's website). This lattice contains two types of elements: **DRIFT** and **THINQ.**
2) Note that you are in the **MAIN WINDOW.** Explore the different column values. Only the 'Length' and 'Thin quad kL' columns have values. In particular, the length of THINQ is zero, by definition. The integrated strengths (in m^{-1}) of the quadrupoles have opposite signs.
3) In the 'Calculations' menu choose 'Transfer Line'. A window 'Twiss Input' opens up; click OK. The input here is irrelevant to our present calculations. You end up with a new window called **BEAM PARAMETERS**.
4) In the 'Calculations' menu choose 'Tracking'. Enter 0.005 for 'Horizontal position, x' and also for 'Vertical position, z'. The window now changes to **TRACKING**.
5) In the 'Graphs' menu choose 'Trajectories'. A window with a blue background opens up showing the horizontal and vertical trajectories. The default particles are 1 GeV protons, but this is irrelevant, as all the information for the optics is contained in the 'kL' values (**MAIN WINDOW**). Click 'Save' and then 'Back' to return to the 'Tracking' window.
6) Repeat 4) with −0.005 values for x and z. Select the entire field to be able to change the signs from the original values (this is but the first example of a bug in the GUI!—but be patient).
7) Choose 'Trajectories' again in the 'Graphs' menu and then 'All'. You will see the wonders of 'alternating gradient' focusing: net focusing on both planes! You can now try increasing the separation of the quads to be more than their individual focal lengths. To do this you need to go back to the **MAIN WINDOW**, then 'File', 'Edit'. Double-click on the field that you want to change and press OK. Then go to 'Check Data' and select either option. You are ready to repeat the tracking calculations.

A.10 Mobile applications

Android: from the Google Play website—‘TAPAs stands for Toolkit for Accelerator Physics on Androids. It allows ‘back-of-the-envelope’ accelerator physics calculations, with more than 20 inter-linked types of calculations. These include storage ring scaling with energy and circumference, longitudinal dynamics in rings, free-electron lasers, electron linear accelerators, electron guns, bunch compression, iron-dominated multipole magnets, short pulse x-rays, undulator effects on orbit and optics, undulator radiation properties, undulator models, top-up parameters, electromagnetism, synchrotron radiation, particle passage through matter, and engineering calculations’. See also [18]. Figure A.7 shows a typical screen from TAPAS.

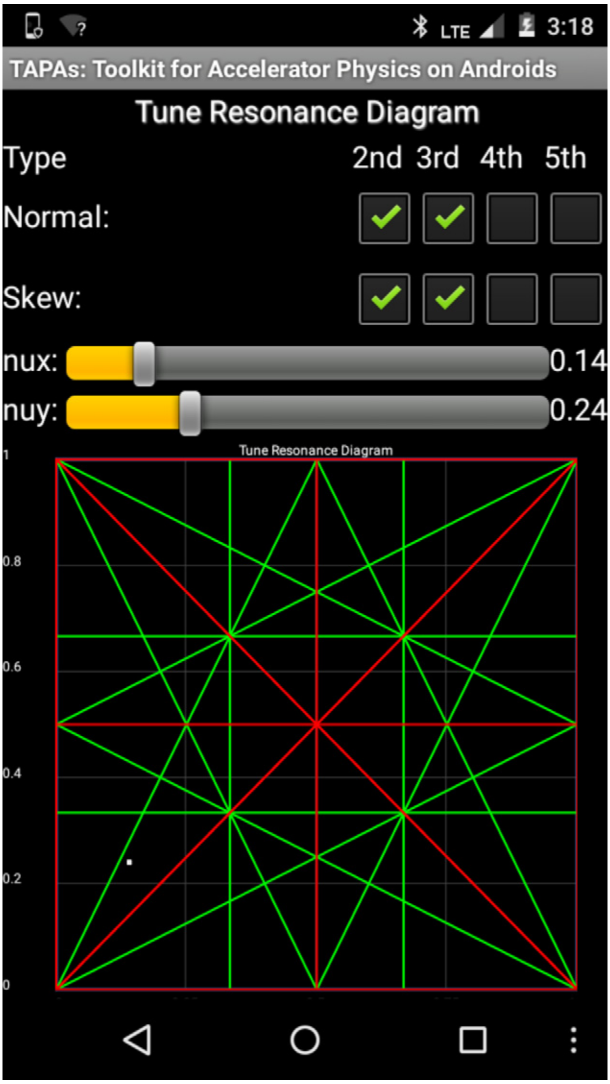

TAPAs: Toolkit for Accelerator Physics on Androids

Tune Resonance Diagram

Type	2nd	3rd	4th	5th
Normal:	☑	☑	☐	☐
Skew:	☑	☑	☐	☐

nux: 0.14

nuy: 0.24

Figure A.7. Screen from Android App TAPAS.

References

[1] Herbert Goldstein H 1980 *Classical Mechanics* 2nd edn (Reading, MA: Addison-Wesley)

[2] Donnelly D and Rogers E 2005 Symplectic integrators: an introduction *Am. J. Phys.* **73** 938

[3] Yoshida H 1999 *in Handbook of Accelerator Physics and Engineering* 3rd edn ed A Wu Chao and M Tigner (Singapore: World Scientific)

[4] Forest E 1998 *Beam Dynamics—A New Attitude and Framework* (Amsterdam: Hardwood Academic)

[5] Wolski A 2014 *Beam Dynamics in High Energy Particle Accelerators* (London: Imperial College Press)

[6] Douglas D *et al* 2007 Simplified charged particle beam transport modeling using commonly available commercial software *Proc. of PAC07 (Albuquerque, NM)* p 3651

[7] Borland M 2000 *Technical Report No. LS-287* (Lemont, IL: Argonne National Laboratory)

[8] Borland M 2015 User's Manual for elegant, Program Version 27.0.2, Advanced Photon Source

[9] Bernal S, Li H, Kishek R A, Quinn B, Walter M, Reiser M and O'Shea P G 2006 RMS envelope matching of electron beams from 'zero' current to extreme space charge in a fixed lattice of short magnets *Phys. Rev. ST Accel. Beams* **9** 064202

[10] Grote H, Schmidt F, Deniau L and Roy G (eds) 2015 The MAD-X Program (Methodical Accelerator Design), Version 5.02-04, User's Reference Manual (Geneva: European Laboratory for Particle Physics)

[11] Bryant P J and Johnsen K 1993 *The Principles of Circular Accelerators and Storage Rings* (Cambridge: Cambridge University Press)

[12] Carey D C, Brown K L and Rothacker F 1995 Third-Order TRANSPORT—A Computer Program For Designing Charged Particle Beam Transport Systems, SLAC-R-95-462, Fermilab-Pub-95/068, UC-414

[13] Murphy J 1993 Synchrotron Light Source Data Book, Version 3.0, October 1993, Brookhaven National Lab., BNL 42333 (revised) Informal Report.

[14] Allen C K, Guharay S K and Reiser M 1996 Optimal transport of low energy particle beams *Proc. of the 1995 Particle Accelerator Conference (Dallas, TX)* (New York: IEEE) p 2324

[15] Métral E 2013 Training-week in Accelerator Physics, Lund, Sweden, 27–31 May 2013

[16] PBO Lab (Particle Beam Optics Laboratory) User Manual, AccelSoft, Inc, G H Gillespie Associates, Inc., 1997

[17] Crandall K R and Rusthoi D P 1997 TRACE 3D Documentation *LA-UR-97-886, Los Alamos National Laboratory Report* 3rd edn

[18] Borland M 2013 Android application for accelerator physics and engineering calculations *Proc. of the 2013 Particle Accelerator Conference (Pasadena, CA)* p 1364